

Transmission Electron Microscope Characterisation of Iron-Rhodium Epilayers

Mathew Jonathon McLaren

Submitted in accordance with the requirements for the degree of
Doctor of Philosophy

The University of Leeds
Institute for Materials Research
School of Chemical and Process Engineering
Leeds, LS2 9JT
United Kingdom

September 2014

Declaration of Academic Integrity

The candidate confirms that the work submitted is his own, except where work which has formed part of jointly-authored publications has been included. The contribution of the candidate and the other authors to this work has been explicitly indicated below. The candidate confirms that appropriate credit has been given within the thesis where reference has been made to the work of others.

List of Publications

1. Characterisation of Magnetic FeRh Epilayers

M. J. McLaren, M. A. de Vries, R. M. D. Brydson and C. H. Marrows

[J. Phys. Conf, 371 1 012031 \(2012\)](#)

2. Aberration corrected STEM of iron rhodium nanoislands

M. J. McLaren, F. S. Hage, M. Loving, Q. M. Ramasse, L. H. Lewis, C. H. Marrows and R. M. D. Brydson

[J. Phys. Conf, 522 012039 \(2014\)](#)

3. Sputter Growth and Characterization of Metamagnetic B2-ordered FeRh Epilayers

C. Le Graët, M. A. de Vries, M. J. McLaren, R. M. D. Brydson, M. Loving, D. Heiman, L. H. Lewis, C. H. Marrows

[J. Vis. Exp. \(80\), e50603 \(2013\)](#)

4. Asymmetric "melting" and "freezing" kinetics of the magnetostructural phase transition in B2-ordered FeRh epilayers

M. A. de Vries, M. Loving, M. McLaren, R. M. D. Brydson, X. Liu, S. Langridge, L. H. Lewis, and C. H. Marrows

[Appl. Phys. Lett. 104, 232407 \(2014\);](#)

All work contained within publications 1 and 2 is directly attributable to M. J. McLaren under

the guidance of academic supervisors R. M. D. Brydson and C. H. Marrows. These publications relate to results presented and discussed in Chapters 5 and 6 of this thesis. Publications 3 and 4 are co-authorship papers. In Publication 3 M. J. McLaren is responsible for the TEM data collection. In Publication 4 M. J. McLaren participated in the synchrotron X-ray experiment at X22C, NSLS.

This copy has been supplied on the understanding that it is copyright material and that no quotation from the thesis may be published without proper acknowledgement.

2014 The University of Leeds and Mathew Jonathon McLaren.

Acknowledgements

Firstly, many thanks go to my supervisors Rik Brydson and Chris Marrows for giving me the chance to perform this research and somehow finding time in their schedules to provide help and insight, as well as providing opportunities to use top of the range microscopes, visit fantastic synchrotrons and attend some exotic (Kyoto) and less exotic (Manchester) international conferences.

Thank you to Mike Ward, John Harrington, Stuart Micklethwaite and Nicole Hondow who have managed to help me with much of the equipment I've used here at Leeds as well as berate me if I broke anything! Fred Hage and Quentin Ramasse at SuperSTEM as well as Damien McGrouther and Ian MacLaren at Glasgow have been tremendous people to work with, helping me to get some fantastic microscopy data. Everyone who has inhabited our well-hidden third floor office over the last four years deserves a mention, for providing entertainment and conversation for those (brief, of course!) moments between work.

Finally, two people who have always been there for me are my mum Kirsty, who always pushed me to question the world around me and Alice, who has managed put up with me for the entirety of my PhD, somehow keeping me sane along the way!

There is a theory which states that if ever anyone discovers exactly what the Universe is for and why it is here, it will instantly disappear and be replaced by something even more bizarre and inexplicable.

There is another theory, which states that this has already happened.

- Douglas Adams, *The Restaurant at the End of the Universe*

Abstract

Iron-rhodium (FeRh) alloys exhibit an unusual magnetostructural transition, making them a fascinating topic of research. When the alloy is approximately equiatomic ($\text{Fe}_{48}\text{Rh}_{52}$ to $\text{Fe}_{56}\text{Rh}_{44}$) it is in a caesium chloride (CsCl) structure. At room temperature it is antiferromagnetic (AFM), making a first-order phase transition to a ferromagnetic (FM) state when heated above ~ 350 K. There is also a 1% increase in unit lattice volume upon heating to the FM phase, as well as an increase in entropy and decrease in resistivity. The transition can be modified by doping, applied strain and applied magnetic field among other methods. Thin film FeRh has potential uses as part of a spin valve system for magnetic data storage and as a suitable choice for a memristor.

The work presented here demonstrates the methods approached to preparing a variety of sputter-deposited thin film FeRh samples for characterisation in a transmission electron microscope (TEM) as well as by techniques such as X-ray photoelectron spectroscopy (XPS) and X-ray diffraction (XRD). These include samples capped with epitaxial chromium (Cr) and tungsten (W) to raise and lower the transition temperature respectively. After cross-section or plan-view preparation using either a conventional ion polishing method or a focused ion beam, the samples were characterised using a variety of methods in the TEM. Initial characterisation has examined the crystal structure, layer thickness and interfacial roughness of these films, confirming results from bulk X-ray measurements. It has been found that FIB-prepared samples do not exhibit the phase transition whereas ion polished samples are unaffected. Compositional analysis of the interface FeRh makes with a magnesium oxide (MgO) substrate finds a change in iron-to-rhodium ratio while characterising the FeRh/cap interface finds significant Fe diffusion into Cr-capped samples with no interdiffusion seen in identical W-capped FeRh films. Analysis of the transition dynamics observing changes in strain and ferromagnetic domains via heating experiments have confirmed the nucleation and growth of the phase change at the interfaces. Finally, there is some evidence to suggest that a martensitic change is occurring in FeRh through the transition. The presence of twins in the FeRh as well as extra ordering spots in a FIB-prepared cross-section allude to a more complex transition than previously thought.

Contents

1	Introduction	1
2	Background	5
2.1	An Overview of Magnetism	5
2.1.1	Paramagnetism	6
2.1.2	Ferromagnetism	7
2.1.3	Antiferromagnetism	11
2.1.4	Ferrimagnetism	11
2.2	Magnetic Materials	12
2.3	Phase Transformations	15
2.3.1	Free Energy	15
2.3.2	First and Second Order Transformations	17
2.3.3	Diffusionless Transformations	18
2.3.4	Magnetic Phase Transformations	19
2.4	The Iron-Rhodium System	21
2.4.1	Controlling the Transition	25
2.4.2	Dynamics of the Transition	30
2.4.3	Inducing Ferromagnetism via Laser Heating	33
2.4.4	Latent FM in AFM phase	35
2.4.5	Theories to Explain the Transition	35
2.4.6	Uses of Iron-Rhodium	37
3	Instrumentation and Theory	39
3.1	Introduction	39
3.2	Thin Film Growth	39

3.2.1	Molecular Beam Epitaxy	40
3.2.2	Direct Current (DC) Magnetron Sputtering	40
3.2.3	Other Methods	42
3.2.4	Comparison of Growth Methods	43
3.3	X-ray Diffraction	43
3.4	X-ray Reflectivity	45
3.5	Neutron Diffraction	46
3.6	Sample Preparation for TEM	47
3.6.1	Ion Polishing Method	48
3.6.2	Focused Ion Beam	50
3.6.3	Comparison of Sample Preparation Techniques	53
3.7	Transmission Electron Microscopy	57
3.7.1	Electron Sources	58
3.7.2	The Condenser Lens, Aberration and its Correction	60
3.7.3	Beam-Sample Interactions	62
3.7.4	Electron Diffraction	62
3.7.5	Bright Field and Dark Field Imaging	64
3.7.6	High Resolution TEM	64
3.7.7	Scanning TEM and High Angle Annular Dark Field	65
3.7.8	Energy Dispersive X-Ray Spectroscopy	68
3.7.9	STEM-EDX Drift	68
3.7.10	Electron Energy Loss Spectroscopy	71
3.7.11	Lorentz Imaging	72
3.7.12	Electron Microscopes and Analysis	73
3.8	X-ray Photoelectron Spectroscopy	74

4	FeRh Structure and Observations of Strain and Dislocation at the Interfaces	77
4.1	Introduction	77
4.2	Film Overview, Sample Thickness and Interfacial Roughness	77
4.3	X-ray Diffraction	79
4.4	Electron Diffraction Pattern Analysis	82
4.5	Direct Structure Observations	84
4.6	Interfacial Strain	85
4.7	FeRh Twins	87
4.8	Chapter Summary	94
5	Local Chemistry of FeRh at the Film/Substrate Interface	96
5.1	Introduction	96
5.2	STEM-EDX Maps and Line Profiles	96
5.3	STEM-EELS Spectrum Images and Line Profiles	97
5.4	EELS Edge Analysis	104
5.5	Rhodium EELS Delocalisation	105
5.6	Chapter Summary	108
6	Local Chemistry of FeRh at the Film/Cap Interface	109
6.1	Introduction	109
6.2	Initial XPS	110
6.3	STEM-EDX Maps and Line Profiles	112
6.4	STEM-EELS Spectrum Images and Line Profiles	118
6.5	EELS Edge Analysis	127
6.6	Chapter Summary	130

7 Changes in Strain and Magnetism by Heating Through the FeRh Transition 131

- 7.1 Introduction 131
- 7.2 Strain Field Heating Experiments 131
- 7.3 Diffraction Pattern Changes Across Transition 138
- 7.4 Plan View Magnetic Imaging 139
- 7.5 Cross-Sectional Magnetic Imaging 143
- 7.6 Chapter Summary 145

8 Conclusions and Future Work 148

List of Figures

1	Diagram demonstrating the random nature of paramagnetism due to the thermal energies of the system. There is no overall order in a paramagnetic material (and therefore no magnetic moment) until thermal energies are overcome, by either a very low temperature or a very strong applied field.	7
2	Diagram of ferromagnetic order in the absence of an applied magnetic field. The material is broken into domains, each with their own orientation. The random alignment of each domain cancels the overall magnetic moment of the material. This is analogous to paramagnetic systems albeit on a larger scale.	8
3	Example of a typical hysteresis loop for a magnetic sample. The sample is still magnetised with no applied field after the material is magnetised to saturation. . . .	10
4	Diagram of the ordering of antiferromagnetic systems. The vectors of the parallel and antiparallel magnetic moments are equal in magnitude, resulting in no measurable magnetic field from the material.	12
5	Simple example of giant magnetoresistance. The two ferromagnetic materials can either have parallel or antiparallel magnetisation. If the magnetisations are parallel then the resistance for an electron travelling through the system perpendicular to the magnetisation is low. If the magnetisations are antiparallel, the resistance is high. . .	13
6	Diagram demonstrating the stability of a system moving from state A to state B. The minimum at A represents a metastable state while the minimum at B represents the most stable state with the lowest free energy.	16
7	Graphs demonstrating the change in Gibbs free energy, volume and entropy through a first order phase transition. Discontinuities are visible at the transition temperature T_t in the first orders, in this case volume and entropy.	17

8	Graphs demonstrating the change in entropy and specific heat capacity through a second order phase transition. Entropy does not exhibit a discontinuity whereas specific heat capacity (the second derivative of Gibbs free energy) sees a jump across the transition.	18
9	Example of coexistence between parent and product phases, resulting in a lath-like structure.	19
10	Graphs showing different examples of first and second order transitions in magnetic materials. (a) Change in magnetisation for a single crystal $\text{Ni}_{14}\text{Co}_5\text{Mn}_3\text{Sb}_2$ Heusler alloy. (b) Example of a typical demagnetisation curve of a ferromagnet as it approaches its Curie temperature.	20
11	Demonstration of the CsCl-type structure of iron-rhodium. The lattice parameter ($a = b = c$) at room temperature is 2.987 Å. The lattice parameter changes to 2.997 Å above the transition temperature.	21
12	X-ray diffraction peak for (004) FeRh, showing the peak shift corresponding to the 1% unit lattice expansion when heating to the FM phase.	23
13	Example of a typical resistivity measurement for FeRh through the transition. The resistivity in the heating curve (red) slowly increases in a linear fashion as is expected for a heated metal. However, there is a characteristic drop as the material makes a transition to the FM phase, after which it begins slowly increasing again. Upon cooling (blue) it can be seen that the resistivity is hysteretic. The inset shows the derivative of resistivity w.r.t. temperature, highlighting the difference in transition temperature depending on direction.	23
14	Phase diagram of the iron-rhodium system as determined by Swartzendruber. The area of interest is the α'' section, where the sample is antiferromagnetic. Heating of the sample will cause a phase change into the ferromagnetic α' region.	24

15	Magnetisation against temperature for FeRh films annealed at various temperatures. Higher annealing temperatures result in a sharper phase transition.	29
16	Change in magnetisation against temperature for FeRh nanoparticles. It can be seen that there is a large broadening of the phase transition from the FM-AFM phase while the AFM-FM transition remains largely unaffected.	30
17	X-ray photoemission electron microscopy (XPEEM) images showing the nucleation of ferromagnetic domains and phase coexistence during the phase transition.	32
18	Comparison of the change in the (004) FeRh reflection upon heating and cooling. The black line on each represents the middle of the phase transition, and it may be seen that the cooling curve shows greater separation of the two peaks.	33
19	Example of the change in magnetisation when heated by a picosecond laser. The open circles show the magnetisation increase while the filled ones are an example of the lattice parameter change. ΔR shows the change in reflectivity (measuring lattice expansion) while $\Delta\theta$ shows the change in magnetic polarisation. The inset shows the full changes in magnetisation and lattice parameter over 400 ps.	34
20	Structural and magnetic scattering length-density (SLD) depth profiles for FeRh above and below the transition temperature obtained from the CRISP reflectometer at ISIS. The increase in the magnetic SLD at 300 K shows the presence of ferromagnetic domains close to both interfaces. The change in the structural SLD suggests a Fe-deficient (Rh-rich) area towards the cap which could explain the FM region.	36
21	Schematic of a molecular beam epitaxy process.	41
22	Schematic of a sputtering process.	42
23	Visualisation of diffraction in a crystal lattice.	44

24	Example of a typical X-ray diffractogram for an FeRh film. The existence of a (001) peak shows that FeRh is in a B2-ordered structure. By collecting integrated intensities of the (001) and (002) peaks an experimental value for chemical order parameter, S, may be determined.	46
25	Example of a typical X-ray reflectivity curve with a fit applied.	47
26	Schematic showing the various stages of cross-sectional TEM sample prep, by a conventional, mostly mechanical method. (a) The sample is cut into wafers and stacked together with silicon wafers cured together with epoxy. (b) A cylinder is cut out of the stack and encapsulated in a brass tube with epoxy. (c) Cross sections are cut from the tube and polished to $\sim 100 \mu\text{m}$. (d) The sample is dimpled until there is a $\sim 10 \mu\text{m}$ thick region in the centre of the sample. (e) The sample is ion polished on both sides until there is a small hole in the middle of the sample. At this point, the region around the edge of the hole is $\sim 20\text{-}50 \text{ nm}$ thick and thin enough for HRTEM imaging.	51
27	Example of a FIB section cut out of a thin film (a) pre-thinning and (b) after partial thinning. The area around and under the sample has been excavated in image a. (c) The finished FIB lamella. (d) Rough measurements of lamella thickness.	52
28	Comparison of MgO redeposition in a FIB prepared and conventionally prepared cross-section. There is a very small amount of Mg signal scattered throughout the image. The conventionally prepared sample shows no Mg signal across the film although there is a large area of redeposition found in the epoxy layer. While uncommon, this is still a potential issue when preparing cross-sections.	54

29	Comparison of electron-transparent regions in a FIB prepared and conventionally prepared cross-section. The entire FIB section is electron transparent while only particular areas of the cross-section provides enough contrast range in conventionally prepared samples.	55
30	Comparison of amorphisation in FIB and conventionally prepared samples. The amorphous layers are visible at the bottom and left of the FIB and conventional samples respectively.	56
31	Schematic of a transmission electron microscope and its major components.	58
32	Ray diagrams demonstrating (a) an ideal lens with no aberration (b) a lens with spherical aberration.	61
33	Example of an electron diffraction pattern. Pictured is [001] fcc MgO crystal.	63
34	Comparison of a bright field and a dark field TEM image of the (002) MgO spot. The MgO is expected to be single crystal but changes in the Bragg condition (e.g. from strain at the interface) is visible in the bright field as dark contrast and in the dark field image as bright contrast.	65
35	HRTEM image of an MgO single crystal substrate along the [020] zone axis. Here the lattice fringes are visible, allowing direct viewing of the crystal lattice.	66
36	Schematic of scanning transmission electron microscope operating principles.	67
37	Schematic of demonstrating some available transitions that give rise to X-ray emissions.	69
38	HAADF STEM and STEM-EDX maps demonstrating the effect of drift on results obtained. The position of the initial HAADF-STEM image is very dislocated from the resulting STEM-EDX map with a smearing of the signal in the vertical direction (the signal of the layer is strong in the middle and weak at the edges).	70
39	Diagram demonstrating EELS edge with their associated electron excitations.	72

40	Diagram demonstrating EELS edge with their associated electron excitations. The Rh edge is highlighted as it is very weak relative to the background and is very close to the carbon K edge and therefore easily missed.	73
41	(a) Schematic of how the beam is affected in Fresnel imaging. The beam is deflected when passing through the ferromagnetic domains and bringing the image out of focus shows areas of contrast where domain walls exist. (b) Typical example of a Fresnel image acquired in Lorentz mode. The black and white lines signify the location of domain walls in the film.	74
42	(a) Schematic of a segmented DPC detector and how beam deflection affects the image. (b) Typical example of a vector map showing magnetic domains acquired via DPC.	75
43	A simulated fit for an X-ray reflectivity curve for an FeRh film with a W cap.	80
44	A TEM bright field image showing an example of a typical FeRh film grown on MgO. The large contrast between MgO and FeRh is clearly visible, and the interface between the two appears to be smooth. Epitaxy may be seen across the film-substrate interface as well as the film-cap (W) interface. In comparison, the interface of the cap appears rougher. Contrast is visible along both interfaces likely due to strain. Also, Moiré fringes are visible within the FeRh.	80
45	X-ray diffraction pattern of two FeRh films, a Cr-capped sample (a) and a W-capped sample (b). The principle peaks of MgO, FeRh, Cr and W are labelled.	81
46	X-ray diffraction pattern of Cr and W-capped FeRh samples with emphasis on the (002) FeRh peaks as well as the (002) Cr and W peaks. The FeRh peak is seen to shift depending on the capping layer applied.	81

47	(a) Example of a typical selected area electron diffraction pattern of FeRh grown on an MgO substrate prepared by ion polishing. (b) Measurements and analysis of FeRh/MgO SAED pattern. The black spots correspond with the MgO lattice and the red spots FeRh. The epitaxial relationship (FeRh[100](001) MgO[110](001)) may be seen due to the overlap of the (020) MgO and (110) FeRh spots.	82
48	Typical HAADF-STEM image of an FeRh film taken along the [110] FeRh zone axis. The discrete Fe and Rh layers are clearly visible due to the difference in contrast caused by the atomic number difference. This is expected for the CsCl crystal phase that has grown. Direction of epitaxial growth is marked with an arrow.	84
49	MAADF and HAADF images of an FeRh/MgO interface taken along the [110] zone axis of a FIB-prepared FeRh film. There is a ~0.5 nm layer of contrast within the FeRh that suggests interfacial strain.	85
50	MAADF and HAADF images of an FeRh/Cr interface taken along the [100] zone axis of a FIB-prepared FeRh film. In both images there is dark contrast within the Cr layer which may be attributed to the strain bringing the areas off-axis and disrupting the channelling conditions. There is considerable contrast within the Cr layer as well as a band of contrast ~3 nm thick at the bottom of the image, extending somewhat into the FeRh.	86
51	MAADF and HAADF images of an FeRh/W interface taken along the [110] zone axis of a FIB-prepared FeRh film. There is a 3-5 nm layer of contrast within the FeRh as well as contrast in the W layer. The larger lattice mismatch (5.5%) relative to MgO and Cr fits with the larger contrast band seen here.	86
52	Bright field TEM image showing the diagonal bands of contrast in an FeRh film prepared by FIB. These lines seem to begin at the interfaces and travel through much of the FeRh film, but are not visible elsewhere within the film.	87

53	HRTEM image showing the twins in the FeRh thin film in greater detail on a W-capped FeRh film prepared by FIB. Other than the direction and angle, there is no pattern or periodicity in the contrast. Moiré fringes are also visible within the FeRh which is potentially an overlap of twins within the crystal.	88
54	HRTEM image of a conventionally prepared FeRh sample along the [110] axis exhibiting the same lath contrast seen in FIB-prepared cross-sections (circled with direction highlighted). The effect is less widespread and not as obvious but clearly still exists. There is a strong presence of Moiré fringes close to the interface	91
55	Microdiffraction pattern summed from only the FeRh layer in a FIB-prepared Cr-capped sample. When compared to a standard selected area diffraction pattern of an FeRh film, there are many extra diffraction spots visible. The locations of some standard CsCl FeRh spots are highlighted. It is important to note that, while at room temperature, the heating experiments performed on FIB-prepared cross-sections suggest that this is not in the AFM phase.	92
56	Observations of twins in HAADF-STEM. To the left and right of the red lines (i.e. twin boundaries) exists one crystal orientation whereas in between exists another. (a) The main crystal orientation appears to be [111] showing (111) planes. At the twin boundary (which lies along the (111) plane), the planes make an angle of $\sim 65^\circ$ with the twin plane. (b) The main crystal orientation is [001] and shows (100) planes. At the twin boundary the planes make an angle of 45° with the twin plane. As the twin plane is (111) it is not edge on and the crystal goes out of orientation on the other side of the twin boundary.	93

57	STEM-EDX maps of Mg, O, Fe and Rh with a composite of Fe, Rh and O and a HAADF-STEM image. The positions of the layers correlate well with the HAADF and no obvious interdiffusion around the FeRh/MgO interface is visible. Some O signal is detected outside the substrate however this is most likely due to oxidation of the surface of the sample. No variation or texturing may be seen within the FeRh film both close to and far away from the interface. In the mapped area, more signal is collected on the right hand side of the sample but this is likely due to a thickness gradient in this particular area of the sample.	98
58	STEM-EDX maps of Mg, O, Fe and Rh with a composite of Fe, Rh and O and a HAADF-STEM image with emphasis on the FeRh-MgO interface. As with figure 57, the interface appears sharp with no obvious traces of interdiffusion. The Fe and Rh signal is consistent throughout the film showing no positional dependence from the interface for the Fe:Rh ratio.	99
59	Line profiles showing change of intensity of Mg, O, Fe and Rh across the FeRh/MgO interface. The data is noisy but it can be seen that Fe and Rh have not diffused across the interface. A small amount of Mg signal is detected within the FeRh layer which is unlikely to be interdiffusion due to the sputtering process as this would fall off quickly further into the sample. Instead this is more likely to be a result of the FIB preparation process. While there is Mg signal in the FeRh and vice versa close to the interface, this is due to both beam broadening and the large probe formed in the microscope used. From this interface an approximation of probe size may be determined from the FWHM, showing a probe size of $\sim 2.5 \text{ \AA}$	100

60	HAADF image demonstrating the spatial resolution obtained using aberration-corrected HAADF-STEM of [110] FeRh. The Fe and Rh columns of atoms can be clearly differentiated with Rh, the heavier atom, scattering more strongly and therefore appearing brighter. The structure appears as expected for a CsCl crystal with alternating rows of Fe and Rh.	101
61	(a) HAADF image taken at the interface of FeRh and MgO along the [100] FeRh zone axis. The MgO appears dark as it is a lighter element that does not produce much inelastic scattering and the electron beam mills the material away as the beam scans over it. However, it may be seen that there are no obvious intensity changes and the Fe and Rh atoms appear to alternate as expected. (b) Line profile taken from the HAADF image showing change in intensities of the atomic columns. Peaks and troughs correspond with Rh and Fe respectively. It can be seen that there is intensity change through the sample although this corresponds with the contrast caused by twinning. There is variation in intensity but not enough to demonstrate a significant change in Fe or Rh composition.	102
62	STEM-EELS spectrum images acquired at the FeRh-MgO interface along the [100] zone axis, with maps for iron L _{2,3} , rhodium M _{4,5} and oxygen K edges. A HAADF image of the same region is provided for comparison, with a dotted line indicating the FeRh-MgO interface. There is a variation in intensity for the first two Fe rows, which appear brighter than the other Fe layers. Distortion in the HAADF image appears due to beam-sample interactions, particularly due to the magnetic nature of the sample.	103

63	Line profiles taken from the above EELS spectrum images, showing the relative change of Fe, Rh and O across the FeRh-MgO interface. The first two rows of Fe atoms have a noticeably stronger signal relative to the rest of the atoms and the first Rh layer (in between the two Fe rows) is diminished in comparison to the remaining layers. The HAADF profile for the same area is offset above. The intensity change at the interface cannot be seen on the HAADF. Probe size is expected to have a diameter of $\sim 1 \text{ \AA}$	105
64	Background-subtracted EELS spectra showing change in the O-K edge across the FeRh-MgO interface, beginning with FeRh at the top and MgO at the bottom. As the probe location passes close to the film, a pre-peak begins to appear before promptly disappearing along with the rest of the edge within the FeRh. This pre-peak is indicative of a transition metal oxide bond and, combined with the EELS spectrum images showing a terminating Fe layer, confirms the formation of an iron oxide at the interface.	106
65	Background-subtracted EELS spectra showing change in the Fe-L _{2,3} edges across the FeRh-MgO interface, beginning within the FeRh at the top and ending within the MgO at the bottom. A small shoulder is visible at the FeRh/MgO interface to the right hand side of the L ₃ edge, which is indicative of an Fe ²⁺ oxide bond. This promptly disappears in both directions away from the interface.	107
66	Background-subtracted Fe 2p and Rh 3d peaks from the surface of the sample to 12 nm into the thin film. The depth values were obtained by averaging the etching times for pure Fe and Rh.	111

67	Depth profile created from the background-subtracted Fe 2p, Rh 3d and Al 2p peaks. Deep within the FeRh it may be seen as equiatomic but closer to the interface there are deficiencies of Rh and Fe. The interaction volume of electrons emitted means that signal nominally collected from the surface will also collect signal from a few nm within the sample. As a result, it is likely that there is a small Fe deficiency located at the FeRh-Al interface and then an Fe-rich region beyond that point. There is also a significant diffusion of Al into the top of the FeRh layer.	111
68	STEM-EDX maps taken from an FeRh film with a Cr cap prepared using ion polishing. No evidence of large compositional variation exists within the FeRh. The Cr layer is very well defined, although it appears highly oxidised along with the Al layer. The FeRh again appears to have suffered from surface oxidation. Al is detected throughout the FeRh, which is likely due to redeposition of alumina suspension used during the sample preparation process.	114
69	Bright field TEM image of the area shown in the STEM-EDX maps of figure 68. A large amorphous region is visible on the far right of the sample that corresponds with the Al and O signal found in the maps. This is likely to be residue of the alumina suspension used in the dimpling phase of the sample preparation process.	114
70	EDX line profile created from the maps in figure 68. There is little evidence of interdiffusion of Cr into the FeRh although the left side of the Al has a shoulder leading into the Cr, suggesting a small amount of diffusion. Both the Al and Cr layers are highly oxidised with some relatively strong signal (i.e. not an effect of surface oxidation) found within the first few nm of the FeRh. There is an increase in Fe concentration relative to Rh directly at the interface but no inferences may be made from this due to the large signal variation throughout the FeRh layer.	115

71	STEM-EDX maps taken from an FeRh film with a W cap prepared via FIB. No evidence of large compositional variation exists within the FeRh. The Cr layer is very well defined, although it appears highly oxidised along with the Al layer. The FeRh again appears to have suffered from surface oxidation. Al is detected throughout the FeRh, which is likely due to redeposition of alumina suspension used during the sample preparation process.	116
72	EDX line profile created from the maps shown in figure 71. there is little evidence of interdiffusion between FeRh and W seen here. The W and Al layers are partially oxidised with a small amount of interdiffusion between these two layers.	117
73	HAADF-STEM image of the FeRh/Cr interface along the [100] FeRh (and Cr) zone axis. While not as well-defined as the FeRh/MgO interface seen in other HAADF-STEM images (e.g. figure 61) the epitaxy between the layers is barely visible as well as the single crystal nature of the chromium. The terminating layer is ambiguous due to the large amounts of strain affecting the contrast combined with the roughness of the interface, however the Fe and Rh are labelled. Growth direction of both FeRh and Cr is shown with an arrow.	119
74	STEM-EELS spectral images showing elemental maps of Fe, Rh, O and Cr with a HAADF image for comparison. The colours indicate a temperature scale ("hotter" colours show higher signal). There is no evidence of Rh or Cr diffusion around the FeRh/Cr interface however it can be seen that a large amount of Fe is visible within the nominally Cr layer. There is also little oxygen signal found within the Cr layer while it is found elsewhere within the FeRh.	120

75	Line profile plot created from the elemental maps in figure 74. By including the FeRh/MgO interface to observe relative drop in Fe and Rh concentration at the cap interface, it can be seen that iron is detected throughout the chromium cap, with the signal eventually disappearing when the chromium layer ends. Also, it appears as though the ratio of Fe:Rh varies slightly through the film. There is an Fe-deficient area close to the FeRh-Cr interface which, if Fe is detected within the Cr cap, makes sense as the Fe would have diffused from the neighbouring region.	121
76	Quantified EELS line profile for Fe and Cr only. Within the Cr layer there is a stable Fe concentration of $\sim 10\%$	122
77	Phase diagrams for Cr-Fe and Cr-Rh alloys. CrFe alloys remain in a bcc phase regardless of ratio. Adding Rh to Cr creates a multiphase CrRh which remains bcc until 22% atomic Rh, where a Cr_3Rh alloy is formed.	123
78	HAADF-STEM image of the FeRh/W interface along the [110] FeRh (and W) zone axis. In a similar manner to the Cr layer previously described in figure 73 the layer is seen as less strongly defined than the FeRh/MgO interface (figure 61) due to the roughness of the FeRh layer and how this roughness is displayed in a 2D projection. Visibility of a terminating layer is difficult due to the high strain affecting the contrast and the distortion of the lattice. However, the W lattice is seen here to be a single crystal. Growth direction of the FeRh and W crystal is indicated by an arrow. . . .	124

79	STEM-EELS spectral images showing elemental maps of Fe, Rh, O and W as well as a HAADF image of the area. The colours indicate a temperature scale ("hotter" colours show higher signal). Unlike the Cr-capped sample, the interface is very well defined and shows no evidence of diffusion between the layers. There is also a small degree of oxidation within the W layer. In the image a large variation in Fe content can be seen, when comparing to other samples this appears to be an anomaly with no similar compositional variations seen elsewhere.	125
80	Line profile created from figure 79. The lack of interdiffusion across the FeRh-W interface is obvious with no significant composition changes occurring. There is a large amount of noise in the W curve within the FeRh due to a high signal:noise ratio using an edge with such a high energy loss. Finally, the oxidation of the W is seen with a small 1-2 nm region of FeRh also suffering from a small amount of oxidation.	126
81	Phase diagrams for W-Fe and W-Rh alloys. In both cases W allows a small percentage of alloying (3% for Rh and 2% for Fe) after which a multiphase alloy exists for both.	127
82	Background-subtracted EELS spectra of the Cr $L_{2,3}$ edges at the FeRh/Cr interface. There are no obvious changes across the interface other than an increase in intensity.	128
83	Background-subtracted EELS spectra of the Fe $L_{2,3}$ edges at the FeRh/Cr interface. There are no obvious changes across the interface other than an increase in intensity.	128
84	Background-subtracted EELS spectra of the W $M_{4,5}$ edge at the FeRh/Cr interface. The W edge is extremely broad and is noisy here due to the high energy loss. The edge intensity drops quickly at and beyond the interface into the FeRh.	129

85	Background-subtracted EELS spectra of the Fe $L_{2,3}$ edges at the FeRh/W interface. The intensity of the FeRh edge decreases further into the W layer but there are no changes that cannot be attributed to noise. The bottom curve shows two small, broad peaks both before the Fe edge that are likely attributable to extended energy loss fine structure (EXELFS) oscillations from the $Cr_{2,3}$ edge.	129
86	Bright field heating experiments of FeRh with a Cr cap prepared using ion polishing at (a) room temperature (b) 85 °C (c) 97 °C (d) 166 °C. (a) At room temperature, some pockets of contrast are visible. (b) As the temperature is increased these regions become larger until (c) the regions can be seen to coalesce. (d) Finally, within the expected FM phase most of the sample now appears dark. This suggests strain nucleates at the interfaces and propagates through the sample.	133
87	HRTEM image of a grain boundary located within an FeRh film along the [110] zone axis. The line of dark contrast indicates the boundary. The FeRh on the right of the boundary is observed along the zone axis while the FeRh on the left is slightly off-axis.	135
88	Bright field heating experiments of FeRh with a Cr cap prepared conventionally observing a grain boundary in the FeRh structure at (a) 30 °C (b) 130 °C (c) 150 °C (d) 190 °C. (a) At low temperatures, there is a large area of contrast close to the grain boundary. (b) As the temperature is increased area of contrast appear although are constrained to opposite corners adjacent to the substrate and cap interface. (c) Heating further the areas of contrast increase in size and contrast begins to form at the interfaces. (d) At high temperatures far into the expected FM phase much of the film appears dark.	136

89	Bright field heating experiments of FeRh with an Al cap prepared using a focused ion beam at (a) room temperature (b) 100 °C (c)130 °C (d) 190 °C. Unlike previous experiments on different samples, there is no obvious change in contrast when heating through the transition and instead there is dark contrast even at room temperature.	137
90	Microdiffraction pattern summed from only the FeRh layer in a FIB-prepared Cr-capped sample. When compared to a standard selected area diffraction pattern of an FeRh film, there are many extra diffraction spots visible. The locations of some standard CsCl FeRh spots are highlighted. It is important to note that, while at room temperature, the heating experiments performed on FIB-prepared cross-sections suggest that this is not in the AFM phase.	139
91	Selected area diffraction patterns of a plan-view FeRh film with a W cap below the transition temperature at 25 °C (AFM phase) and above the transition temperature at 200 °C (FM phase). There is no obvious visible change between the two aside from a slight rotation that is probably due to sample drift rather than any change in crystal structure.	140
92	Various TEM images of a) a Fresnel image showing the existence of magnetic domains. The lines of bright and dark contrast corresponds with ferromagnetic domain walls. b) a DPC image again showing magnetic domains, instead imaging them directly with colour showing the direction of magnetisation. c) a Fresnel image with the sample brought to saturation magnetisation. Magnetic contrast from the domain walls is no longer visible but there is still a lot of contrast that appears in both this image and in 92a, potentially due to defects or granularity of the crystal. d) a diffraction pattern of the same area. The lack of evidence of polycrystalline or amorphous signal here suggests that the contrast is due to grains in the Cr capping layer.	141

93	A series of Fresnel images observing the change in domain wall signal during cooling at (a) 199 °C (b) 120 °C (c) 108 °C (d) 27 °C. At 199 °C the sample is in the FM phase and domain walls are visible throughout the sample. In the middle of the phase transition at 120 °C more contrast is visible, suggesting a higher density of domains. Cooling further to 108 °C the domain walls are still visible but have a lower intensity. Finally at 27 °C the sample is in the AFM phase and no domain wall contrast is visible.	142
94	A series of DPC images observing the change in magnetic signal as the sample cools at (a) 200 °C (b) 171 °C (c) 130 °C (d) 70 °C. (a) Within the FM phase, the FM domains are clearly visible with many large, single-coloured areas. (b) As the sample is cooled, the domains are less well-defined and appear speckled in nature. (c) Within a reference in a or b, the location of the domains is much harder to ascertain. The original domains still exist but the speckle pattern is much more prominent. (d) In the AFM phase there are no longer any clearly defined ferromagnetic domains as expected.	144
95	DPC images taken in the nominal FM (200 °C) and AFM (30 °C) phases for a FIB-prepared FeRh cross-section. It can be seen even deep within the AFM phase (~90 °C below the transition temperature) the domains still exist unchanged from the image taken above the transition.	145

List of Tables

- 1 Table of typical thickness and roughness values for various materials and the interfaces they make compared to values determined by X-ray reflectivity. Thickness values are for the bolded material in the interface column. Roughness and thickness values are obtained from the sample shown in figure 44 and the XRR data in figure 43 with the exception of the Cr and Al interfacial data. 79

- 2 Table of lattice parameter values as determined from selected area diffraction patterns compared to both measured XRD values and literature values (also derived using XRD)¹⁻³. The values for SAED are calibrated to the lattice parameter of MgO at 4.212 Å. 83

Abbreviations Used

Symbol Full Term

2D Two-dimensional

ADF Annular dark field

AFM Antiferromagnet

bcc Body-centred cubic

bct Body-centred tetragonal

BF Bright field

CsCl Caesium Chloride

DF Dark field

DPC Differential phase contrast

EDX Electron-dispersive X-ray spectroscopy

EELS Electron energy loss spectroscopy

EFTEM Energy filtered transmission electron microscopy

fcc Face-centred cubic

FEG Field emission gun

FeRh Iron-Rhodium

FIB Focused ion beam

FM Ferromagnet

GMR Giant magnetoresistance

HAADF High angle annular dark field

MAADF Medium angle annular dark field

MBE Molecular beam epitaxy

PEEM Photoemission electron microscopy

PIPS Precision ion polishing system

PNR Polarised neutron reflectometry

SAED Selected area electron diffraction

SEM Scanning electron microscope

SIMS Secondary ion mass spectrometry

SQUID Superconducting quantum interference device

STEM Scanning transmission electron microscope

TEM Transmission electron microscope

XMCD X-ray magnetic circular dichroism

XPEEM X-ray photoemission electron microscopy

XRD X-ray diffraction

XRR X-ray reflectivity

XPS X-ray photoelectron spectroscopy

1 Introduction

Magnetic materials play a key role in every day life, from electric motors and generators to magnetic resonance imaging (MRI) devices and computer hard drives. Recently magnetostructural materials have become an interesting topic for research. A magnetostructural material is a material that makes an abrupt and hysteretic phase transformation that exhibits both a magnetic and structural change. Some magnetic shape memory alloys - materials that make a reversible structural change under the influence of an applied magnetic field - in particular NiMnGa Heusler alloys, exhibit this magnetostructural phase transition^{4,5}. Other magnetostructural materials have been used in sensor devices that are capable of observing local changes in magnetic field, strain or temperature⁶. Some of these materials also exhibit a magnetocaloric change - variations in temperature when exposed to a changing magnetic field - that has applications in magnetic refrigeration⁷.

Iron-rhodium (FeRh) alloys are another such material that exhibit a magnetostructural phase transition. These alloys are potentially a very useful material due to their unusual phase transition. In a near equiatomic state, FeRh exists in a CsCl structure and undergoes a magnetostructural phase transition upon heating from an antiferromagnetic (AFM) phase to a ferromagnetic (FM) phase at around 350 K⁸, with a 1% increase in the unit lattice volume⁹. While similar transitions exist in other materials such as Ru-doped CeFe₂ alloys¹⁰⁻¹² and Co/Pd multilayers¹³, the FeRh transition occurs at a higher temperature relative to CeFe₂ and also has the ability to tune the transition temperature through a variety of methods, including applying an external field, varying the composition, doping with various materials and applying strain^{3,8,14-17}. FeRh in particular has been earmarked for use in creating thermally-assisted magnetic recording (TAMR) media when paired with iron-platinum (FePt). A current limitation in modern hard drive technology is the size of an individual bit, which is essentially a single ferromagnetic domain. Reducing the size reduces the magnetic energy relative to the local thermal energies, meaning temperature variations will destroy the data on the drive. This is known as the superparamagnetic limit¹⁸. TAMR is capable

of bypassing this limit by heating FeRh-FePt bilayers to a temperature where FeRh is in the FM phase. At this temperature, the coercivity (the applied field needed to reduce magnetisation to zero) of the FePt layer drops via an exchange spring mechanism after which the data is written to the media and the temperature cooled to the AFM phase¹⁹. There is also interest in applying FeRh as a memory resistor or memristor, a long-theorised circuit component whose resistance is dependent on the history of current that has flowed through the device^{20,21}. By applying a magnetic field when FeRh is in the FM phase, the direction of the magnetic moments are retained in the AFM phase upon cooling, then using an AFM equivalent of anisotropic magnetoresistance to measure an electrical reading²². Memristors may be used as a replacement for random access memory (RAM) in computers, allowing fast read/write times of the memory whilst retaining the data when no current is flowing.

Although the FeRh phase transition has been known for several decades, there is still much about the phase transition of both FeRh and other magnetostructural materials that is still currently unknown, in particular the mechanism for the transition change and whether it is caused by strain, magnetic or electronic change. Time resolved studies using femtosecond lasers suggest that the change is primarily driven by magnetism^{23,24}. Recent research on FeRh thin films using neutron scattering experiments have found the existence of FM signal within the AFM phase²⁵ that appears at the interfaces FeRh makes with its substrate and a capping layer.

This thesis aims to further understand the FeRh phase transition using transmission electron microscopy (TEM) on thin film samples. TEM is a powerful technique that is capable of providing chemical, structural and magnetic data of a material provided it is thin enough for high energy electrons to transmit through it. FeRh has been briefly studied using TEM but mostly as a means to confirm nanoparticle sizes or crystal structure²⁶⁻²⁸. Thin film samples are grown using dc magnetron sputtering and are then prepared for the TEM using either a conventional ion polishing method or focused ion beam. There are several objectives for this research to achieve. Cross-correlation

of thickness and roughness measurements for FeRh films and any capping layers compared to bulk characterisation methods can confirm the effectiveness of the growth procedure. The different TEM sample preparation techniques can be investigated to confirm the optimal method for creating cross-sections and plan view samples. The effects of novel chromium and tungsten capping layers to affect the transition can be explored, examining strain and interdiffusion. The ideas and issues raised in other work may be investigated, in particular the effects of the interfaces on the FeRh phase transition and the transition dynamics, applying advanced TEM techniques in a novel situation such as scanning TEM (STEM) electron energy loss spectroscopy (EELS) and differential phase contrast (DPC) magnetic imaging.

This work has been divided into eight chapters including this introduction:

- Chapter 2 provides a review of magnetism and phase transformations as well as literature on the FeRh system itself .
- Chapter 3 details the experimental methods of the characterisation techniques applied in this research, with particular emphasis on the TEM and the sample preparation techniques. Other techniques such as X-ray diffraction (XRD), X-ray photoelectron spectroscopy (XPS) are detailed as well. Techniques not performed as part of this research but still relevant such as sample growth, X-ray reflectivity (XRR) and neutron diffraction are discussed as well.
- Chapter 4 explores the initial characterisation of the FeRh system in the TEM, characterising the structure of the thin films and comparing to characterisation methods of bulk thin films, in particular XRD and XRR, with an aim to confirm the viability of sputter-deposition for FeRh growth.
- Chapter 5 describes the local chemistry of FeRh at the interface it makes with a substrate of magnesium oxide (MgO) to see if composition changes take place, which may help to provide an explanation for the latent ferromagnetism spatially shown to be here in the antiferromagnetic

phase.

- Chapter 6 examines the local chemistry of FeRh at the interfaces of various capping layers, including aluminium, chromium (Cr) and tungsten (W). Cr and W are novel choices for capping layers in an attempt to apply epitaxial strain to the FeRh and affect the transition temperature. It is therefore important to understand if compositional changes at the interface exist as they may play a role in affecting the phase transition alongside strain effects.
- Chapter 7 investigates the FeRh phase transition through a series of heating and cooling experiments, observing changes in strain and magnetism with the aim of understanding the dynamics of the transition and how epitaxial growth and strain play a role.
- Chapter 8 discusses the conclusions reached by this thesis as well as potential for future work.

2 Background

2.1 An Overview of Magnetism

It would first be prudent to talk about the concepts of magnetism and magnetic materials before applying the concepts to a specific material. Magnetic interactions arise from the movement of charge such that a force, \mathbf{F} , acts upon a charge, q , when moving with a velocity, \mathbf{v} , in a magnetic field, \mathbf{B} ²⁹.

$$\mathbf{F} = q(\mathbf{E} + \mathbf{v} \times \mathbf{B}) \quad (1)$$

Certain properties of a magnet (the force it can exert on an electric current and the torque a magnetic field will exert on it) are affected by its magnetic moment. The magnetic moment is a vector, the direction of which defines a north and a south on a magnet. The definition of a magnetic moment is typically related to a closed current-carrying loop. This can be easily demonstrated using the right-hand rule by curling the fingers around to be analogous to the current in the loop with the thumb pointing upwards in the direction of the magnetic moment. A general expression for the magnetic moment, μ , for a current density \mathbf{J} where \mathbf{r} is a vector from the origin to a volume element, dV , (the radius for a circular path) is:

$$\mu = \frac{1}{2} \int \mathbf{r} \times \mathbf{J} dV \quad (2)$$

The torque, τ , exerted on a current-carrying loop can be described in terms of the magnetic dipole moment, μ .

$$\tau = \mu \times \mathbf{B} \quad (3)$$

Atoms have magnetic dipole moments that can be classically derived from the intrinsic angular momentum (or spin) of the electrons orbiting the nucleus, along with the orbital motion the electrons make as they move. When dealing with magnetic fields passing through a magnetic sample, \mathbf{B} is

often redefined in terms of magnetisation, \mathbf{M} , the total magnetic dipole moment per unit volume in a given material. The magnetic field may now be described as follows, where \mathbf{H} is the applied magnetic field and μ_0 is the permeability of free space.

$$\mathbf{B} = \mu_0(\mathbf{H} + \mathbf{M}) \quad (4)$$

For different magnetic materials, the vector \mathbf{M} can point in the same direction as or opposite to \mathbf{H} . As a result, a dimensionless value called magnetic susceptibility, χ_m , is created to describe the degree of magnetisation in an applied magnetic field.

$$\mathbf{M} = \frac{\chi_m \mathbf{H}}{\mu_0} \quad (5)$$

From here we can discuss different types of magnetism that are relevant to consider here as the magnetic susceptibility determines the type of magnetism a material exhibits.

2.1.1 Paramagnetism

Paramagnetism is an effect present in materials where the atoms have permanent magnetic moments that interact very weakly, providing an extremely small magnetic susceptibility. If the material is placed in the absence of an external magnetic field, the moments are randomly orientated (figure 1). However, in an external field the magnetic moments attempt to align themselves parallel to the applied field. The magnetic moments can be randomly orientated due to thermal energy, therefore the degree to which the moments align is dependent on temperature and the strength of the external B-field. Typically, the value of $k_b T$ (thermal energies) is around two orders of magnitude above $\mu \cdot B$ (magnetic energies) so paramagnetic materials become apparent at very low temperatures or very high B-fields.

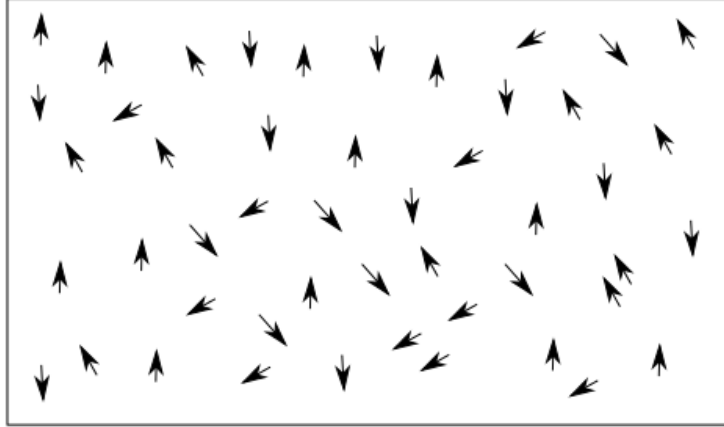


Figure 1: Diagram demonstrating the random nature of paramagnetism due to the thermal energies of the system. There is no overall order in a paramagnetic material (and therefore no magnetic moment) until thermal energies are overcome, by either a very low temperature or a very strong applied field.

2.1.2 Ferromagnetism

Ferromagnetism is the most widely-known form of magnetism. Its origin can be found from interactions between electrons in an a partially filled valence band or from interactions of magnetic moments between neighbouring atoms and molecules³⁰. The latter is due to the exchange interaction, a quantum mechanical effect that occurs when wavefunctions of identical particles overlap. This can affect the expectation values of the energy or distance of these particles. For example, identical bosons (with symmetric wavefunctions) appear closer together whilst identical fermions (with antisymmetric wavefunctions) appear farther apart. In a ferromagnetic material, the wavefunctions of unpaired electrons in adjacent atoms overlap, distributing the electric charge over a wider area. The electrostatic energy of spin-parallel electrons is then lower than electrons with opposite spins, so it is energetically more feasible for two electrons of the same spin to coexist. In ferromagnets, the exchange interaction is usually much higher than the dipole-dipole interaction,

meaning that the majority of dipoles in the materials will be aligned.

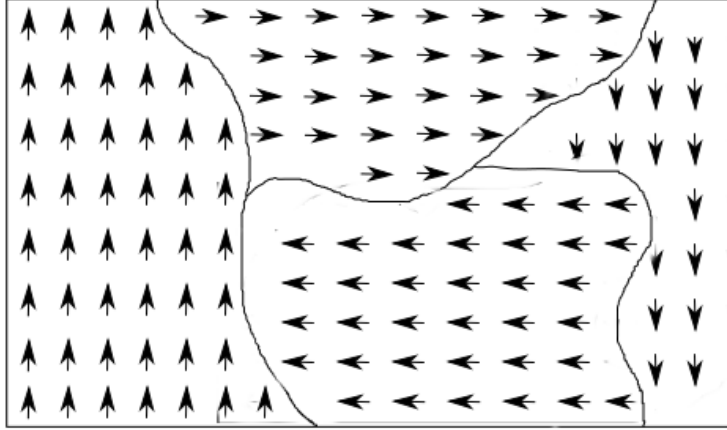


Figure 2: Diagram of ferromagnetic order in the absence of an applied magnetic field. The material is broken into domains, each with their own orientation. The random alignment of each domain cancels the overall magnetic moment of the material. This is analogous to paramagnetic systems albeit on a larger scale.

The exchange interaction keeps spins aligned, but the overall orientation of the system is still not in a particular direction. The expected result would be similar to paramagnetism (i.e. affected by thermal fluctuations) but with many groups of atoms with their spins in the same direction. However, there is an effect called magnetic anisotropy, which gives the spins a preferred dimension to point to. Magnetic anisotropy can be caused by different things, including the shape of the bulk structure and, generally for ferromagnets, the crystalline structure of the magnetic material.

For a perfect, magnetically isotropic material, there is no preferential direction for magnetic moments to align in. Magnetically anisotropic materials will have a preferred direction which is energetically favourable for the system, called an easy axis. This axis is determined by various different types of anisotropy. The most obvious case is shape anisotropy, where the shape of the object will affect the preferred direction of the magnetic field. A spherical object will have no

preferred direction but a typical bar magnet will prefer to align parallel to the long side of the magnet in order to minimise the size of the domain boundaries.

Ferromagnetic materials do not have a very strong magnetisation as expected from magnetic anisotropy initially as the material is split into several magnetic domains, or Weiss domains. Within these domains, the spins are aligned with each other and the random orientation of each domain therefore cancels out any overall orientation on a macromolecular scale, similar to how the individual magnetic dipole moments cancel each other in a paramagnetic material (see figure 2). This happens spontaneously in ferromagnetic materials as it is the lowest energy configuration due to the demagnetising field, reducing the total magnetic moment. If placed in a strong enough magnetic field, the different domains will align parallel to the external field and become magnetised. They remain orientated when the external field disappears, creating a permanent magnet.

The boundary between these magnetic domains is called a domain wall. These walls tend to be ~ 100 atoms thick (although this varies depending on the material's anisotropy) and involves a gradual reorientation of the magnetic moments from one domain to the other.

Crystal defects in ferromagnets result in a gradual change in magnetisation as applied magnetic field is increased. This is demonstrated by the Barkhausen effect, where a magnetisation curve appears quantised due to discrete jumps in the size or orientation of ferromagnetic domains. As the magnetic field increases, whole domains may orientate themselves to the direction of the field and crystallographic defects will cause domains to increase around them until the domain is big enough to encompass it.

If subjected to high enough temperatures, it is possible for the thermal energies to overcome to the magnetic energies of the system and break the orientation of the domains or, indeed, the whole ferromagnet. The point at which this occurs is the Curie temperature, and results in the material making a second order phase transition to a paramagnetic state. This can and has been used as a way of erasing magnetic media in order to write new data, in particular for minidisk players.

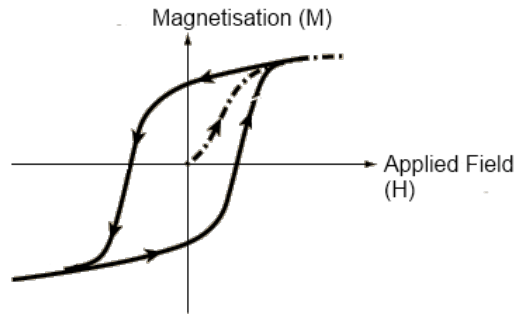


Figure 3: Example of a typical hysteresis loop for a magnetic sample. The sample is still magnetised with no applied field after the material is magnetised to saturation.

Ferromagnetic materials have a hysteresis curve (see figure 3) related to the application of an H-field and the saturation magnetisation of the ferromagnetic material. When in the absence of a field, a non-aligned ferromagnet will have zero magnetisation. As the sample is subjected to an applied field, the magnetisation increases in a non-linear fashion until it is saturated from the complete alignment of magnetic domains. As the applied field is decreased the magnetisation decreases but does not relax back to zero in the absence of an applied field. This is known as remanence. By reversing the direction of the applied field, the magnetisation will revert back to zero until the field is large enough to saturate the sample. Along the way, applying a magnetic field to bring the magnetisation of the sample to zero is known as the coercivity of the ferromagnet. Along with heating to the Curie temperature, the hysteretic nature may be applied as a method for data storage, as a defined magnetisation may be forced with an applied field and removed or reversed altogether with a field in the opposite direction.

2.1.3 Antiferromagnetism

Another form of ordered, magnetism, antiferromagnetism is a similar concept to ferromagnetism. Rather than all spins aligning in a single direction, spins seek to align against directly adjacent spins, as shown in figure 4.

In an antiferromagnet, the spins are found to anti-align relative to their neighbours due to the exchange interaction (a spin-dependent force that acts between particles). When the exchange integral between adjacent spins is negative, the spins tend to align antiparallel to one another. Therefore, at low temperatures an antiferromagnetic order will exist since the thermal energies do not overpower the exchange forces. A simplified antiferromagnetic system (e.g. a CsCl structure like FeRh) may be seen as two separate sublattices, each of which is ferromagnetic with antiparallel spin orientation. It can be derived that in the absence of an applied field, upon heating the magnetisation of each sublattice will see a sharp decrease in magnetisation close to a critical point, the Néel temperature, with the antiferromagnetic properties disappearing above this, where the material will typically become paramagnetic, analogous to the Curie temperature of ferromagnets.

Antiferromagnetism plays a key role in giant magnetoresistance and the operation of spin valves, which together form the fundamental science behind modern hard drive technology and magnetic sensors. The AFM layer acts to pin a FM layer via the exchange interaction while the other FM layer is free to move.

2.1.4 Ferrimagnetism

Similar to both ferromagnetism and antiferromagnetism, a ferrimagnet is a material that has a pair of opposing magnetic moments. Unlike an antiferromagnet, one has a larger moment than the other so acts much like a ferromagnet in the presence of a magnetic field. As with ferromagnets, they have a Curie temperature where above it they are paramagnetic. Ferrimagnets are common in materials where different ions exist, e.g. Fe_3O_4 , where two iron ions (Fe^{2+} and Fe^{3+}) exist. Some

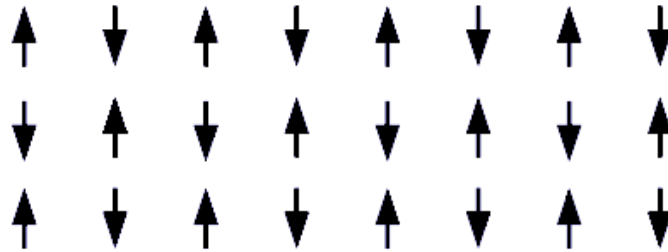


Figure 4: Diagram of the ordering of antiferromagnetic systems. The vectors of the parallel and antiparallel magnetic moments are equal in magnitude, resulting in no measurable magnetic field from the material.

ferrimagnets exhibit what is called a magnetisation compensation point. This is a point below the Curie temperature where the opposing moments are equal, resulting in a zero net magnetic moment.

2.2 Magnetic Materials

One major use of magnets and magnetism is to convert between electrical and mechanical energy. The most prevalent cases of this technique are motors and generators. A generator works by electromagnetic induction. A conductor is rotated within a magnetic field and a force is generated that creates a current in the conductor, thus generating electricity. A motor is effectively the process in reverse. Electrical signals can be converted into audio using magnetism. This is the principle of speakers and headphones, which use a magnetic field to move a diaphragm, a lightweight and stiff material, generating the change in pressure to produce sound. The inverse of this method may be used to create microphones.

In the digital age, magnetic materials have become increasingly more common as a method of data storage. Video and audio cassettes contained a tape with a magnetic coating which can be read using a type of transducer called a tape head. This consists of a magnetic material shaped in a toroid with a very narrow gap. This gap is then filled with a paramagnetic material, which forces

the magnetic field into the magnetic material. The gap may be left empty and air can be used but it does not work as effectively. The field magnetises the tape at that point, writing to it. There is a wire coiled around the tape head at the end opposite to the gap that can either provide a signal for recording to the media or send a signal from the tape to an amplifier to play it back. As a result, the design of the head is fully reversible, allowing recording and playback in the same system.

Modern credit and debit cards contain a magnetic strip that contains important information that ties the card to a particular bank account and what services it is capable of using.

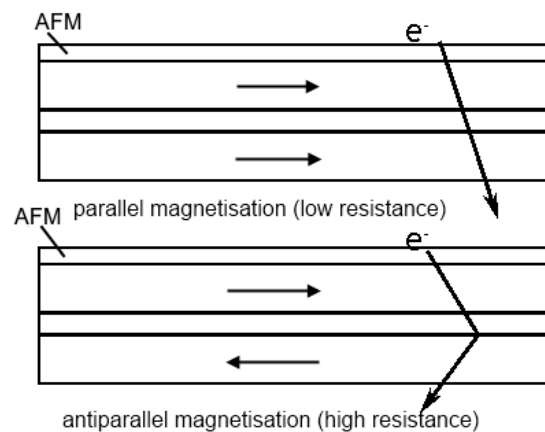


Figure 5: Simple example of giant magnetoresistance. The two ferromagnetic materials can either have parallel or antiparallel magnetisation. If the magnetisations are parallel then the resistance for an electron travelling through the system perpendicular to the magnetisation is low. If the magnetisations are antiparallel, the resistance is high.

By far one of the most important advances in magnetism in recent years, giant magnetoresistance (GMR) has revolutionised hard drive data storage. GMR works on a principle that the resistance of a material can be changed depending on the direction of a magnetised ferromagnetic layer (figure 5). It was initially created by having many ferromagnetic layers separated by an extremely thin non-magnetic material. If the ferromagnetic layers are magnetised parallel to each other, the resistance is low. If they are antiparallel, the resistance is very high (at least in comparison to other

forms of magnetoresistance). More recently, spin valve GMR has become a more useful method. One ferromagnetic layer is pinned (i.e. its magnetisation direction cannot change) with an antiferromagnet. The other layer, however, is free to change with an applied field. It is this method that makes spin valves such a useful device as a read head in a hard drive. As the head moves over a bit (which itself is magnetic) the direction of the unpinned ferromagnet's magnetisation is free to change and thus change the resistance. This resistance can determine if the bit is therefore a 1 or 0.

A recent development in magnetic materials is based around the concept of a magnetostructural transition - that is a material that makes an abrupt phase transformation that involves both a magnetic and structural change. This transition may be driven by changes in applied field, strain or temperature meaning that they are potentially useful for a variety of technologies. For example, these materials may be applied into sensor devices that monitor strain, temperature or magnetic field changes or for use in magnetic refrigeration^{6,7}.

2.3 Phase Transformations

Phase transformations are ubiquitous in materials, manifesting themselves in various different ways and can be defined as the change of a thermodynamic system from one state to another³¹. A very common everyday example would be the melting or freezing of water.

2.3.1 Free Energy

For a system undergoing a transformation with constant temperature and pressure, the total available energy in the system may be defined as the Gibbs free energy which, in its most basic form, can be represented as

$$G(P, T) = H - TS \quad (6)$$

where G is the Gibbs free energy, H is the enthalpy, T is the temperature and S is the entropy. This equation is very flexible and extra terms may be added for other contributions to the system, e.g. applied magnetic field or surface energy. The enthalpy term is a measure of the heat content of the system and can be described as

$$H(P, T) = U + PV \quad (7)$$

where U is the internal energy of the system, P is pressure and V is volume. From this equation it can be seen that enthalpy essentially describes a sum of potential and kinetic energies: the internal energy is potential energy obtained from atomic bonding or interactions and PV arises from motion and vibrations between these atoms. The stability of the system may be determined from the first derivative of the Gibbs free energy. If $dG = 0$ and the free energy is at a minima, the system is in equilibrium. The lowest free energy value is the stable state of the system while any other minima are metastable. For cases where $dG \neq 0$, the system may be described as unstable. Changes in

temperature or pressure will increase the free energy of the system and can move the system from a stable to a metastable equilibrium. Figure 6 shows how stability and equilibria may be represented graphically.

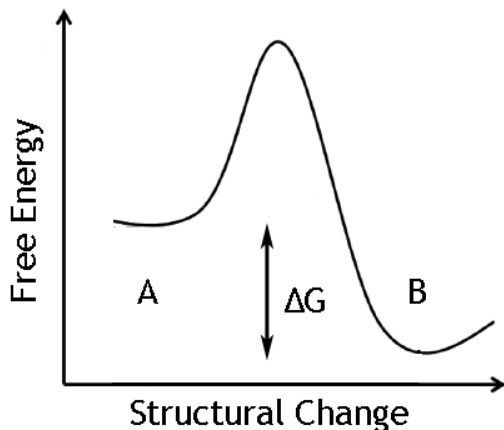


Figure 6: Diagram demonstrating the stability of a system moving from state A to state B. The minimum at A represents a metastable state while the minimum at B represents the most stable state with the lowest free energy.

A phase transformation will occur when there is a difference between the free energies of the initial and final states of the system (e.g. points A and B in figure 6) and may be described as

$$\Delta G = G_f - G_i \quad (8)$$

where ΔG is the thermodynamic driving force, G_f is the free energy of the final state and G_i is the free energy of the initial state. A thermodynamically favourable outcome occurs when $\Delta G < 0$.

If a system is cooled or heated beyond its equilibrium transition temperature, ΔG increases. This is known as supercooling or superheating of a system and is commonly seen in solid to liquid transitions. In particular, it can be seen that a liquid may be cooled below its freezing point

and remain as a liquid. This may only occur if there are no nucleation sites available to begin the transition, usually for a freezing transition the surface energy (which is defined for liquids as surface tension) is responsible for these sites. Nucleation sites bring about the phenomenon known as hysteresis with the nucleation and growth model that results in a gradual change through the transition.

2.3.2 First and Second Order Transformations

Phase transformations may be broadly grouped into two different types: first and second order (or continuous) transitions. These were initially defined by Ehrenfest by the lowest derivative of free energy that is discontinuous at the transition. In first order phase transitions, there is a discontinuity in the first derivatives of the Gibbs free energy, volume and entropy, with respect to temperature and pressure, examples of which are shown in figure 7³².

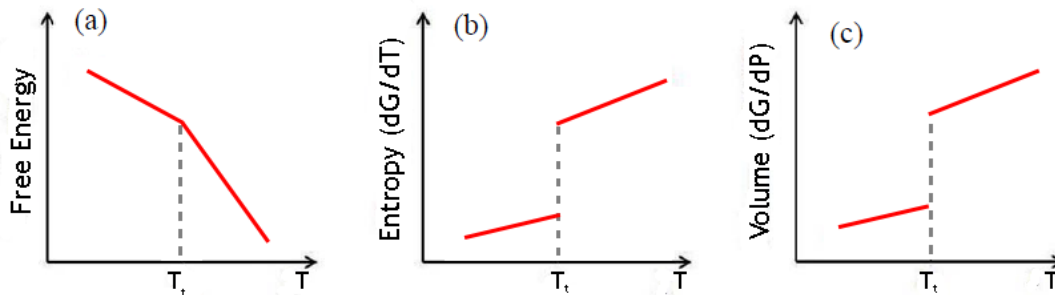


Figure 7: Graphs demonstrating the change in Gibbs free energy, volume and entropy through a first order phase transition. Discontinuities are visible at the transition temperature T_t in the first orders, in this case volume and entropy.

Second order phase transitions are then discontinuous in the second derivatives, in this case the specific heat capacity C_p and compressibility K . This may be seen in figure 8.

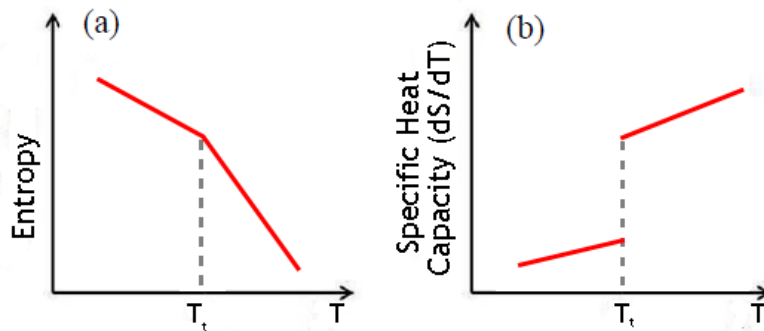


Figure 8: Graphs demonstrating the change in entropy and specific heat capacity through a second order phase transition. Entropy does not exhibit a discontinuity whereas specific heat capacity (the second derivative of Gibbs free energy) sees a jump across the transition.

2.3.3 Diffusionless Transformations

Diffusionless transformations are a particular kind of phase change that occur without a significant long-range reordering of the crystal structure³¹. The effect was first documented in carbon steel by rapidly cooling austenite. The carbon atoms do not have time to diffuse out of the crystal structure as seen with slower cooling to form cementite so instead the fcc austenite makes a transition to a strained bct structure. This so-called martensitic transformation is a first order transition where the atoms do not diffuse but instead the lattice deforms homogeneously to create a different crystal structure. The transformation seen in martensite itself is irreversible however thermoelastic martensitic transformations are capable of having reversible transformations. Coexistence between the parent and product phases (e.g. austenite and martensite respectively) results in an interface plane, the habit plane, between the phases and the presence of laths, or bands of martensite crystal, is seen (figure 9). Not all martensites follow the fcc-bct transformation of austenite to martensite. Alloys such as FeIr and FeMn exhibit a bcc-hcp transformation, MnAu shows a bcc-bct transformation

and TiNi exhibits a B2-B19' transformation³³

Furthermore, some materials that exhibit a martensitic transformation are also what is called a shape memory alloy (SMA). Materials such as AuCd and NiTi^{34,35} are SMAs that may be deformed in its low temperature phase and "remember" their original shape when heated through its martensitic transition. SMAs have wide-reaching potential for engineering and medical applications³⁶ and have in recent times become commercially available for eyeglasses that retain their shape upon bending³⁷.

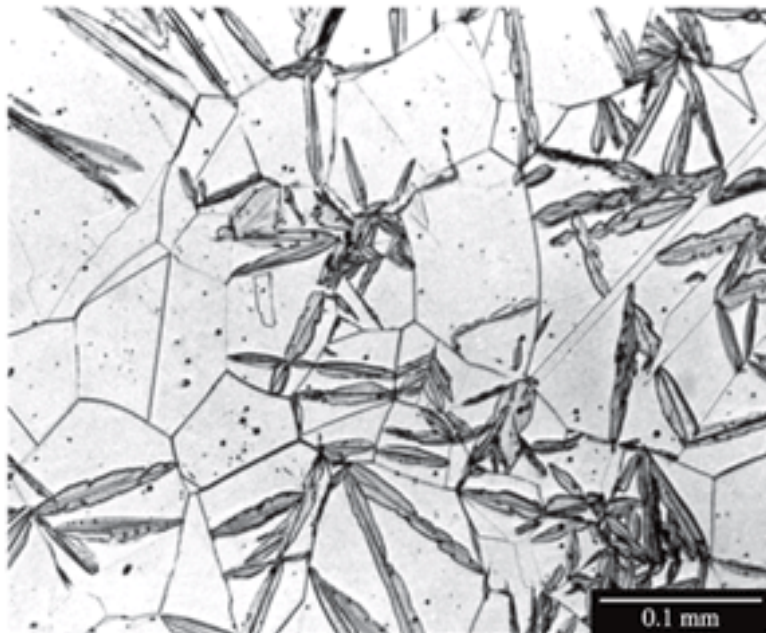


Figure 9: Example of coexistence between parent and product phases, resulting in a lath-like structure³⁸.

2.3.4 Magnetic Phase Transformations

First and second order transitions may be applied to magnetic systems in a similar manner³⁹. In a first order magnetic transition there is a discontinuity in magnetisation at the transition tempera-

ture whereas a second order magnetic transition has no such discontinuity. Second order transitions are naturally seen in ferromagnetic-paramagnetic transitions, for example, in Fe where the magnetisation drops slowly to zero with increasing temperature where it reaches its Curie temperature (figure 10b). First order transitions are less widespread but are seen in systems such as Ni_2MnGa Heusler alloys^{40–42} (figure 10a), Ru-doped CeFe_2 alloys^{10–12} and FeRh (discussed later).

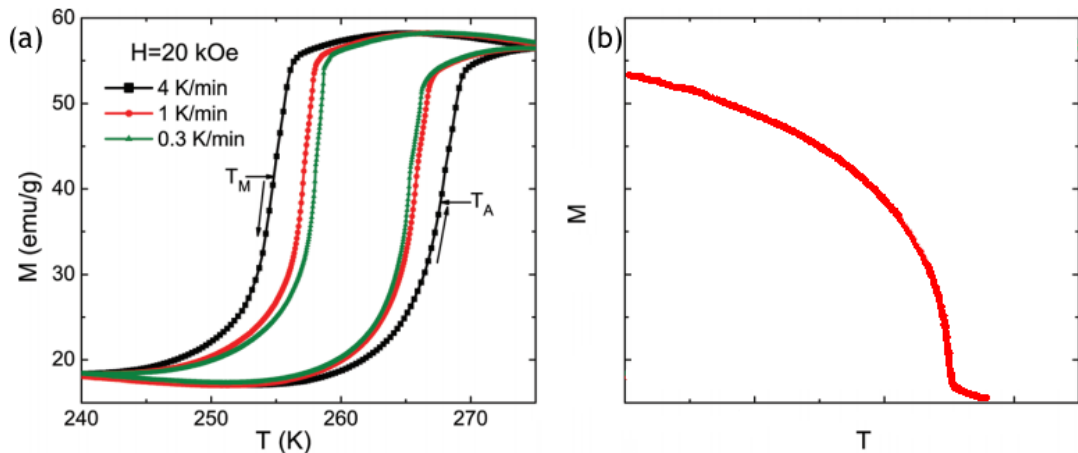


Figure 10: Graphs showing different examples of first and second order transitions in magnetic materials. (a) Change in magnetisation for a single crystal $\text{Ni}_{45}\text{Co}_5\text{Mn}_{38}\text{Sb}_{12}$ Heusler alloy⁴¹. (b) Example of a typical demagnetisation curve of a ferromagnet as it approaches its Curie temperature.

2.4 The Iron-Rhodium System

Iron-rhodium (FeRh) alloys are known to have extremely unusual magnetic properties, making them an area of great interest. Magnetic phase changes, where a system changes from one magnetic state to another, are extremely common. As mentioned previously, ferromagnetic order breaks down at high temperatures to create a paramagnetic state. Other materials may exhibit other changes, with a strong magnetic field or a temperature change yielding different magnetic states. First discovered in 1938 by Fallot⁴³, it was found that iron-rhodium alloys of a roughly equiatomic ratio exist in a CsCl (bcc) structure³, the structure of which is demonstrated in figure 11. At room temperature the system exhibits antiferromagnetic⁴⁴ (AFM) properties. Above a transition temperature of ~ 350 K⁴⁵, the system becomes ferromagnetic (FM), undergoing a first order phase transition with no apparent change to the arrangement of the crystal structure⁴⁶, although there is a discontinuous change in lattice parameter³. Increasing the temperature further, a Curie temperature is found at 675 K¹⁵, where FeRh makes a second order ferromagnetic-paramagnetic phase transition.



Figure 11: Demonstration of the CsCl-type structure of iron-rhodium. The lattice parameter ($a = b = c$) at room temperature is 2.987 Å. The lattice parameter changes to 2.997 Å above the transition temperature.

There are many other characteristics that are associated with this first order phase transition. The lattice parameter makes an isotropic volume expansion of $\sim 1\%$ ⁴⁷, which associates with a

lattice parameter increase from 2.987 Å to 2.997 Å³ (a lattice parameter change of 0.3%). The crystal structure, however, remains the same. The lattice parameter change has been observed via changes in Bragg peaks of the diffraction pattern, as seen from XRD measurements in figure 12. The transition from AFM-FM also yields a resistivity drop and a large increase in entropy. The transition exhibits a 10 K⁴⁸ temperature hysteresis in bulk samples. In the AFM phase there is a magnetisation of 0 emu/g, with a sharp increase to 120 emu/g (with $H_{app} = 5 \text{ kOe}$) when entering the FM phase. The magnetisation at the Curie temperature sees a slow decrease back to 0 emu/g into the paramagnetic phase. Studies of the magnetic moments of the Fe and Rh atoms using Mössbauer spectroscopy have shown that in the FM state a magnetic moment of 3.04 μB and 1 μB are found for Fe and Rh respectively. In the AFM phase, bulk FeRh has no net magnetic moment as expected for an antiferromagnet. However, the magnetic moment within the atoms is purely within the Fe with moments of $\pm 3.3 \mu\text{B}$ and no magnetic moment for the Rh atoms^{49,50}. Band structure calculations determine values for the magnetic moments that correspond with experimental values⁵¹. Photoemission electron microscopy (PEEM) experiments have been used to determine the typical FM domain size, which is found to be of the order of 1 μm ^{52,53}. The phase transition is very sensitive to the ratio of Fe:Rh, the ratio can vary by $\sim 10\%$ (i.e. Fe₄₈-Rh₅₂ to Fe₅₆-Rh₄₄). Beyond this, the material changes phase altogether, with both too much iron or too much rhodium losing the unique magnetic properties. An excess of rhodium leads to a fcc structure³ with a paramagnetic phase. In contrast, Fe-rich samples change the system to a standard ferromagnet with a dominant α' or α phase (both CsCl) depending on the amount of Rh-doping.

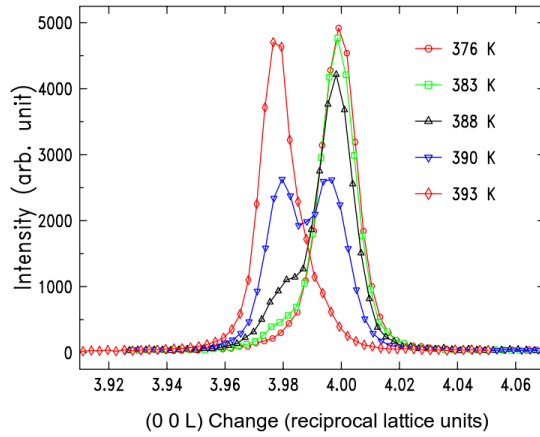


Figure 12: X-ray diffraction peak for (004) FeRh, showing the peak shift corresponding to the 1% unit lattice expansion when heating to the FM phase. The transition experiences a hysteresis from 365 K to 400 K⁵⁴.

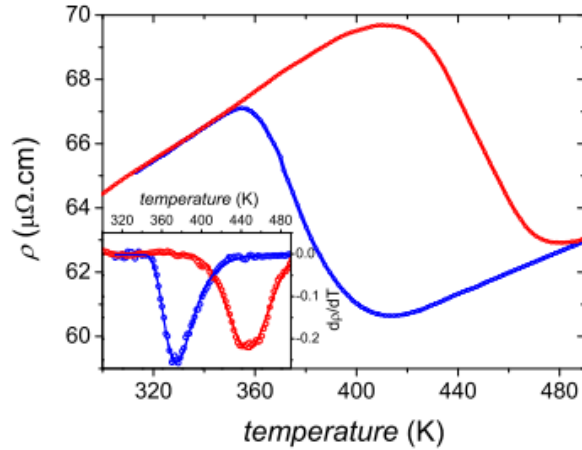


Figure 13: Example of a typical resistivity measurement for FeRh through the transition⁵⁵. The resistivity in the heating curve (red) slowly increases in a linear fashion as is expected for a heated metal. However, there is a characteristic drop as the material makes a transition to the FM phase, after which it begins slowly increasing again. Upon cooling (blue) it can be seen that the resistivity is hysteretic. The inset shows the derivative of resistivity w.r.t. temperature, highlighting the difference in transition temperature depending on direction.

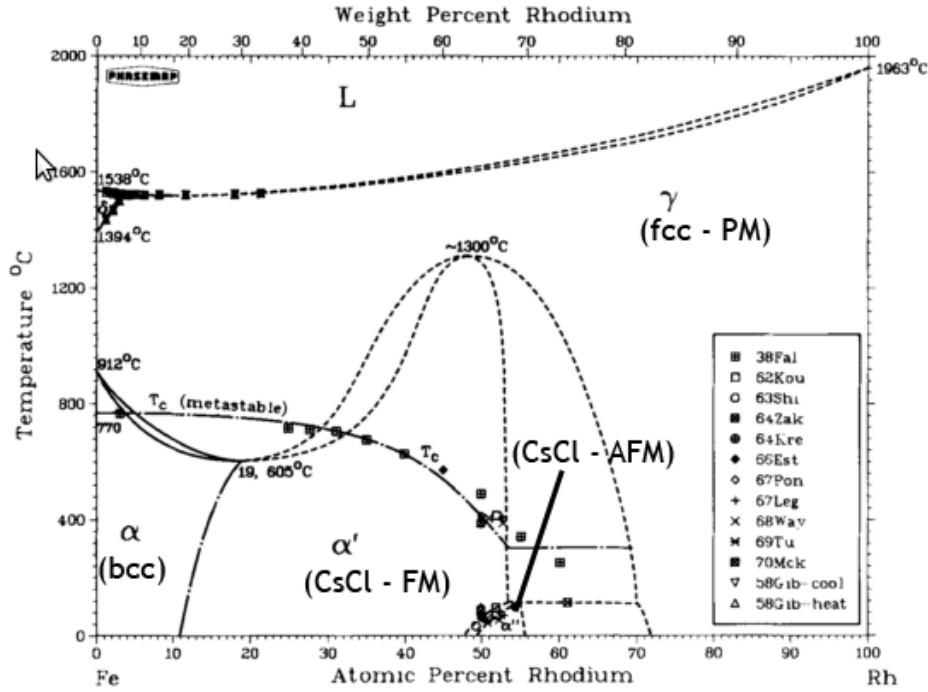


Figure 14: Phase diagram of the iron-rhodium system as determined by Swartzendruber³. The area of interest is the α' section, where the sample is antiferromagnetic. Heating of the sample will cause a phase change into the ferromagnetic α' region.

Growth of FeRh in thin film form is a common method of studying the FeRh system⁵⁶⁻⁵⁸. The differences between bulk FeRh and those in a thin film form are slight⁵⁹. There is a wider temperature hysteresis for thin film samples, with the AFM-FM transition being far less broad than the FM-AFM. However, the applied field dependence for both bulk and thin film samples are essentially the same. It is typically required to anneal thin film samples to obtain the CsCl structure otherwise it is found in a fcc phase instead⁶⁰. It has been shown by Lounis et al⁶¹ through band structure calculations that a thicker FeRh thin film with Rh as a terminating layer will change the magnetic order. Thinner films result in a FM phase whereas thicker films give AFM phases also seen in bulk samples. The same is not true for samples that terminate with an Fe layer on the

surface.

2.4.1 Controlling the Transition

FeRh is not the only material that exhibits transitions between different forms of ferromagnetism. Co/Pd multilayers have been designed to imitate this transition¹³ and Ru-doped CeFe₂ is also known to have a similar phase change¹⁰⁻¹² that instead makes a transition from FM to AFM on heating. However, this transition occurs at temperatures below 100 K whereas for FeRh it makes a transition above room temperature. Many other materials have also been documented⁶²⁻⁶⁵. A unique point of interest in FeRh is the ability to tune the transition temperature both up and down.

The transition can be controlled by various different methods. One such method is by applying a magnetic field as an applied field will help to orientate the spins in a particular direction, eventually overcoming the energies required to pass into the ferromagnetic phase. The transition temperature drops^{3,15} at a rate of 0.8 K/kOe with increasing magnetic field in both a bulk and film state. Increasing the magnitude of the applied field broadens the transition and lowers the resistivity of the sample⁶⁶.

Compositional Changes

As discussed previously and seen in figure 14, the AFM phase only exists for a small subset of Fe:Rh ratios. Within this region, the transition temperature may be increased or decreased by changing the composition. A binary change like this provides some scope to affect the transition. However, it is seen that Rh-rich alloys show a reduction in saturation magnetisation^{67,68}. By comparison, creating a ternary system using a dopant can provide a better way to fine tune the transition. By doping with platinum, iridium, osmium, ruthenium or gold the transition temperature may be increased whilst doping with palladium and nickel will lower the transition temperature^{8,16,17}. The effects of adding Pt in particular have shown⁶⁹ that increasing the concentration will increase

the transition temperature. However, increasing the concentration will also limit the ability for an external field to affect the transition. It has been observed that adding iridium and palladium to FeRh increase the specific heat capacity at low temperatures rather significantly^{70,71}. The majority of research into doped FeRh systems has been performed on bulk samples so there is no guarantee that the effects observed are the same as with thin film samples. However, studies have shown that Pt-doped FeRh exhibits similar properties to its bulk equivalent⁷², suggesting that these dopants may indeed affect thin film samples in similar ways.

Beam Irradiation

FeRh may be forced into a ferromagnetic state by irradiating a sample with an ion beam. By using high-energy heavy ions, it was shown by Fukuzumi et al⁷³⁻⁷⁵ that the transition temperature could effectively be lowered. In areas where the ion beam was applied (used were 120 MeV Ni, 150 MeV Kr and 200 MeV Xe), the ferromagnetic transition was observed at temperatures down to 5 K. Further experiments⁷⁶ demonstrated how irradiation by 0.18-10 MeV ions (H, He and I) can affect the magnetisation. The magnetisation increases with the energy density of the elastic collisions from the irradiations, which disorders the arrangement of the atoms and adds defects to the structure, whilst keeping the CsCl structure. Too high an energy density, however, leads to a loss of magnetisation as the sample changes from a ferromagnetic to paramagnetic phase. The research shows how the magnetic state of the FeRh films can be finely controlled using an ion beam. Focused ion beam systems provide an effective method with which to control the process by making localised changes⁷⁷ and is a useful tool for patterning FeRh⁷⁸.

Pressure and Strain

By applying pressure to FeRh, the transition temperature may be changed. The effects have been well documented for bulk FeRh with the transition temperature increasing with external compressive strain applied^{14,79-81}. While not as extensively studied, it has been seen that the transition temperature may also change if a thin film is strained⁶⁷. By growing an epitaxial layer of FeRh onto a single crystal substrate with a similar but not identical lattice parameter, the film is placed under a compressive or tensile strain near to the interface depending on the lattice parameter of the substrate. A suitable substrate must be similar enough to provide epitaxial matching but different enough to provide enough strain to affect the transition temperature. A compressive strain on the lattice has been shown to increase the transition temperature and a tensile strain applied will cause the opposite effect⁸². It has been suggested that the increased lattice parameter at the interface creates a stable FM phase at the interface, thereby reducing the transition temperature⁸³. Magnesium oxide (MgO) and sapphire (Al_2O_3) are good choices for tensile and compressive strain respectively due to lattice mismatches of $\sim 0.3\%$. MgO has an epitaxial relationship with FeRh of $\text{FeRh}[100](001)\|\text{MgO}[110](001)$ and sapphire has an epitaxial relationship of $\text{FeRh}(111)\|\text{Al}_2\text{O}_3(0001)$. In both cases, it is seen that the interfaces create a slight tetragonal distortion onto the FeRh layer in the AFM phase, although the unit cell volume remains approximately the same⁸².

Film Growth Conditions

Initial thin film growth experiments by Lommel tested various potential methods for producing an FeRh film⁸⁴. It was found that depositing alternating layers of Fe and Rh produced a broad magnetic transition while sputter deposition and codeposition from separate sources produced no magnetic transition. It has since been shown many variables in film growth such as the post-

deposition annealing temperature and the atmosphere of the deposition chamber can affect the final film⁸⁴⁻⁸⁷. The annealing process, however, is key to producing a sample that has both the correct CsCl structure and a sharp transition, as shown in figure 15. It is seen that annealing temperatures of about ~ 870 K produce a sharp transition, with a broader transition paired with a lower transition temperature as the annealing temperature is decreased^{84,86}. At lower annealing temperatures, it is suspected that the occurrence of other crystal phases cause the aforementioned issues⁸⁶. Sample thickness also plays a role in affecting the transition, with thinner samples shown to have a lower transition temperature and a more stable FM phase^{88,89}.

It has also been seen that by growing FeRh at high temperatures with an intention to grow a film ~ 10 nm in thickness results in an island-like structure instead of the anticipated film⁹⁰. There are three different ways of thin film growth: Volmer-Weber (island growth), van der Merwe (layer-by-layer growth) and Stranski-Krastanov (layer then island growth). Here the FeRh has grown via Volmer-Weber growth, which has also been confirmed in other research⁹¹. The islands themselves show a strong phase coexistence in the room temperature phase and a very broad temperature hysteresis which has led to the conclusion that there is a lattice parameter gradient with the core and the shell of the nanoislands exhibiting different lattice constants and, in the nominally AFM phase, different magnetic states.

FeRh Nanoparticles

In a similar context to the aforementioned FeRh nanoislands, FeRh nanoparticles are another example of a nanostructured material designed in an effort to manipulate the phase transition⁹². Magnetic nanoparticles have potential uses in extremely dense magnetic data storage. Ferromagnetic nanoparticles can contain a single domain, providing the potential for extremely small and defined magnetic domains and, as a result, larger storage density. As a result, there is a demand to create FeRh nanoparticles with consistent sizes and compositions. A typical method⁹³ used involves

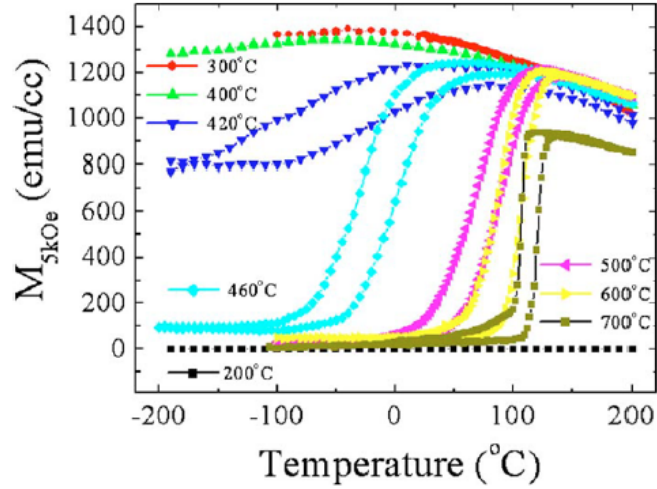


Figure 15: Magnetisation against temperature for FeRh films annealed at various temperatures. Higher annealing temperatures result in a sharper phase transition ⁸⁶.

the co-reduction of two compounds, iron (II) chloride tetrahydrate ($\text{FeCl}_2 \cdot 4\text{H}_2\text{O}$) and rhodium (III) acetylacetonate in either superhydride or in 1,12-dodecanediol in the presence of oleic acid, oleylamine and phenyl ether under a nitrogen atmosphere. The temperature is increased to 100°C to evaporate the solvents then to 200°C and are then later annealed at temperatures varying between $400\text{--}600^\circ\text{C}$ and 800°C . These are characterised using XRD and TEM to determine the structural order and particle sizes respectively. Using this method, particles with various size distributions have been synthesised, ranging from 4-20 nm. It has been seen that FeRh nanoparticles exhibit an altered phase transition compared to other structures. In particular, there is a large asymmetry in the transition itself with an abrupt AFM-FM transition upon heating and a much broader transition on cooling which continues to low temperatures (figure 16) ⁹⁴⁻⁹⁶. In size selected FeRh nanoparticles of size ~ 3.3 nm, ferromagnetic order exists down to 3 K ⁹⁷.

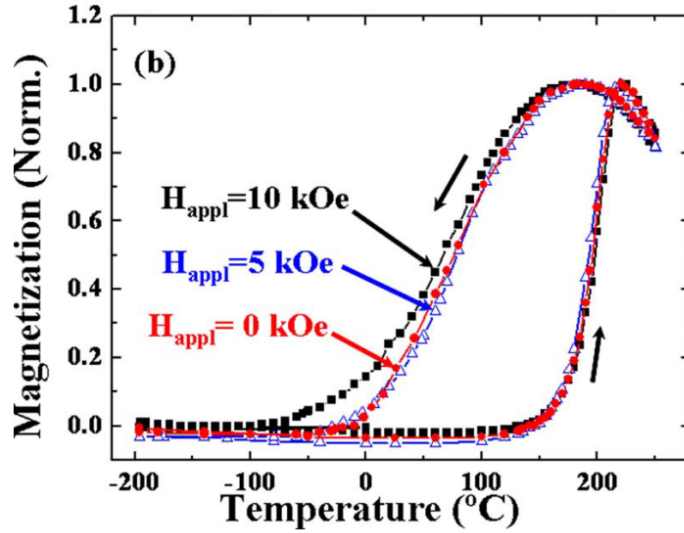


Figure 16: Change in magnetisation against temperature for FeRh nanoparticles. It can be seen that there is a large broadening of the phase transition from the FM-AFM phase while the AFM-FM transition remains largely unaffected⁹⁴.

2.4.2 Dynamics of the Transition

The nucleation and growth of domains into the ferromagnetic transition was explored by Kim et al⁵⁴ on epitaxially grown FeRh films on MgO. X-ray scattering experiments were performed at the Advanced Photon Source synchrotron, observing the FeRh 004 peak. By heating through the transition, the positions of two peaks representing the AFM and FM phases could be seen with position of the peaks directly relating to the lattice parameters at the two phases. Experimental evidence suggested that there was a sudden change in lattice parameter and a coexistence of the two phases (i.e. there is an interface between the two phases - as expected for a first order transformation), indicating a first order phase transition.

By grazing the sample with the incident X-ray beam, surface measurements of the film could be made as opposed to the bulk, with a sharper angle resulting in a smaller scattering depth.

X-ray magnetic circular dichroism (XMCD) experiments also found results to support this phase coexistence. XMCD works on the principles of X-ray absorption spectroscopy in an applied field with the comparison of two sets of data: one with left-circularly polarised light and one with right-circularly polarised light. The differences in these two sets of data can determine magnetic properties of the atoms in a sample, including its spin and magnetic moment. Work by Stamm et al⁹⁸ used this technique to compare the change in the Fe and Rh moments as they pass through the transition. It was found that the magnetic moments increased through the transition when heating. However, the relative moments (i.e. the ratio between the Fe and Rh moments) stays constant. As this is taken over an average of the whole sample, this implies that there is a coexistence of phases as the sample heats to the ferromagnetic phase.

Similar experiments using XMCD X-ray photoemission electron microscopy (XPEEM), a surface-sensitive technique that spatially resolves XMCD data, demonstrate a similar effect, providing a spatial reference to previous XMCD data. Observations of the Fe L_3 edge (at an energy of 705.6 eV) show a similar nucleation of the FM phase, coexisting with the AFM phase^{52,99} as seen in figure 17. It can be seen that upon heating FM domains begin to form at various nucleation sites and at higher temperatures the domains increase in size and align to create the FM phase. The colours correspond to the direction of the Fe magnetic moment.

Finally, magnetic force microscopy (MFM) shows phase coexistence through the phase transition^{100,101} with the presence of both FM signal and regions with no FM signal (which may be inferred as AFM domains). These experiments also suggest that the nucleation of domains occurs at grain boundaries within the FeRh. Further experiments have concluded that the phase transition nucleates within the FeRh film at the film-substrate film before spreading through the rest of the film^{54,82}.

A recent study into the kinetics of heating and cooling show a difference between the directions of the phase change¹⁰². Synchrotron X-ray diffraction experiments observing the (004) FeRh reflection

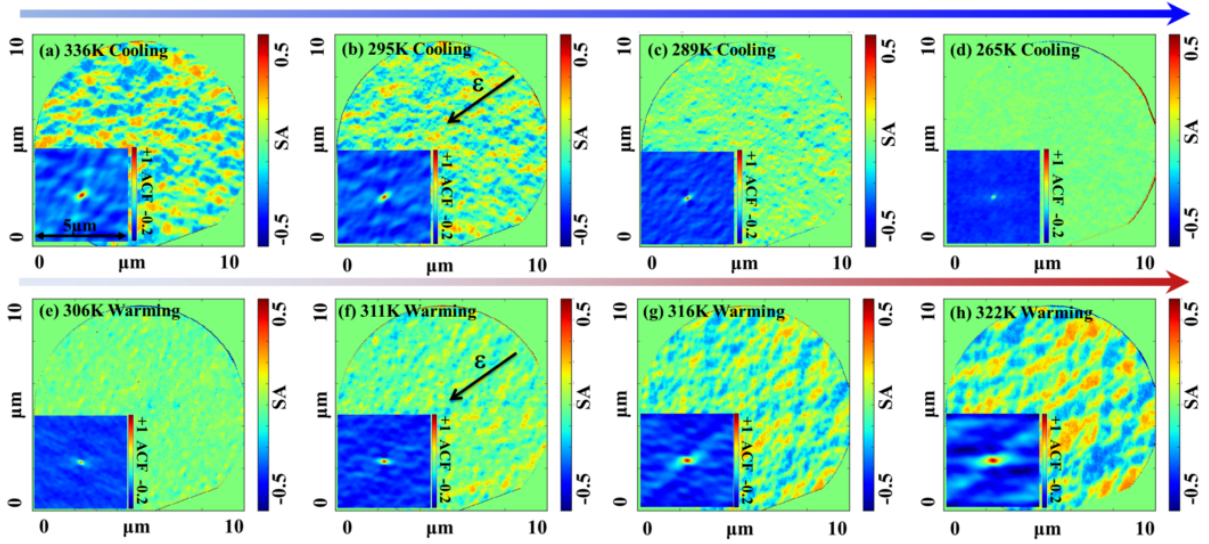


Figure 17: X-ray photoemission electron microscopy (XPEEM) images showing the nucleation of ferromagnetic domains and phase coexistence during the phase transition. The colour represents spin asymmetry (SA), and indicates magnetic moment intensity relative to the vector of photon propagation, ϵ ⁵².

showed a greater separation of the coexisting phases upon cooling than on heating into the FM phase, similar to the melting and freezing of a solid-liquid phase transition. Figure 18 shows that in the middle of the phase transition the cooling curve shows more well-defined peaks (indicating the greater separation) than the heating curve. Studies of the transition in Pd-doped FeRh find a martensitic transformation from bct in the AFM phase to bcc in the FM phase¹⁰³. It is demonstrated that Fe₅₀Rh₄₀Pd₁₀ alloys exhibit a bcc to bct change upon cooling at 175 K. The parent phase (i.e. the bcc phase) exhibits a magnetic transformation at 270 K while the martensite phase is assumed to be antiferromagnetic up to 400 K. FeRh has also been seen to show a temperature memory effect, an effect similar to shape memory effects^{104,105}. This suggests that FeRh may have a martensitic transformation but there is no crystallographic data to confirm this.

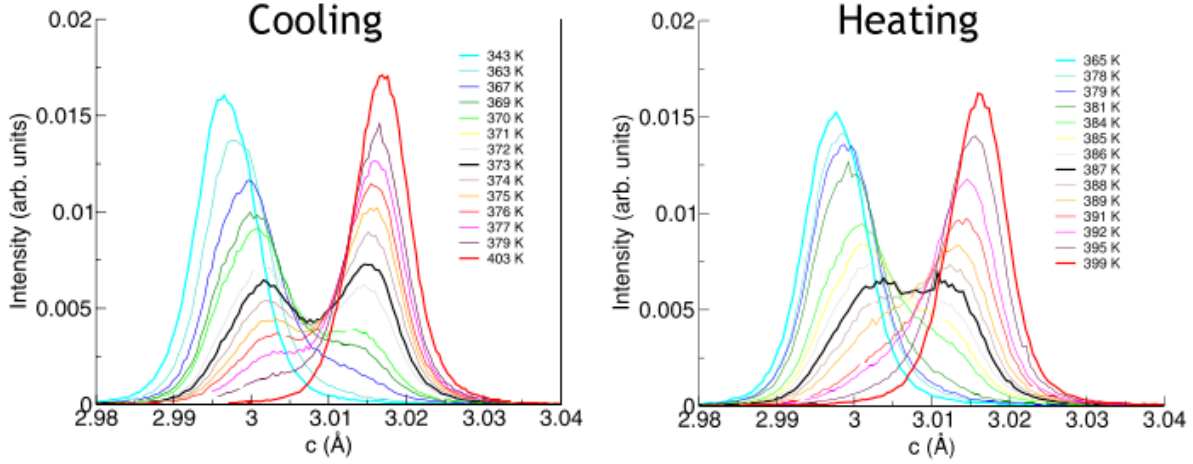


Figure 18: Comparison of the change in the (004) FeRh reflection upon heating and cooling. The black line on each represents the middle of the phase transition, and it may be seen that the cooling curve shows greater separation of the two peaks¹⁰².

2.4.3 Inducing Ferromagnetism via Laser Heating

Currently, there is an interest in manipulating magnetic materials at sub-picosecond timescales by laser heating with femtosecond laser pulses. Initial research with magnetic materials showed^{106,107} how a laser pulse could drop the magnetisation of a ferromagnetic nickel sample within the timescale of a picosecond. The timescales involved means the dynamics of a system can be observed in a way not normally seen. This technique has since been applied to many materials¹⁰⁸ and is also of interest for writing with magnetic data storage devices¹⁰⁹. For FeRh systems, interest arises in attempting a reverse of the procedure outlined by Beaurepaire et al¹⁰⁶, i.e. the generation of ferromagnetic order in a system. A typical experimental procedure involves a thin film of FeRh with a typical thickness of 100 nm. A Ti:sapphire-based laser is used with a wavelength of 800 nm^{23,24}.

The first major experiments²⁴ demonstrated experimentally that magnetisation increases rapidly in the sub-picosecond timescale and then continues to increase over a much slower rate until it

reaches a maximum at ~ 30 ps, as shown in figure 19. The lattice parameter change here is seen to lag behind the generation of magnetisation in the domains. These results suggest that the transition is of an electronic origin. Further work has been done with femtosecond lasers²³. The

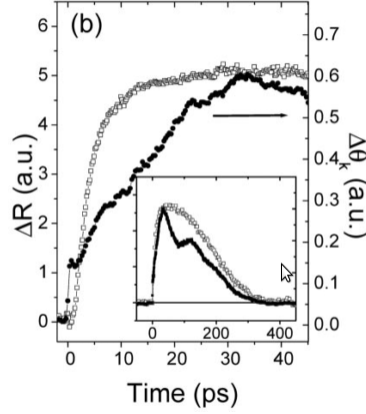


Figure 19: Example of the change in magnetisation when heated by a picosecond laser. The open circles show the magnetisation increase while the filled ones are an example of the lattice parameter change. ΔR shows the change in reflectivity (measuring lattice expansion) while $\Delta\theta$ shows the change in magnetic polarisation²⁴. The inset shows the full changes in magnetisation and lattice parameter over 400 ps.

work by Bergman et al suggested¹¹⁰ that the growth of magnetic domains occurred within the first 10 ps. In the following 50 ps afterwards, a gradual alignment of the domains with each other occurs.

Research by Radu et al¹¹¹ showed that ferromagnetic order is generated within 100 ps for both the Fe and Rh atoms. The data showed that when the AFM-FM transition temperature was reached, there was a coexistence of both phases. At the same time, the lattice expansion through the transition occurs on a ps time scale. Since this occurs on a shorter time scale, it is implied that the transition is controlled by the lattice expansion but the time resolution is not high enough to confirm this and these data do not fit with either previously mentioned femtosecond laser experiments or

the potential theories to explain the phase transition.

2.4.4 Latent FM in AFM phase

Experiments with polarised neutron reflectometry²⁵ revealed, for 50 nm FeRh epilayers grown on MgO and capped with 2 nm of MgO, after cooling through the transition to the AFM phase there were still latent FM moments in the film, as demonstrated in figure 20 by the increase in magnetic scattering length density (SLD). The measurement of SLD arises from measuring the reflectivity as a function of the spin eigenstate of a neutron being parallel or antiparallel to a direction defined by an applied magnetic field. For the magnetic SLD profiles, the value is zero for AFM domains and non-zero for FM domains. The structural SLD changes depending on the density, meaning different elements and isotopes will yield different values. The results show that the difference in magnetic phase is constrained to 6-8 nm from both cap and substrate interfaces. It is theorised (by Fan et al)²⁵ that diffusion at the interfaces and imbalances in the Fe:Rh ratio could influence this metastable phase. Structural scattering length-density information shows there could be a change in composition or density close to the interface, as shown in figure 20. Studies of capping layers in stabilising a FM layer at the interface using XMCD find that oxidation of capping layers inhibits the interfacial FM phase while certain metallic caps cause interfacial FM due to interdiffusion and the creation of a doped FeRh alloy¹¹².

2.4.5 Theories to Explain the Transition

One key outstanding question of the FeRh system is whether the lattice expansion causes the magnetic transition or vice versa. Various theories have been put forward to explain the magnetic change by lattice parameter expansion, spin fluctuation and electronic heat capacity changes. Previously the dynamics of the transition change were too quick to isolate whether the magnetic transition or lattice transition is first to occur but the laser heating experiments previously mentioned strongly

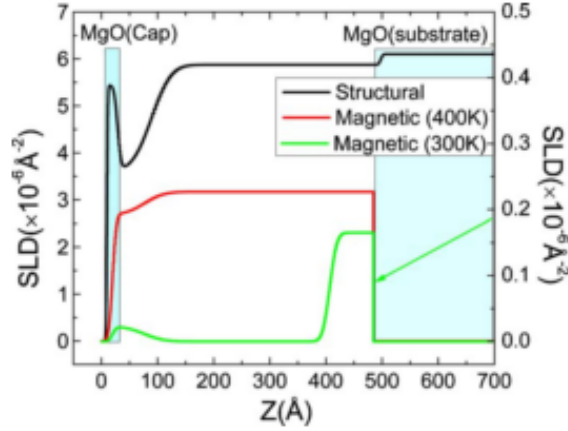


Figure 20: Structural and magnetic scattering length-density (SLD) depth profiles for FeRh above and below the transition temperature obtained from the CRISP reflectometer at ISIS. The increase in the magnetic SLD at 300 K shows the presence of ferromagnetic domains close to both interfaces. The change in the structural SLD suggests a Fe-deficient (Rh-rich) area towards the cap which could explain the FM region²⁵.

suggest that the magnetic transition occurs first.

Exchange Inversion

The theory of exchange inversion put forward by Kittel¹¹³ suggests that the lattice parameter drives the FM-AFM transition. The theory starts by separating a magnetic material into two lattices (in this case an Fe and Rh lattice) tightly coupled together by exchange interactions. It is assumed that there is always a net magnetic moment below the Curie or Néel temperature. The ordered states are assumed to have collinear magnetic structures.

Next we assume that exchange coupling between the lattices is a linear function of the lattice parameter (i.e. it weakens as the atoms become further apart) and crosses zero at a critical value. This means that temperature too can be related to this function (as lattice parameter increases

with temperature). At this critical value the material makes its magnetic transition from AFM to FM and the sign of the exchange coupling switches.

However, exchange inversion does not account for certain characteristics of the transition, such as the disappearance of the Rh moment in the AFM state and an anomalous entropy change^{114–116}.

Electronic Heat Capacity

Another theory^{71,117} suggests that exchange inversion cannot be the reason for this transition as the total change in entropy of the system cannot be explained solely by the entropy change from the lattice parameter increase. The theory put forward by Tu et al is that changes in the band structure and the associated entropy change are the driving force for the transition.

Spin Fluctuation

The most recently put-forward theory for the transition is by Gruner et al¹¹⁸. The work acknowledges that the electronic heat capacity theory put forward by Tu et al is along the right path, but makes assumptions that may not apply for a real system.

Instead, it has been suggested that the competing magnetic states of the Rh atom which, depending on the phase of the system, either has a magnetic moment of 0 or 1 μB . Recent theoretical studies using density functional calculations suggest that this change in electronic structure is the key for driving this transition^{119–121}. A further theoretical approach using atomistic spin dynamics finds agreement with the FM response driving the phase transition as seen in laser heating experiments¹²².

2.4.6 Uses of Iron-Rhodium

FeRh in a thin film form could be applied to data storage or microelectromechanical systems¹⁹. Currently, standard magnetic media relies on statistically averaging large amounts of weakly-interacting

magnetic grains to form a single bit due to the likely issues of heat affecting the data. For modern hard drives, the data density has been increased by reducing the size of these grains. However, this will reduce the magnetic energy contained in the grain and, eventually, the energy will decrease to around or below the thermal energy (kT) of the grain. This is known as the superparamagnetic limit. FeRh may be used as a thermally assisted medium as it has very high magnetic energies compared to that of currently-used materials at similar grain sizes. To record media, the FeRh must first be heated, unlike current materials. This technique allows limitations in magnetic recording to be overcome¹²³. For non-FeRh based systems this is not a viable method as the writing needs to be done near to their Curie temperature (which is typically well above 300 °C), which can result in large thermal stresses. It is also difficult to limit the temperature change to anything beyond the one domain of interest. FeRh is of interest by pairing it with a layer of FePt^{124,125}. The bilayer may be heated, with the FeRh making a transition into the FM state. Via an exchange spring mechanism¹²⁶ the coercivity of the FePt layer lowers and thus makes writing of bits possible. As the limit of data density for standard magnetic data is reached, FeRh may be used to overcome the limitation and continue in the trend of creating higher and higher density magnetic storage.

FeRh also has a use in a memristor device²². A memristor was, until recently, a component of electrical circuits theorised by Leon Chua in 1971 that fitted as a fourth core component along with the resistor, the capacitor and the inductor. A memristor is unique in that its electrical resistance is dependent on the previous charge that has flowed through the device, even when turned off. This would allow a memristor to be used for data storage whilst having extremely fast access times due to the electrical nature of the reading and writing.

Another potential use involves using the FeRh as a nanosensor, capable of providing an easy way of detecting a specific temperature change as dictated through doping the material to the desired temperature, providing a magnetic field that may be detected as the FeRh makes its transition.

3 Instrumentation and Theory

3.1 Introduction

The ultimate goal of this research is to use transmission electron microscopy (TEM) to provide structural and elemental analysis of FeRh to better understand the phase transition. This chapter provides background information regarding the growth process for thin films and, particularly, the FeRh films characterised here. Bulk characterisation techniques are discussed and outlined next, including X-ray photoelectron spectroscopy (XPS), X-ray diffraction (XRD) and X-ray reflectivity (XRR), before talking about the sample preparation process for making TEM cross-sections via both a mechanical process involving grinding, polishing and ion beam thinning as well as using a focused ion beam (FIB). Also discussed are a brief overview of the inner workings of a TEM as well as various characterisation techniques used in the TEM such as high angle annular dark field (HAADF) scanning TEM (STEM), energy dispersive X-ray spectroscopy (EDX), electron energy loss spectroscopy (EELS) and differential phase contrast (DPC) magnetic imaging.

3.2 Thin Film Growth

In order to generate thin films, a deposition method needs to be used that can be well-controlled. In most cases, the film must be grown slowly to achieve as uniform a film as possible. It typically involves depositing a chosen material onto a substrate. The techniques of thin film deposition can be placed into two broad categories, physical and chemical deposition methods. The latter category typically involves a liquid undergoing a chemical reaction at or above a substrate, leaving a solid layer on top. Physical deposition methods involve ejecting material from a target onto the substrate of choice and have been the preferred method of FeRh film preparation for most research groups, and indeed the typical method of choice for metallic thin films as it provides better control over interfaces.

3.2.1 Molecular Beam Epitaxy

Molecular Beam Epitaxy (MBE) is similar to evaporation techniques but instead performed in an ultra-high (10^{-9} Torr or lower) vacuum. MBE deposits material extremely slowly ($\sim 1 \mu\text{m/hr}$), allowing the films to grow epitaxially, i.e. a monocrystalline structure is deposited onto a monocrystalline substrate. The typically used method is solid-source MBE, where pure samples of the thin film desired are heated in Knudsen effusion cells until the material begins to sublimate. These gaseous particles may then condense on the substrate. In the case of certain compounds, the elements are heated separately and fired at the substrate where they may react with each other, forming a single crystal thin film.

The desired thickness of the film can be controlled to an extremely precise level. Reflection high energy electron diffraction (RHEED) is used to monitor the deposition of atoms. This connects to a computer that controls a shutter, stopping the beam altogether. The time for a single atomic layer to grow is ~ 5 s while the shutter takes 0.1 s to close. This allows a fine control of the film thickness to a single layer of atoms.

3.2.2 Direct Current (DC) Magnetron Sputtering

Sputtering is a process where a stream of energetic particles collide with a target sample, causing the ejection of atoms from the target. In a typical sputtering environment, ions from an argon source are accelerated towards a target with a pressure of 1×10^{-3} Torr. A magnetron generates a magnetic field surrounding the target that confines the plasma near to the sample, allowing the plasma to be sustained at a lower temperature. The argon ions collide with the target surface, causing the ejection of atoms (and a small percentage of ions), which travel in a ballistic trajectory until stopped. This results in a coating of atoms across the chamber, including any potential substrate chosen to deposit the film on. As the ejected material is not ionised, it is unaffected by the magnetic field generated by the magnetron and passes straight through.

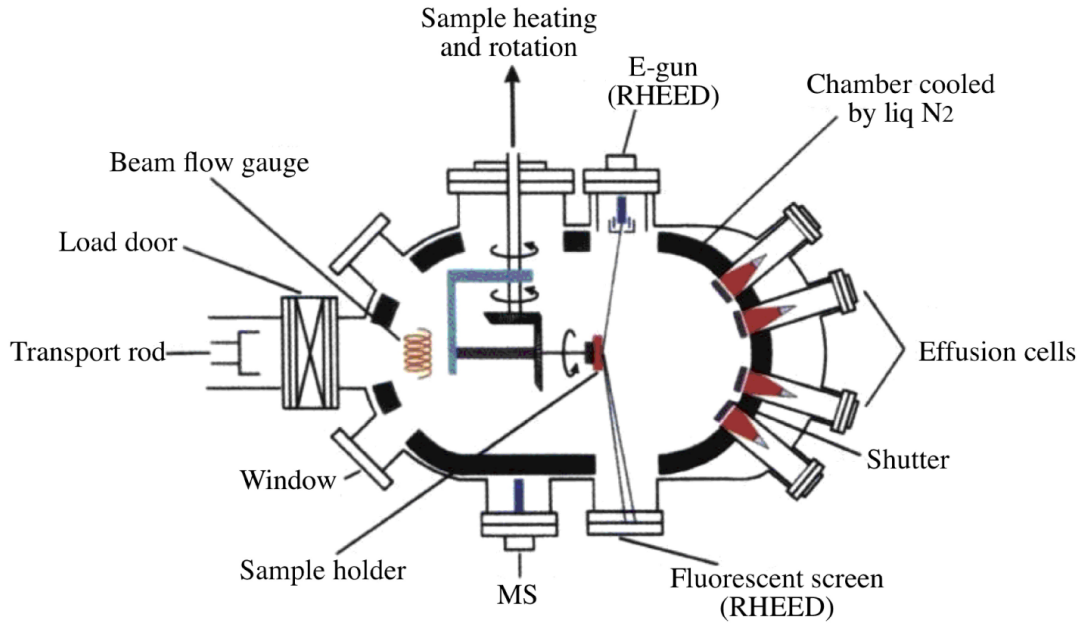


Figure 21: Schematic of a molecular beam epitaxy process¹²⁷.

Iron and rhodium are sputtered from a target with a $\text{Fe}_{47}\text{Rh}_{53}$ ratio. The substrate is heated to 870 K and the power is chosen to deposit at a rate of 0.4 \AA/s with a pressure of 4×10^{-7} Torr which then increases to the order of mTorr when the Ar gas is flowing. The substrate temperature is maintained at a temperature of 600 °C. The films are then annealed for 60 minutes at ~ 970 K. The substrate temperature is then lowered to room temperature. The thin film is subsequently capped with any required layer, which is typically a tungsten or chromium layer with an aluminium cap to prevent oxidation of the film. Deposition of these layers is done below ~ 370 K to prevent any potential interdiffusion into the FeRh layer⁵⁵. Sputter-prepared samples were prepared by Mark de Vries and Chantal Le Graët at the Leeds condensed matter physics department. All samples

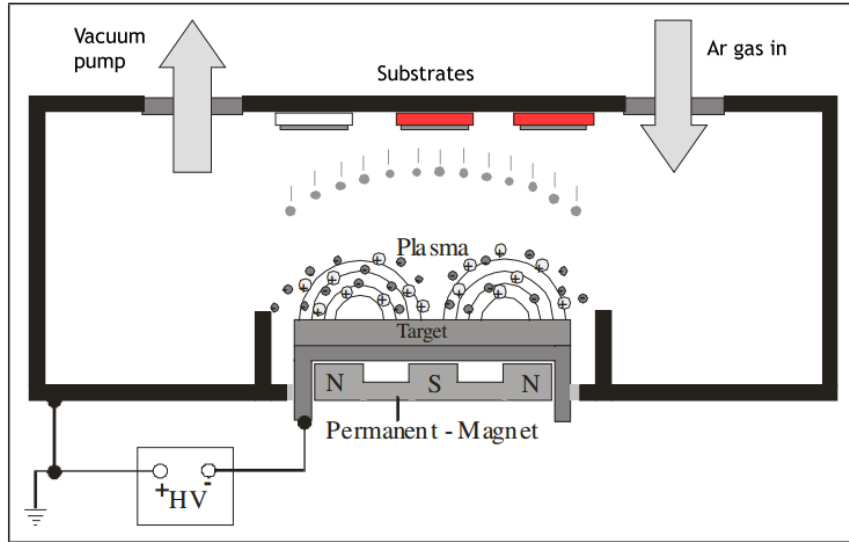


Figure 22: Schematic of a sputtering process¹²⁸.

discussed within this thesis were prepared via this method.

3.2.3 Other Methods

Of the other techniques available, electron beam evaporation is the only one that has been applied to FeRh^{125,129}. The general technique involves bombarding a target with an electron beam. The electron beam causes atoms to eject from the target in a gaseous form. These atoms then form a thin coating around the chamber in line of sight from the target area.

As with other physical deposition techniques, the chamber is pumped to a low pressure (10^{-6} Torr). Multiple electron beams are focused towards ingots of the material chosen to deposit at an accelerating voltage of ~ 25 kV. The beam hits, releasing mostly thermal energy. This causes the ingots to heat up and melt, while the vacuum conditions allow the material to evaporate. While most of the material ejected covers the interior of the vacuum chamber, the substrate is positioned near to the target and is set on a rotating plate to ensure an even coverage of material. The deposition rate

can vary greatly, from 1 nm to a few microns per minute. As the deposition rate can be so high, electron beam evaporation can be an effective method for generating good quality thin films on an industrial scale.

3.2.4 Comparison of Growth Methods

As briefly mentioned, the growth methods discussed above have particular strengths and weaknesses. MBE-grown samples are typically very high quality due to the slow growth and fine control this gives when combined with a fast closing shutter. However, for larger scale application MBE is expensive and not very effective for growing multiple samples. Sputter-grown samples are cheaper to make than MBE samples and provide the same epitaxial growth but do not provide the same fine control. As a result, thicker films may suffer from greater surface roughness. There is also potential for the argon in the chamber to implant in the sample. Finally, evaporation is more cost-effective for larger scale applications than both MBE and sputtering but can suffer from issues with poor growth. If the filament begins to degrade then the growth rate will be uneven and scattering of the sublimated material in the chamber's vapour cloud can result in non-line of sight growth. Both of these may result in non-uniform film growth.

3.3 X-ray Diffraction

X-ray diffraction (XRD) is a method of determining crystallographic data from a sample. By using Bragg's law as a starting point (equation 9 and figure 23) where d is interatomic spacing, λ is the wavelength of the incoming wave, θ is the incident angle of the wave and n is the order of reflection), the atomic arrangement may be determined through the diffraction of X-rays of a known wavelength which may be measured at discrete angles by a detector relative to the X-ray source.

$$2d\sin\theta = n\lambda \tag{9}$$

Once d -spacings have been determined, the lattice constants for a cubic cell (as is expected for the phases of FeRh, MgO, W and Cr discussed here) may be calculated using

$$\frac{1}{d^2} = \frac{h^2 + k^2 + l^2}{a^2} \quad (10)$$

where a is the lattice constant, d is the interatomic spacing and hkl are Miller indices.

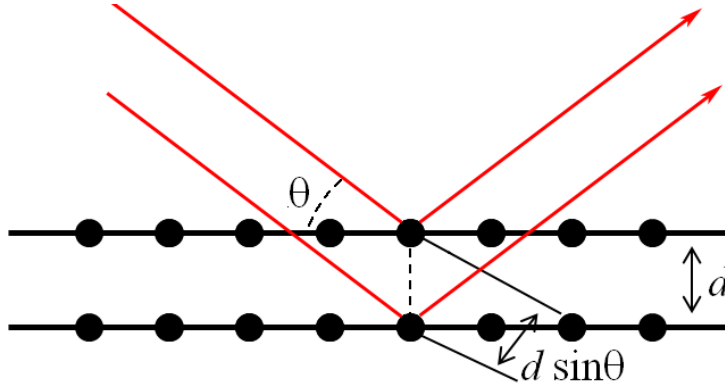


Figure 23: Visualisation of diffraction in a crystal lattice.

The basic premise of an X-ray diffractometer consists of a radiation source, a sample stage and a detector. A filament is heated, producing electrons. These electrons bombard the source, causing core electrons to be emitted. The resulting electron holes are filled by outer shell electrons, creating X-rays with a characteristic wavelength. In the diffractometer used here (a PANalytical XPert MPD), a copper target is used with $K\alpha$ radiation with wavelength 0.15418 nm and $K\beta$ with wavelength 0.13923 nm. Another such source briefly discussed is the use of synchrotron X-rays, generated by the acceleration of electrons to relativistic velocities. Synchrotron sources can result in a very large signal of extremely monochromated X-rays of a particular wavelength suitable for the conditions required for the experiment.

By comparing the relative intensities of the (001) and (002) FeRh reflections, it is possible to

obtain a chemical order parameter, S , that is determined from the fraction of Fe and Rh atoms on their respective sites. It is defined as

$$S = r_{Fe} + r_{Rh} - 1 \quad (11)$$

where r_{Fe} and r_{Rh} are the fraction of Fe and Rh sites occupied by their respective atoms. As such, a perfectly ordered CsCl structure will result when $r_{Fe} = r_{Rh} = 1$, providing $S = 1$ whereas a randomly ordered bcc will arise when $r_{Fe} = r_{Rh} = 0.5$, giving $S = 0$. This is derived experimentally from XRD using

$$S = \sqrt{\frac{I_{001}^{exp}}{I_{002}^{exp}}} / \sqrt{\frac{I_{001}^{calc}}{I_{002}^{calc}}} \quad (12)$$

where I_{00x}^{exp} and I_{00x}^{calc} are experimental and theoretical integrated intensities of the (00x) reflections¹³⁰. For FeRh the square root of ratio of the theoretical values ($\sqrt{\frac{I_{001}^{calc}}{I_{002}^{calc}}}$ is ~ 1.07 , determined using X-ray absorption fine structure¹³¹. For FeRh films discussed here, $S = 0.8$.

The value of S may be derived from an XRD pattern such as the one shown in figure 24. Here, the ratio of the two integrated intensities is calculated to be 0.83. Inputting this into equation 12 gives $S = 0.85$.

3.4 X-ray Reflectivity

X-ray reflectivity (XRR) is a technique often applied to thin film specimens as a means to gauge the growth of the sample. It is capable of obtaining information such as layer thicknesses and interfacial roughness. By firing a beam of X-rays at a grazing angle onto the sample of interest, the reflection of these X-rays may be collected and then analysed. Figure 25 shows an example of a typical XRR curve (blue). Visible are Kiessig fringes, interference of the X-rays that reflect from the thin-film interfaces in the sample, that manifests as a decaying wave. From this it may be inferred that the interfaces are smooth, but otherwise quantitative analysis required fitting of the curve (red). By

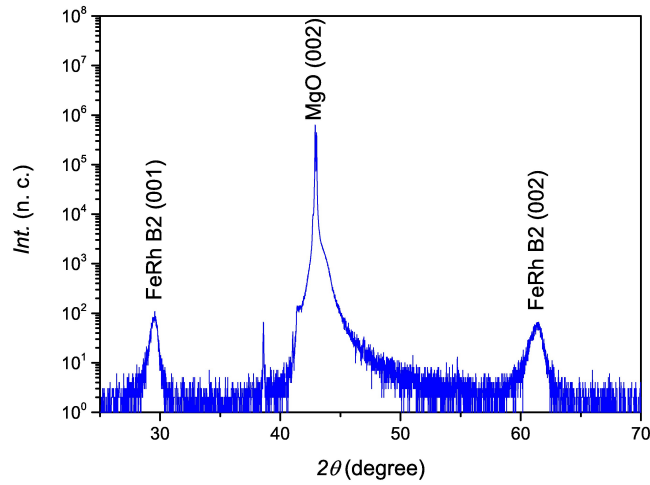


Figure 24: Example of a typical X-ray diffractogram for an FeRh film. The existence of a (001) peak shows that FeRh is in a B2-ordered structure. By collecting integrated intensities of the (001) and (002) peaks an experimental value for chemical order parameter, S , may be determined.

assigning values for layer roughness and thickness, a fit may be created.

3.5 Neutron Diffraction

In a similar fashion to XRD, neutrons may also be used to obtain crystallographic information about a material. Unlike X-ray sources, neutron sources require dedicated facilities for generation, typically using a nuclear reactor or a spallation source - where neutrons are ejected after collisions between a nucleus with a large weight and a high-energy particle. The largest benefit of neutron diffraction is its ability to provide magnetic information about a sample. As neutrons have spin, they are capable of interacting with magnetic moments.

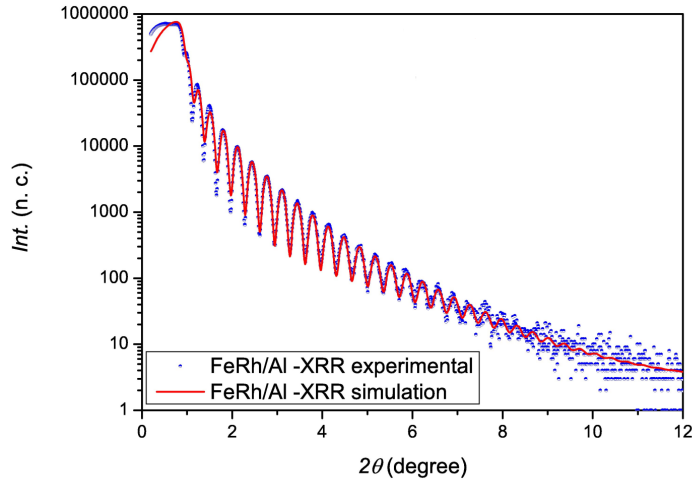


Figure 25: Example of a typical X-ray reflectivity curve with a fit applied ¹³².

3.6 Sample Preparation for TEM

For a sample to be usable in the TEM, it must be processed into a form where it is thin enough to provide electron transparency. The resulting thickness of the sample should be less than 90-100 nm but for certain techniques, in particular phase contrast imaging, thicknesses of 50 nm or lower are required. We are interested in viewing samples in cross-section rather than plan view so the following discussion concentrates on the former. However, both conventional and FIB techniques are able to produce plan view samples with modifications to the process.

Cross-sectional TEM allows a far greater understanding what is happening at and around interfaces. In particular, strain, interfacial diffusion and changes in chemical composition throughout the sample can be determined using cross-sectional TEM. There are three main methods available for metallic thin film samples: ion polishing, focused ion beam and tripod polishing. Here we will focus on the first two.

3.6.1 Ion Polishing Method

Of the two methods used, ion polishing (or the conventional method) is by far the preferred option. It provides samples of an extremely high quality with minimal damage to the specimen (despite the mechanical work done to the sample) and results in an extremely thin area of interest in the middle of the sample. Compared with focused ion beam, it is a slow process with many steps involved. It is also a possibility that the samples will break during the process due to the mechanical nature of the preparation. Figure 26 provides a schematic overview of the procedure.

Creating a wafer stack

Starting with a thin film sample, a Gatan 601 ultrasonic cutter is used with a 5x4 mm² attachment to cut out two areas of interest. In the case of FeRh, the wafers are cut parallel to the edges of the thin film sample. This results in a cross section that is observed along either the [100] or [110] direction in the TEM. Then, using a Gatan epoxy resin, these wafers are fixed together with the thin films facing each other. Several layers of Si wafer cut using the previously described process are fixed using epoxy on either side of the sample wafers to provide bulk for the next step in the process. The epoxy is then cured at 130 °C for an hour in a vice to force out excess epoxy and provide a good contact between the wafers.

Coring and encapsulating

Again using the ultrasonic cutter, a circular attachment with a diameter of 2.3 mm is used to cut a core out of the wafer stack, ensuring the film is located within the centre. The core is covered in the same epoxy as above and placed into a brass tube to provide structural stability and prevent the sample from shattering in the next preparation steps. The epoxy is again cured at 130 °C for an hour ready for the next step.

Cutting and polishing of cross-sections

With the sample encapsulated in the tube, the sample is cut into 700 μm thick discs using a slow cutting diamond saw. A large thickness is initially chosen so grinding and polishing of the sample will remove any potential damage from the cutting process. Using a Gatan 623 disc grinder, the sample is grinded on both sides down so the cross section is $\sim 70\text{-}100$ μm thick. Initially silicon carbide (SiC) paper with a grain size of 15 μm is used, with the last 20 μm finished using SiC with a 5 μm grain size. During this stage, it is important that both sides of the cross section remain parallel, else the quality of the sample may be reduced.

For plan view samples, the sample is initially cut into a 3 mm disc using the ultrasonic cutter. The process is then the same from the polishing step described here onwards, although polishing, dimpling and ion polishing focus only on the substrate side of the sample to achieve electron transparency.

Dimpling

With the cross section now 70-100 μm in thickness, a dimple grinder may be used to thin the middle of the sample but still provide structural stability to stop the sample from breaking. The Gatan 656 dimple grinder involves a spinning wheel and rotating sample stage. With the wheel aligned to the centre of the sample (i.e. the interface of interest), a gently sloping hole is created when the sample is grinded. Ultimately, a ~ 10 μm thickness in the centre is desired, so 35-45 μm must be removed from each side. The first 30-40 μm are polished using a copper grinding wheel combined with a 0.05 μm gamma alumina suspension as a polishing compound. The wheel is changed to one covered with a soft felt and, using the same alumina suspension, the final 5 μm are polished away leaving a 10 μm dimple in the middle of the sample. For samples with a Si substrate, a backlight can reveal the thickness of the sample. The Si becomes optically transparent below 10 μm with

the colour of transmitted light (a reddish-orange tint) changing depending on the thickness of the wafer.

Ion polishing

The final stage of sample preparation involves low energy polishing using a Gatan 691 precision ion polishing system (PIPS). The PIPS uses an Ar^+ source in a range of $\sim 2\text{-}5$ keV, slowly milling away the material with a small incident angle until a hole forms in the middle of the sample. The roughness of the surface is proportional to the energy of the ions, with high energy ions leaving a rough surface but a faster milling rate. As a result, the process typically involves polishing at a high energy (5 keV) initially at a 4° incident angle. Inside the polisher is a light underneath the sample which may be used to gauge the thickness in the middle and to observe the presence of a hole. Once a hole is in the process of forming, the energy of the ions may be reduced to 3 keV to polish the sample gently. At this point, the cross-section is now ready for TEM characterisation. The areas of interest found at the edge of the hole will be $\sim 20\text{-}50$ nm thick, which is excellent for atomic lattice imaging using HRTEM.

3.6.2 Focused Ion Beam

A focused ion beam (FIB) of gallium ions is used to ablate samples and can be used to cut out and thin areas to provide a TEM cross-section¹³⁴. The FIB is coupled with a field emission gun scanning electron microscope (FEGSEM) to allow for sample observation. The FIB uses a gallium source that is heated and placed in contact with a tungsten needle. The gallium wets the needle and causes a huge electric field, ionising the gallium. Gallium is a suitable choice for FIB as it has a low melting point and it can be focused to a very fine size (typically <10 nm in size). The ion beam can be focused onto particular areas and the high energies ($\sim 5\text{-}50$ keV) cause the beam to mill into the chosen sections. As the beam hits the sample, ions and secondary electrons are

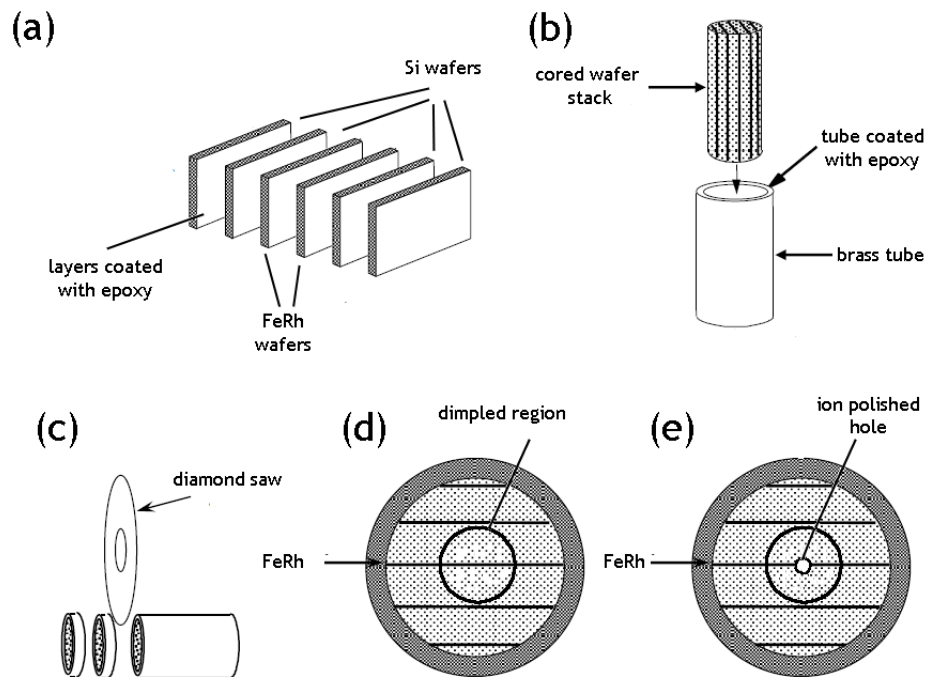


Figure 26: Schematic showing the various stages of cross-sectional TEM sample prep, by a conventional, mostly mechanical method. (a) The sample is cut into wafers and stacked together with silicon wafers cured together with epoxy. (b) A cylinder is cut out of the stack and encapsulated in a brass tube with epoxy. (c) Cross sections are cut from the tube and polished to $\sim 100 \mu\text{m}$. (d) The sample is dimpled until there is a $\sim 10 \mu\text{m}$ thick region in the centre of the sample. (e) The sample is ion polished on both sides until there is a small hole in the middle of the sample. At this point, the region around the edge of the hole is $\sim 20\text{-}50 \text{ nm}$ thick and thin enough for HRTEM imaging¹³³.

sputtered out, which can be collected to form an image. As well as the focused ion beam itself, there is also a gun that ejects a platinum organometallic gas which breaks down when it is hit by an ion or electron beam, depositing Pt. This may be used to deposit onto the sample, typically to mark the area of interest for the automated process and to protect a potentially delicate section

from damage. The sample is moved within the chamber by use of a micromanipulator, which may be used to bring the sample to a grid suitable for mounting in the TEM, where it is welded to the grid by depositing platinum. Finally, the ion beam is used to thin the sample as much as possible, with the final thickness usually resulting in ~ 50 nm, which provides TEM images with a balance between damage and thinness. As with the ion polished samples, the FeRh lamellas were cut along the [100] and [110] directions. FIB sample preparation was performed by Mike Ward in the Leeds electron microscopy and spectroscopy centre.

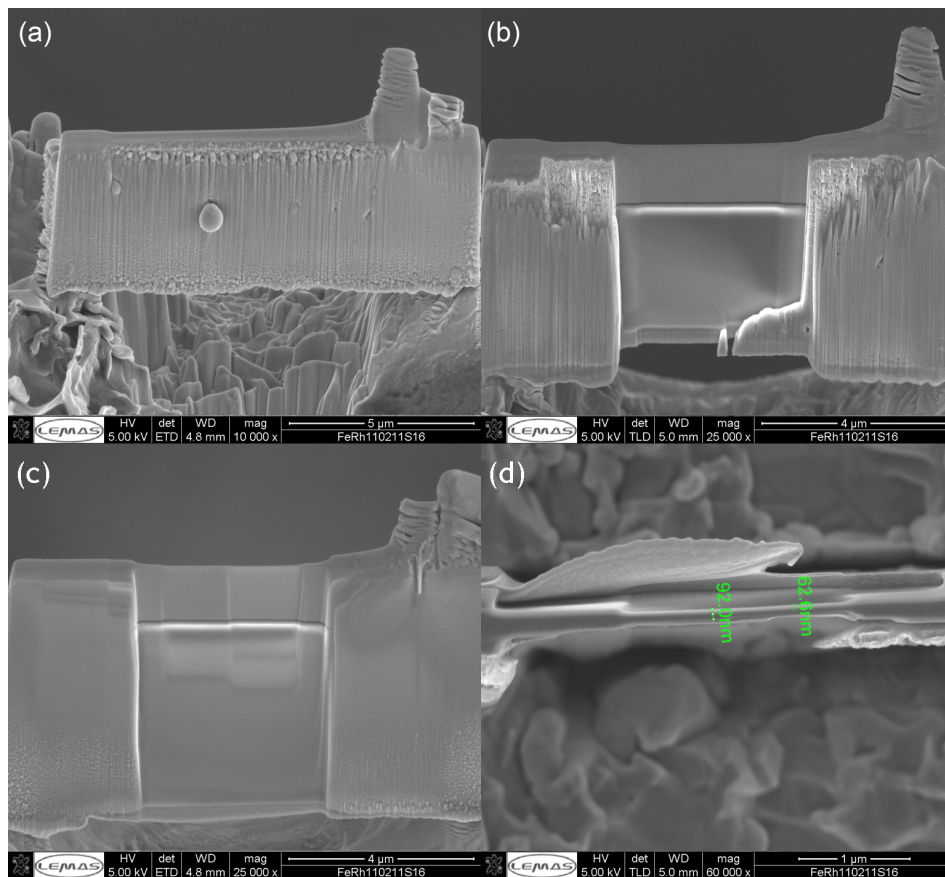


Figure 27: Example of a FIB section cut out of a thin film (a) pre-thinning and (b) after partial thinning. The area around and under the sample has been excavated in image a. (c) The finished FIB lamella. (d) Rough measurements of lamella thickness.

3.6.3 Comparison of Sample Preparation Techniques

Both conventional and FIB preparation techniques have particular advantages and disadvantages. As TEM cross sections prepared by both methods are discussed here, it is prudent to compare and contrast the quality of the samples.

Redeposition

For elemental characterisation, redeposition of material can be a major issue in fully understanding sample composition. Samples prepared by FIB are prone to this problem, as when material is sputtered away it is very likely for it to redeposit nearby. Figure 28 shows an example of MgO redeposition in an iron-rhodium film. In a FIB cross-section there is a small amount of Mg signal found throughout the sample while a conventionally prepared sample shows a large area of redeposition within the epoxy layer. As well, there is potential for Ga ion implantation. In a pre-thinned state, it is highly unlikely for a consistent quantity of diffused material to be found throughout a film. Instead diffusion would be expected to have a gradient away from the interface. For ion polished samples, redeposition of material in the sample is not a major issue. Lower milling angles tend to result in more redeposition. If care is not taken to replace grinding paper or to clean polishing wheels then material from previous sample preparations may collect on the cross section. However, the final ion beam process typically removes this material.

Sample Thickness

The degree of thickness in a cross section is variable across both methods. A conventionally prepared sample should result in a wedge shape, meaning that areas close to the central hole will be extremely thin (~ 20 nm) while moving further away the area of interest will become progressively thicker until the regions are no longer electron transparent. FIB prepared samples tend to have a more uniform

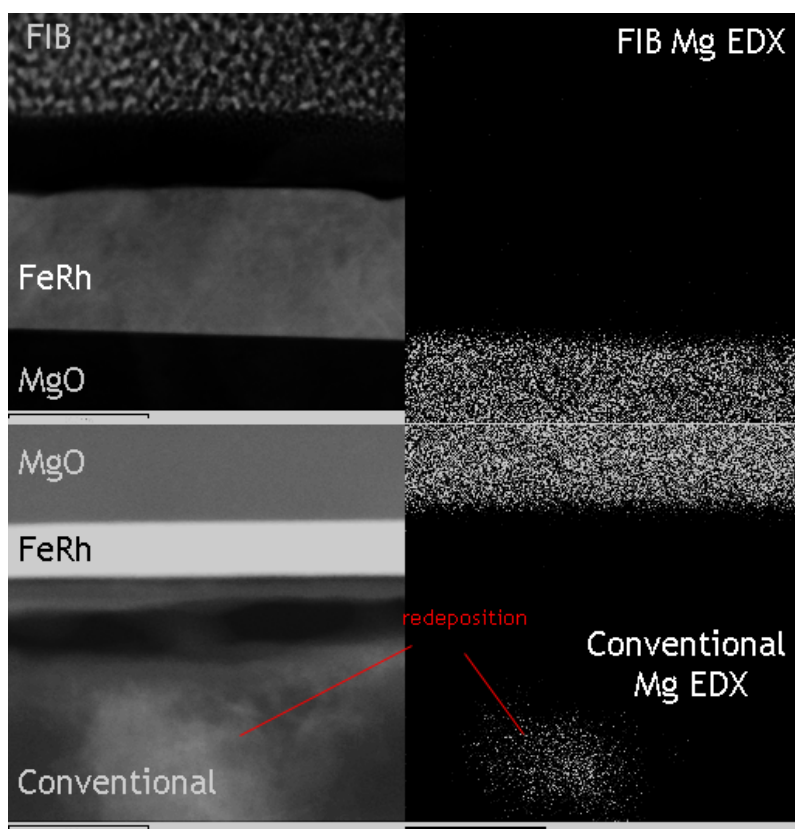


Figure 28: Comparison of MgO redeposition in a FIB prepared and conventionally prepared cross-section. There is a very small amount of Mg signal scattered throughout the image. The conventionally prepared sample shows no Mg signal across the film although there is a large area of redeposition found in the epoxy layer. While uncommon, this is still a potential issue when preparing cross-sections.

thickness as a lamella is instead removed from the thin film. As this lamella is thinned progressively with the ion beam, the process can be stopped when a desired thickness is achieved, although this cannot be measured with a high degree of accuracy. This means that there is no guaranteed extremely thin region as seen for conventional samples but with care large areas of consistently thin material may be visible. Figure 30 demonstrates the area visible to the electron microscope. For the conventionally prepared sample, other areas within the same example exist with comparative

thickness but these regions tend to be $\sim 200\text{-}300$ nm across. The FIB section has a large $\sim 10\mu\text{m}$ wide region for characterisation.

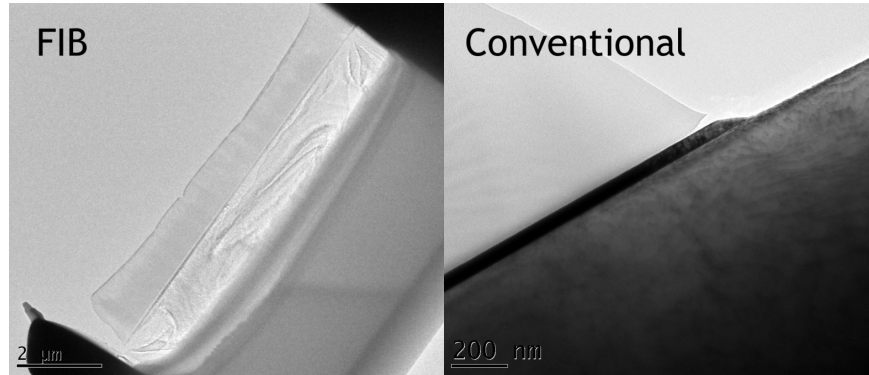


Figure 29: Comparison of electron-transparent regions in a FIB prepared and conventionally prepared cross-section. The entire FIB section is electron transparent while only particular areas of the cross-section provides enough contrast range in conventionally prepared samples.

Structural Damage

It is hoped that a region taken from a thin film, when characterised in an electron microscope, will exist in a similar structural state otherwise the results obtained are worthless. Conventionally prepared samples tend to show less evidence of structural damage, although it can be seen at the thinnest regions that the material becomes partially amorphous, although this is not very visible as the sample becomes thicker. It can be inferred that the ion polishing process creates a thin amorphous layer on the surface of the cross section. In this situation there is enough material that this is not an issue, although the layer may be removed by using a low energy ion beam attachment for the Gatan PIPS. FIB sections also suffer from a similar issue with the existence of amorphous layers on the top and bottom of the layer, which may vary in thickness based on the material of the sample^{135,136}. The only solution to reduce this is using low ion energies and currents that are being

developed in the new generation of low energy Ga ion guns. There is also the possibility of Ga ion implantation. It has also been found that very thin lamellas tend to bend slightly out of plane. Bend contours are visible across the sample and the zone axis of the material can be seen to change depending on location. This effect has been documented on FIB sections taken from strained thin films¹³⁷. It is unknown if this strain relaxation affects the magnetostructural transition, although this is discussed in further detail in chapter 7. Figure 30 shows amorphisation in samples prepared by both preparation methods.

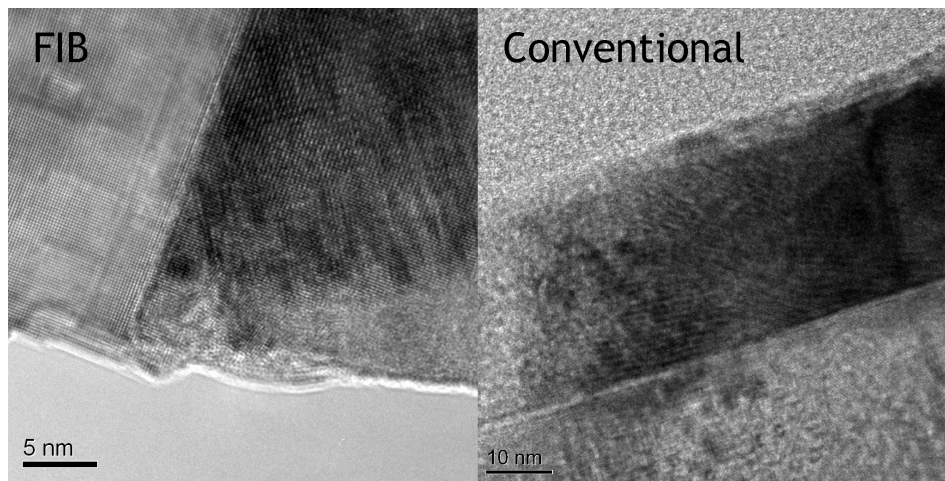


Figure 30: Comparison of amorphisation in FIB and conventionally prepared samples. The amorphous layers are visible at the bottom and left of the FIB and conventional samples respectively.

3.7 Transmission Electron Microscopy

The invention of electron microscopy came about due to the limitations of using light as a way of magnification. The wavelength of the light used to illuminate the sample ultimately determines the maximum resolution available. Using Abbe's equation (equation 13) it can be derived that the resolution limit, d , for a perfect system (i.e. resolving two adjacent sources) for optical microscopy is ~ 200 nm where λ is the wavelength of the illuminating source and NA is the objective numerical aperture ($NA = n \sin \theta$ where n is the refractive index of the medium and θ is the aperture angle)

$$d = \frac{\lambda}{2NA} \quad (13)$$

Therefore, the solution to obtaining higher resolution is to use a beam with a smaller wavelength. It was theorised in 1925 by Louis de Broglie that electrons could have wave-like properties based on their momentum, as described in equation 14, where h is Planck's constant, m_0 is the rest mass of an electron, e is the charge of an electron, c is the speed of light and V is the accelerating voltage of the electron beam.

$$\lambda = \frac{h}{2m_0 e V \left(1 + \frac{eV}{2m_0 c^2}\right)} \quad (14)$$

Using a 200 kV electron beam as an example, this results in an extremely small wavelength (~ 2.5 pm), far lower than the wavelength of visible light (550 nm for green light). Therefore, an electron beam can reach a theoretical resolution limit smaller than atoms themselves. One method of optical microscopy, via a compound microscope, is passing light (transmitting) through the sample. This technique may be copied with electrons using transmission electron microscopy. The first TEM was created in 1931 by Ernst Ruska and Max Knoll, although a microscope with a resolution greater than an optical microscope was developed two years later.

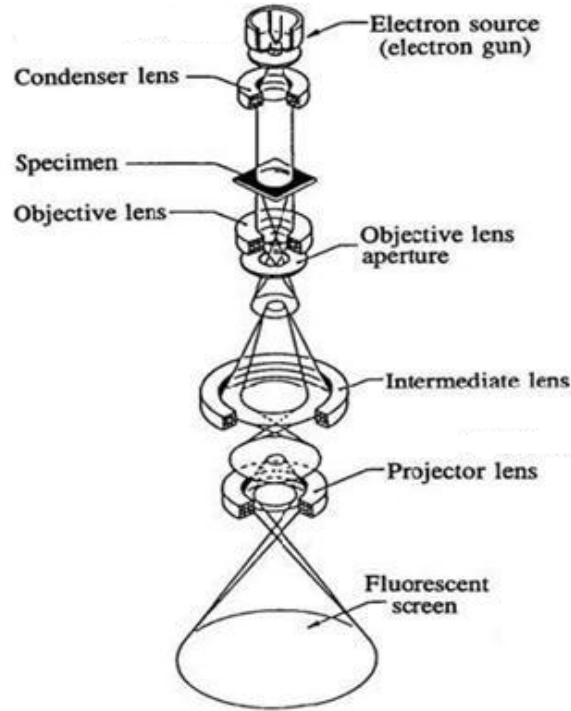


Figure 31: Schematic of a transmission electron microscope and its major components¹³⁸.

3.7.1 Electron Sources

For transmission electron microscopy, electrons may be generated with two main methods, thermionic and field emission guns¹³⁹. Thermionic guns work by heating a source to a high enough temperature. This gives the electrons enough energy to escape the material (the work function Ψ). The physics of thermionic sources can be described by Richardson's Law (see equation 15), which relates the current density of a material to the temperature required to overcome the work function. To obtain a higher current density the sample can be heated. However, increasing the temperature decreases the lifespan of the sample so there must be a compromise. Two materials are used due to their high melting points and relatively small work functions: tungsten and lanthanum hexaboride

(LaB₆). Tungsten filaments are cheap and reliable, but are unsuitable for EELS due to their low energy resolution. LaB₆, on the other hand, gives a brighter image and more coherent electrons, but this requires a better vacuum and the tips are also more expensive.

$$J = AT^2 e^{-\frac{\Phi}{kT}} \quad (15)$$

A field emission gun (FEG) works in a different way, essentially emitting electrons by an applied electric field. The strength of an electric field increases significantly for a needle-like tip as

$$E = \frac{V}{r} \quad (16)$$

These electrons are emitted from the sample via an extraction voltage, and then accelerated to a chosen potential by a second anode. While costing more, a FEG is superior to a thermionic filament as the electrons are more monochromated and the spot size is smaller. The gun needs to be operated under ultra-high vacuum (UHV) conditions ($< 10^{-11} Pa$) to perform effectively. FEGs may be split into cold and Schottky (or warm) FEGs. A cold field emission source uses a single crystal tungsten wire with a sharp end. By comparison, a warm FEG instead is W with a layer of ZrO as a coat which increases conductivity at high temperatures. A current is applied to the Schottky FEG filament to keep the tip at a temperature of ~ 1800 K whereas a cold FEG operates at room temperature. While a cold FEG provides a brighter beam with a smaller energy spread, it has the disadvantage of deforming from ionisation of the residual gases in the column. A cold FEG therefore needs to be flashed, i.e. heated to anneal the tip and remove the defects. Schottky FEGs are immune to this as they operate at a high temperature and defects anneal over time during operation.

3.7.2 The Condenser Lens, Aberration and its Correction

Unlike photons, it is not a viable approach to use a material like glass to focus an electron beam as the electron beam is quickly lost by scattering and absorption inside the crystal. Instead, it is possible to deflect electrons using an electromagnetic field. A typical electromagnetic lens consists of a cylindrical iron pole with a hole in the centre, the bore. A copper coil is wrapped around the pole and when a current is applied a magnetic field is generated. The strength of the magnetic field, and therefore the focal length of the lens, can be increased and decreased by raising and lowering the current. In an ideal lens, a parallel beam should converge at a crossover or focal point. In reality, this is not the case as electrons closer to the optical axis (i.e. further from the electromagnet source) are not focused to the same point as those further from the optical axis. This is known as spherical aberration. Spherical aberration may be quantified by using the collection semiangle of the lens, β , and the spherical aberration coefficient of the lens, C_s . The radius of the spherical aberration disc, also known as a disc of least confusion (r_{sph}) is given by

$$r_{sph} = C_s \beta^3 \quad (17)$$

There is also the possibility for chromatic aberration, where electrons of different energies are brought to focus at different crossover points with lower energy electrons being affected more strongly by the lens. As with spherical aberration, a chromatic disc of confusion, r_{chr} exists with the radius given by

$$r_{chr} = C_c \frac{\Delta E}{E_0} \beta \quad (18)$$

where ΔE is defined as energy loss, E_0 as the incident electron energy, C_c is the chromatic aberration coefficient of the lens¹³⁹. This effect becomes more pronounced for thicker samples, as ΔE increases with increasing thickness.

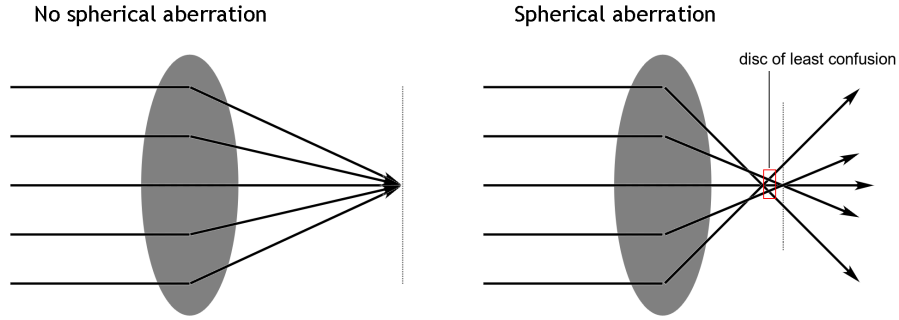


Figure 32: Ray diagrams demonstrating (a) an ideal lens with no aberration (b) a lens with spherical aberration.

After the electrons have been emitted by the gun, they pass through the condenser system containing two lenses, the C1 and C2 lenses. The C1 lens forms a crossover of the gun lens, with the C2 lens controlling the convergence angle of the beam hitting the sample. The C2 lens can be operated to create a parallel beam or a convergent beam depending on the situation required. Finally, the C2 lens has an associated aperture that controls the maximum angle of convergence the beam may have.

In a non-uniform magnetic field, the shape of the beam is distorted as the electrons travel down the column. This phenomenon is called astigmatism and can be described as

$$r_{ast} = \beta \Delta f \quad (19)$$

where Δf is the maximum focus difference induced by the astigmatism. Fortunately, astigmatism may be easily minimised using stigmators. These are small octopoles that create a compensating field to cancel out the imperfections in the lens that causes the astigmatism.

3.7.3 Beam-Sample Interactions

There are many ways in which an electron may interact with a sample. The simplest possible route for an electron passing through an electron-transparent sample is to pass directly through with no interactions whatsoever. However, this is not always the case as the electrons tend to be scattered by the Coulomb forces generated by nuclei and orbiting electrons. These can be scattered elastically (with no energy exchange) or inelastically (where the electron has exchanged energy, typically producing a photon). Both types of scattering can provide useful information about the sample. Electrons can also cause emission of X-rays that may also be detected and give chemical information. Ultimately, these interactions may be broadly categorised as forward and back scattered electrons purely based on the angle of the outgoing ray. Many of the commonly used TEM techniques rely on forward scattered electrons, which includes elastic scattering (i.e. diffraction) and inelastically scattered (high angle annular dark field) electrons.

3.7.4 Electron Diffraction

Electron diffraction is an important technique that comes about as electrons scatter elastically when it enters a periodic atomic structure. As shown before with equation 9, diffraction follows the Bragg equation. In a diffraction pattern, the image obtained is in reciprocal space. This is defined as the space that consists of points corresponding to diffraction from lattice planes. With a parallel electron beam, a diffraction pattern forms in the back focal plane of the objective lens. Depending on the crystal structure, three broad types of diffraction pattern may be generated: a single crystal will produce discrete spots, a polycrystalline structure will give a ring pattern and amorphous materials simply form a diffuse ring pattern. An example of a single crystal diffraction pattern is shown in figure 35. To restrict the pattern obtained to a particular spatial region an aperture may be inserted in the image plane, creating a selected area electron diffraction (SAED) pattern. In a crystal diffraction pattern, the distance between a particular spot hkl and the bright

field (000) spot is related to the lattice constant d_{hkl} . Using the relation

$$\frac{r_{hkl}}{L} = \tan 2\theta \quad (20)$$

where L is the camera length of the TEM, then applying small angle approximations (i.e. $\tan 2\theta = 2\theta$ and $\sin\theta = \theta$) and equating to the Bragg equation (equation 9) we arrive at

$$d_{hkl} = \frac{L}{r_{hkl}} \quad (21)$$

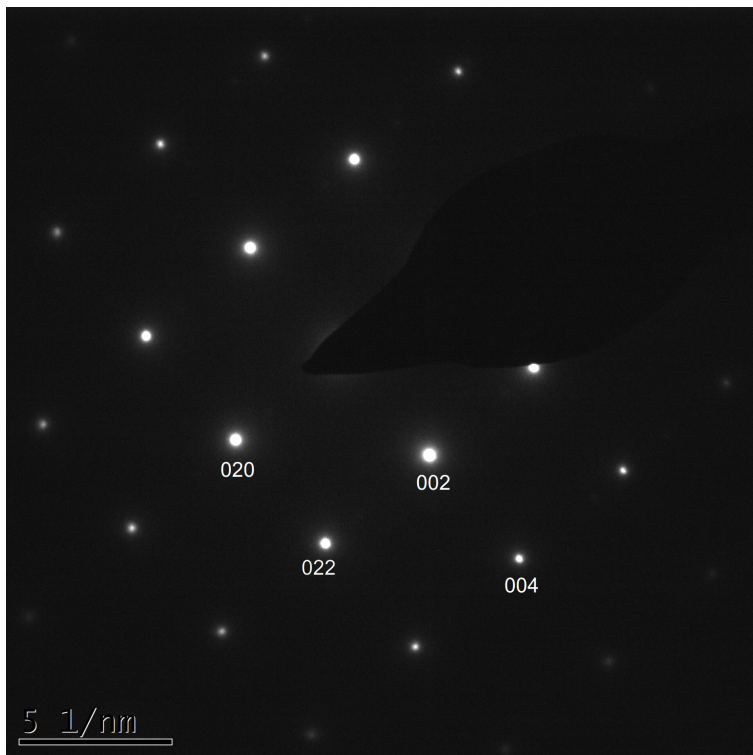


Figure 33: Example of an electron diffraction pattern. Pictured is [001] fcc MgO crystal.

3.7.5 Bright Field and Dark Field Imaging

When observing a sample in a TEM, the variations in transmitted electron intensity provide understanding of structure via contrast, C , which is quite simply defined as a difference in intensity I between two areas

$$C = \frac{I_1 - I_2}{I_2} = \frac{\Delta I}{I_2} \quad (22)$$

Image contrast can occur in two separate ways, via amplitude contrast or phase contrast (with phase contrast being discussed in the next section). Amplitude contrast comes as a result of variations in electron amplitude or intensity, so mass-thickness and diffraction contrast. These types of contrast can be enhanced by selecting particular regions of the electron diffraction pattern, either the bright field (BF) - the unscattered central spot in the diffraction pattern, or dark field (DF) - any region of diffracted beam without the unscattered BF. An aperture may be used to select the imaging conditions of interest, allowing only the electrons desired to form the image.

Imaging Strain

Imaging strain in the microscope is very important for understanding the FeRh system. Bending of atomic planes changes the Bragg condition of the local area, therefore changing the surrounding contrast in bright field images. This contrast change occurs in both the bright and dark field, with a drop in intensity for the bright field image around regions with dislocations, strain or changes to the crystal orientation and an increase in dark field signal collected by the aperture, as demonstrated in figure 34.

3.7.6 High Resolution TEM

High resolution TEM (HRTEM) or phase contrast imaging is important when characterising samples with a periodic lattice. As the electron wave interacts with the sample, its phase may change

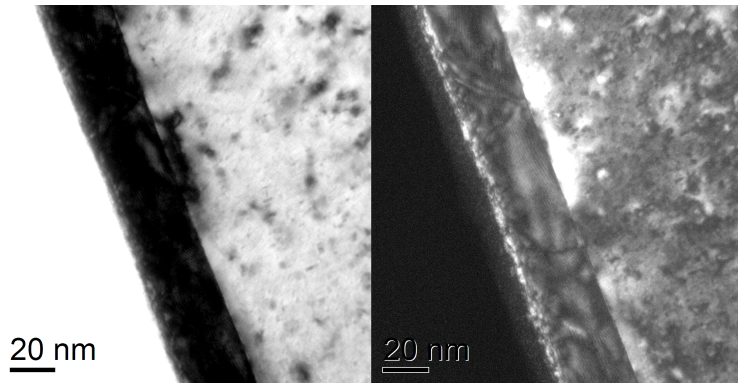


Figure 34: Comparison of a bright field and a dark field TEM image of the (002) MgO spot. The MgO is expected to be single crystal but changes in the Bragg condition (e.g. from strain at the interface) is visible in the bright field as dark contrast and in the dark field image as bright contrast.

relative to the unscattered wave. As a result, the interference of these waves can give rise to contrast in the image with periodicity. These are called lattice fringes and are a representation of the crystal lattice and, as a result, can provide direct measurement of the crystal lattice and the atomic spacings. Despite this, the contrast may not always be directly interpreted as aberration, defocus and astigmatism heavily influence the image formed due to delocalisation of the electron beam.

3.7.7 Scanning TEM and High Angle Annular Dark Field

Scanning TEM (STEM) involves focusing the electron beam into a small, convergent probe that can scan across an area of interest. As a raster scan is used, image acquisition is slower than regular TEM. BF and DF STEM images are acquired using different detectors with a BF detector collecting the electron beam with a semiangle of 10 mrad. A DF detector typically operates with a semiangle of 10-50 mrad with all electrons falling on the detector using to construct an image and is typically referred to as an annular dark field (ADF) detector. At even further semiangles is a high angle

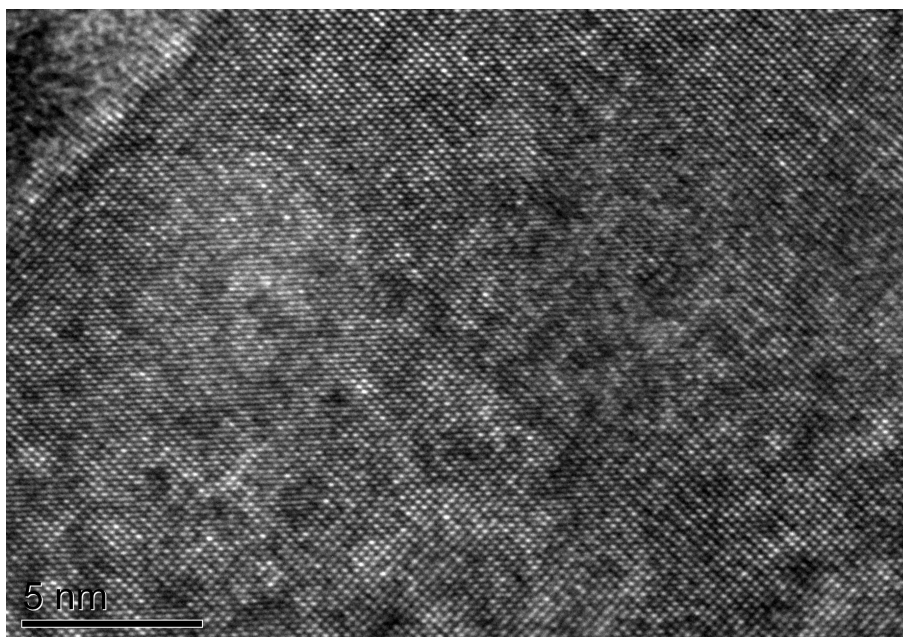


Figure 35: HRTEM image of an MgO single crystal substrate along the $[020]$ zone axis. Here the lattice fringes are visible, allowing direct viewing of the crystal lattice.

annular dark field detector (HAADF), which collects electrons that are inelastically scattered at high angles due to Rutherford scattering. As a result, diffraction contrast is significantly minimised and contrast is almost purely due to variations in mass-thickness and atomic number. It is very common when using STEM to use the bright field signal to collect electron energy loss spectroscopy (EELS) signal to give compositional data in parallel with the HAADF image.

The resolution of the STEM image is restricted by the size of the scanning probe, so aberration is a significant factor in obtaining high resolution STEM data, although this can be minimised using aberration correction. While STEM was initially (and still is) a separate mode within a TEM, dedicated STEM systems with no conventional TEM mode exist.

While HAADF is purely dependent on high angle scattering, annular dark field detectors with a lower semiangle may also be used, in principle to collect similar images. Sometimes called medium

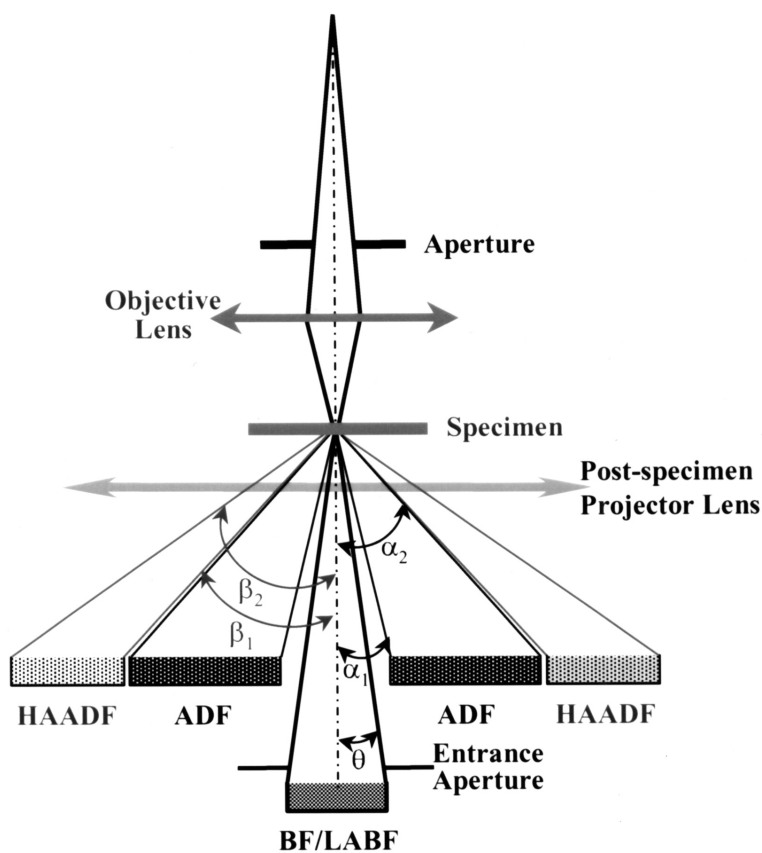


Figure 36: Schematic of scanning transmission electron microscope operating principles¹⁴⁰.

angle annular dark field (MAADF), it also contains information on the strain of a sample region¹⁴¹. If the electron beam channelling conditions are altered, contrast change may appear in HAADF. This is common in situations where the crystal is slightly off-axis or heavily strained¹⁴²⁻¹⁴⁴. Channeling occurs in crystal structures which are oriented along a zone axis parallel to the electron probe. The electron beam then stays close to the atomic column as it transmits through the sample. This maximises the signal and makes the crystal appear brighter than an identical region that is off-axis.

3.7.8 Energy Dispersive X-Ray Spectroscopy

Energy dispersive X-ray spectroscopy (EDX) allows for the elemental analysis of a sample. Electrons in an inner shell of an atom may be excited by the electron beam, resulting in them being ejected and leaving a hole. An electron from a higher-level shell will drop into the empty shell and release a photon of an energy that is equal to the difference in energy of the two shells. The photon is typically of the energy level of an X-ray. The energy and relative intensities of these X-rays can be measured to provide an idea of the elemental composition of a sample. As the number of electron shells increases, more electron transitions can be made. For example, an atom with K, L and M shells can have a K_α (L to K), K_β (M to K) and L_α (M to L) as demonstrated in figure 37. An α X-ray indicates a change between adjacent energy levels while a β X-ray indicates a change between two energy levels.

With EDX spectra, an issue with analysis is that elemental peaks may overlap. However, if an element has multiple peaks then all of them should theoretically be visible in the spectrum.

EDX may be combined with STEM to provide spatial elemental maps. As the probe scans across the sample the X-rays may be acquired. While the signal collected is small, the scans may be repeated in a raster pattern until a complete data set is formed.

3.7.9 STEM-EDX Drift

An issue with STEM-EDX is that the signal obtained from a probe is quite small, requiring multiple passes to achieve data that looks complete. As a result, minor sample drift either from a poor vacuum or interactions between the beam and sample can have a significant effect on the outputted STEM-EDX maps. In particular, there is concern that the FeRh transition itself may cause drift as localised heating of the sample by the electron probe may induce the transition. Figure 38 shows the effect quite clearly, with the maps appearing in a very different location to the initial HAADF-STEM image. The FeRh layer looks smeared in the y axis, with the signal appearing strong in the

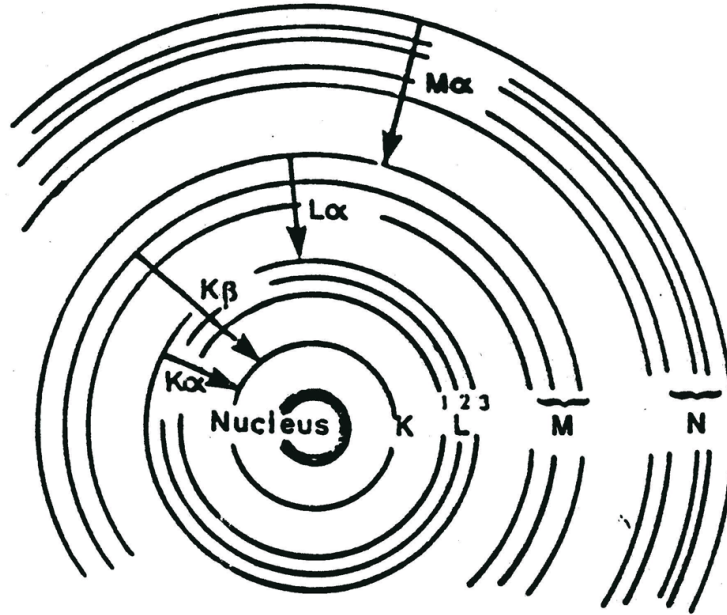


Figure 37: Schematic of demonstrating some available transitions that give rise to X-ray emissions¹⁴⁵.

middle but weaker approaching the edges. The layer also appears thicker than expected.

Another limiting factor for STEM is broadening of the electron beam as it passes through the sample. This means that the expected radius of the electron beam at its focal point as it passes through the sample, and therefore the area of signal collected, is larger than for ideal conditions. The broadening follows the equation

$$b = 7.21 \times 10^5 \left(\sqrt{\frac{\rho}{A}} \right) \left(\frac{Z}{E_0} \right) t^{\frac{3}{2}} \quad (23)$$

where ρ is density, A is atomic weight, Z is atomic number, E_0 is the electron accelerating voltage, and t is the thickness of the sample. Applying this equation to FeRh using an average density of 10.14, atomic number of 35.5, atomic weight of 79.5, an accelerating voltage of 200 kV and a

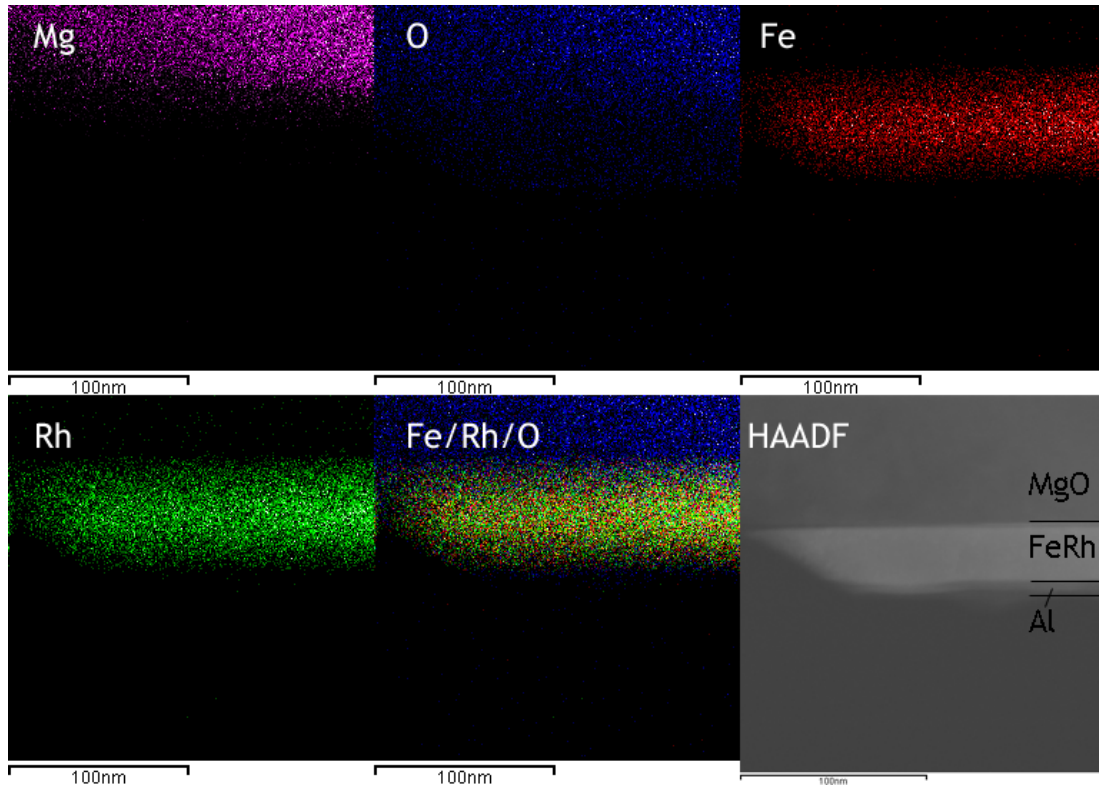


Figure 38: HAADF STEM and STEM-EDX maps demonstrating the effect of drift on results obtained. The position of the initial HAADF-STEM image is very dislocated from the resulting STEM-EDX map with a smearing of the signal in the vertical direction (the signal of the layer is strong in the middle and weak at the edges).

thickness of 50 nm, a broadening of 5.1 nm is obtained. Clearly, this value shows how, for FeRh it is difficult to take EDX maps at face value as the signal is obtained from a large region. It is possible to minimise the broadening with thinner samples. A 20 nm thick sample will result in broadening of 1.29 nm, a significant decrease.

3.7.10 Electron Energy Loss Spectroscopy

Inelastically scattered electrons are interesting as the energy lost is characteristic of the path it has taken. If the initial energy of the electron beam is known, the electron loss (i.e. the measured energy subtracted from the initial energy) can be plotted against its relative frequency as an electron energy loss spectrum (EELS). As an electron passes through a sample, it may lose energy due to a collision with a core electron. As it leaves the sample, it is collected and measured by an electron spectrometer. Due to the quantisation of energy levels in atoms, the energy loss is characteristic to the energy level of a specific electron in a particular atom. This means that EELS can identify the elemental composition of a sample. These tend to occur at energies above 100 eV.

It is possible to use EELS to determine other factors of a sample. Low loss spectroscopy can be used to determine the thickness. Extended energy loss fine structure (EXELFS) can be used to derive the bond lengths in a structure. It is also possible to combine EELS with standard TEM images and select specific electron energies and reform them into an image. The result of this technique effectively allows for the mapping of species in a real space image.

EELS edges are labelled K, L, M, N, O which derives from the electron shell of origin. For example, the K edge corresponds to a 1s electron excitation while an L edge is the result of a 2s or 2p excitation. This is subdivided further so a 2s excitation gives an L₁ edge while a 2p excitation gives an L₂ or L₃ edge. This is shown in figure 39.

In the work shown here, five major core loss edges are collected: Fe L_{2,3}, Rh M_{4,5}, Cr L_{2,3}, W M_{4,5}, O K. The Fe and Cr edges, located at ~700 eV and ~570 eV respectively, exhibit L₂ and L₃ edges, a feature present in many transition metals. The ratio of these two edges can provide information about structure and chemical bonding^{146,147}. The Rh and W M edges, located at ~375 eV and ~1900 eV, are very broad and are not well defined like the Fe and Cr L edges. Finally, the O K edge is located at ~530 eV. Figure 40 provides examples of typical EELS edges for the aforementioned core loss edges¹⁴⁸.

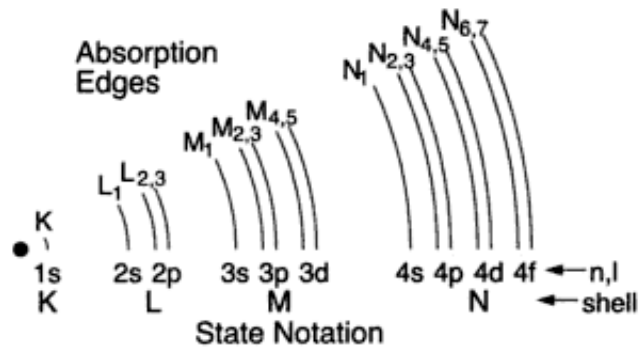


Figure 39: Diagram demonstrating EELS edge with their associated electron excitations.

3.7.11 Lorentz Imaging

All the previously mentioned TEM techniques involve observing structure and chemical composition of a sample. Lorentz imaging is a way of directly observing ferromagnetic signal in a sample. Lorentz TEM relies on the Lorentz force, where an electron beam passing through an area with a component of magnetic induction acting perpendicular to the beam is deflected. In the microscope, this manifests itself as contrast where the domain walls exist but only when the sample is brought out of focus, as shown in figure 41a. The act of imaging this defocused signal is known as Fresnel imaging and is demonstrated in figure 41b. The lines of bright contrast represent the locations of domain walls.

A more advanced mode of imaging known as differential phase contrast (DPC) imaging allows for observation of ferromagnetic domains as opposed to simply domain walls. DPC is performed in STEM mode and relies on the slight deflections of the electron probe as it passes through a magnetic region of interest. This is then observed using a segmented quadrant detector as demonstrated in figure 42a. Images are formed by combining the images of opposite quadrants with intensity based on the difference between the two detectors and these may finally be compiled into a colour vector map that visualises the orientation of the domains as shown in figure 42b.

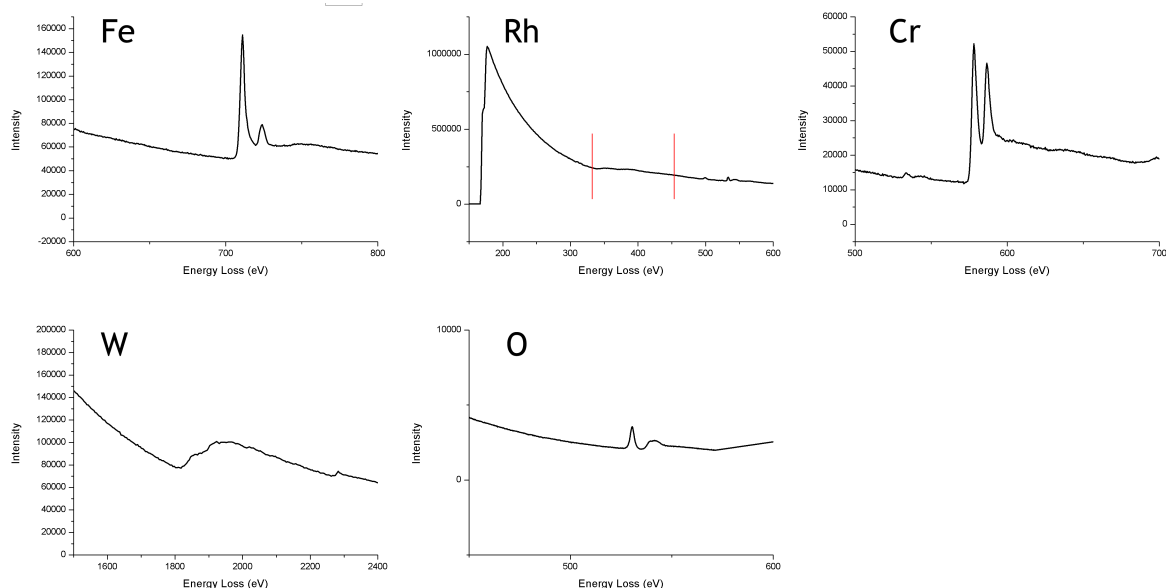


Figure 40: Diagram demonstrating EELS edge with their associated electron excitations. The Rh $M_{4,5}$ edge is highlighted as it is very weak relative to the background and is very close to the carbon K edge and therefore easily missed¹⁴⁸.

3.7.12 Electron Microscopes and Analysis

For the results shown here, four separate microscopes were used. Basic characterisation including bright field TEM, selected area electron diffraction, STEM-EDX and bright field heating experiments were performed using an FEI Tecnai TF20 and Philips CM200 both operating at 200 kV. The Tecnai is fitted with an Oxford Instruments X-Max SDD detector and a Gatan Orius SC600A CCD camera. The CM200 is fitted with a Gatan Imaging Filter (GIF-200). Heating experiments were performed with a Gatan model 628 single tilt heating holder. HAADF-STEM imaging operated with a probe size of ~ 5 nm, as determined via FWHM measurements of a sharp interface (i.e. an FeRh/MgO interface). High-resolution STEM and STEM-EELS were obtained using a Nion UltraSTEM at 100 kV fitted with a Gatan Enfina EELS spectrometer. Principle component analysis to denoise EELS data was performed using the multispectral analysis tool provided by

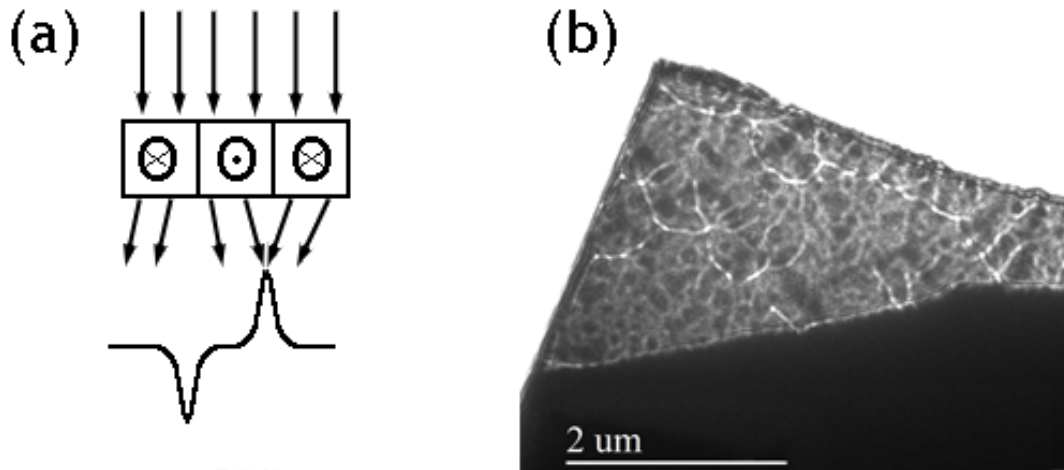


Figure 41: (a) Schematic of how the beam is affected in Fresnel imaging. The beam is deflected when passing through the ferromagnetic domains and bringing the image out of focus shows areas of contrast where domain walls exist. (b) Typical example of a Fresnel image acquired in Lorentz mode. The black and white lines signify the location of domain walls in the film.

HRTEM research¹⁵⁰. The probe size is $< 1\text{\AA}$ and convergence and collection semiangles are 31 mrad and 35 mrad respectively. Lorentz and DPC images as well as microdiffraction patterns were collected on a JEOL ARM 200F microscope at 200 kV with a segmented DPC detector, a Gatan 965 Quantum ER and a Gatan Orius CCD camera. Analysis on all TEM images was performed using Gatan DigitalMicrograph version 1.84.

3.8 X-ray Photoelectron Spectroscopy

X-ray photoelectron spectroscopy (XPS) is a surface-sensitive technique for determining the constituent components of a sample. The basic method involves irradiating a sample with an X-ray beam. These X-rays excite electrons in various energy levels in an atom, causing them to be ejected with a particular kinetic energy (E_{kin}). Due to the quantisation of electronic energy levels, the

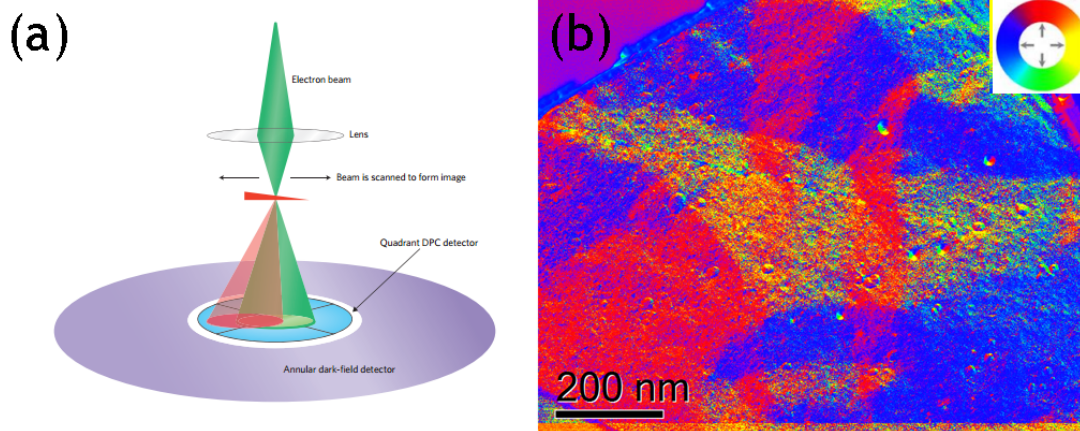


Figure 42: (a) Schematic of a segmented DPC detector and how beam deflection affects the image¹⁴⁹. (b) Typical example of a vector map showing magnetic domains acquired via DPC.

binding energy ($E_{binding}$) for each energy level is unique, giving characteristic peaks for particular atoms. With a given photon energy (i.e. the energy of the incoming X-rays), the E_{kin} can be measured from the ejected electrons and $E_{binding}$ can be calculated using equation 24, where Φ is the work function (energy required to eject an electron from the material). This information, combined with the number of electrons hitting the detector, can ascertain the relative composition of the species in the sample. The chamber must be kept in an ultra-high vacuum ($\sim 10^{-7}$ Pa).

$$E_{binding} = E_{photon} - (E_{kin} + \Phi) \quad (24)$$

The energy levels differ for different compounds, so different oxidation states will result in different peaks. As a consequence, it is possible to ascertain specific compounds (or at least specific species) in a sample. Other forms of electrons may be detected by XPS, in particular Auger electrons. As a core electron is ejected, typically a higher-energy electron will fill the vacancy, releasing energy equivalent to the difference between the energy levels. This is typically released as

a photon, however it is possible for it to excite and eject a secondary electron, or an Auger electron.

To perform XPS experiments, VG Escalab 250 with a monochromated Al $K\alpha$ source was used with an Ar-ion source to etch away sections for depth profiling. The spot size of the source can be focused to a diameter of 120-600 μm .

4 FeRh Structure and Observations of Strain and Dislocation at the Interfaces

4.1 Introduction

FeRh films grown by sputtering are not expected to be perfect crystals when grown. While annealing helps to alleviate this, the imperfections never completely disappear. X-ray diffraction (XRD) measurements on thin film samples provide data to derive a chemical order parameter, S (discussed with XRD in chapter 3), that determines how close to perfect order the sample is¹³⁰. For the samples examined here, the chemical order parameter is typically $S \sim 0.8$, suggesting a small level of disorder in the film, i.e. Fe and Rh atoms swapping positions. The structure of FeRh samples is quite simple, with a typical film grown onto a substrate of MgO and a capping layer on top. Aluminium is the capping material of choice as it prevents FeRh from oxidising, which would cause it to lose its magnetic transition. Some films, which are discussed in more detail in chapter 6, have an epitaxial layer of chromium or tungsten grown on top of FeRh, with a capping layer added above that. These layers are designed to alter the transition temperature by straining the lattice at this interface via compression or tension. In this chapter the bulk film crystal structure for films grown via dc magnetron sputtering is analysed as well as the epitaxy and roughness at the interfaces, using TEM techniques such as selected area electron diffraction, HRTEM and HAADF/MAADF STEM to compare to bulk measurements obtained using XRD and XRR.

4.2 Film Overview, Sample Thickness and Interfacial Roughness

The sample growth method and the conditions for providing the desired iron rhodium film are well documented⁵⁵. The typical thickness for FeRh layers is $\sim 25\text{-}30$ nm and is measured post-growth using low-angle X-ray reflectivity (XRR), along with the roughness at the interfaces. XRR thickness and roughness measurements require simulation to determine the values, whereas TEM

characterisation provides an alternative direct measurement, albeit for a confined area as opposed to an average across the entire film. Figure 43 demonstrates a typical XRR curve for an FeRh film, in particular a film with expected thickness of ~ 30 nm and a W cap of thickness 8 nm. Figure 44 is a bright field TEM image of the same sample. Observing the image initially it may be seen that the contrast between the MgO and FeRh is significant due to the large difference in atomic number (mass-thickness contrast). The film-substrate interface itself is very well defined and appears to be smooth. This is to be expected as commercial single crystal substrates are manufactured with minimal roughness. Some contrast is visible within the FeRh near to the interface which may be due to strain effects. The existence of Moiré fringes within the FeRh film suggest an overlap of crystallites or strain within the film itself. Also shown is the film-cap interface. The cap, here a tungsten layer, has grown epitaxially as can be seen by the lattice matching over the interface. While it is harder to distinguish the layers compared to the FeRh/MgO, the interface is rougher and far more contrast is visible along the boundary, again likely due to strain. From this image, an estimate for thickness and roughness may be determined to compare to XRR data.

Root mean squared (RMS) values for the roughness may be determined experimentally using

$$R_{RMS} = \sqrt{\frac{1}{n} \sum_{i=1}^n y_i^2} \quad (25)$$

where y is distance from the interface and n is the number of data points collected. By defining the interface across an area, variations may be measured on an image to provide a value for roughness. For example, at the MgO/FeRh interface a R_{RMS} value of 0.19 nm was obtained. This is approximately the same value as the spacing between an iron and rhodium atom (~ 0.149 nm) so this interface is very smooth and well-defined. The XRR value obtained for this roughness is 0.176 nm and correlates closely. Table 1 provides a summary of typical thicknesses and roughnesses for a number of layers and their interfaces, as well as comparing to the computed XRR values for the

same sample. All but the Cr and Al layer values are obtained from the sample shown in figure 44 with the comparative XRR data taken from figure 43. The results taken for the Al and Cr interface values are obtained from other FeRh films grown on MgO substrates. Comparing the two data sets the TEM results have shown that XRR data and its computed fit provide a good measure for the roughness.

Interface	RMS Roughness (nm)	TEM Thickness (nm)	XRR Roughness (nm)	XRR Thickness (nm)
MgO/ FeRh	0.19 ± 0.06	27.7 ± 0.8	0.1761 ± 0.0003	28.11 ± 0.06
FeRh/ W	0.27 ± 0.08	8.6 ± 0.3	0.400 ± 0.002	8.82 ± 0.04
FeRh/ Cr	0.31 ± 0.09	8.5 ± 0.3	0.385 ± 0.003	8.47 ± 0.05
FeRh/ Al	0.31 ± 0.09	3.4 ± 0.1	0.357 ± 0.003	2.99 ± 0.04

Table 1: Table of typical thickness and roughness values for various materials and the interfaces they make compared to values determined by X-ray reflectivity. Thickness values are for the bolded material in the interface column. Roughness and thickness values are obtained from the sample shown in figure 44 and the XRR data in figure 43 with the exception of the Cr and Al interfacial data.

4.3 X-ray Diffraction

X-ray diffraction of bulk thin films gives a good starting point for characterising the lattice of FeRh. Figures 45a and 45b shows typical X-ray diffractograms obtained for FeRh grown on an MgO substrate with a Cr and W capping layer respectively. The principle peaks for MgO, FeRh, Cr and W (labelled) correspond with lattice constants of 4.214 \AA (MgO), 3.017 \AA (W-capped FeRh) or 3.023 \AA (Cr-capped FeRh), 2.883 \AA (Cr) and 3.187 \AA (W) respectively. Figure 46 shows patterns from the same two samples across a smaller 2θ range, emphasising the FeRh (002) peaks as well as the (002) W and Cr peaks. The lattice constant difference between the two samples for the FeRh layer is clearly visible as a shift in the (002) FeRh peak due to the strain applied by the capping layers.

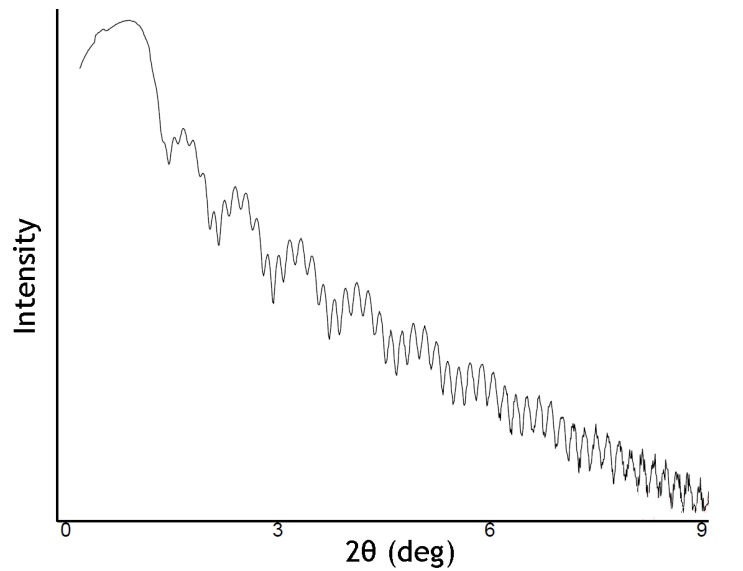


Figure 43: A simulated fit for an X-ray reflectivity curve for an FeRh film with a W cap¹⁵¹.

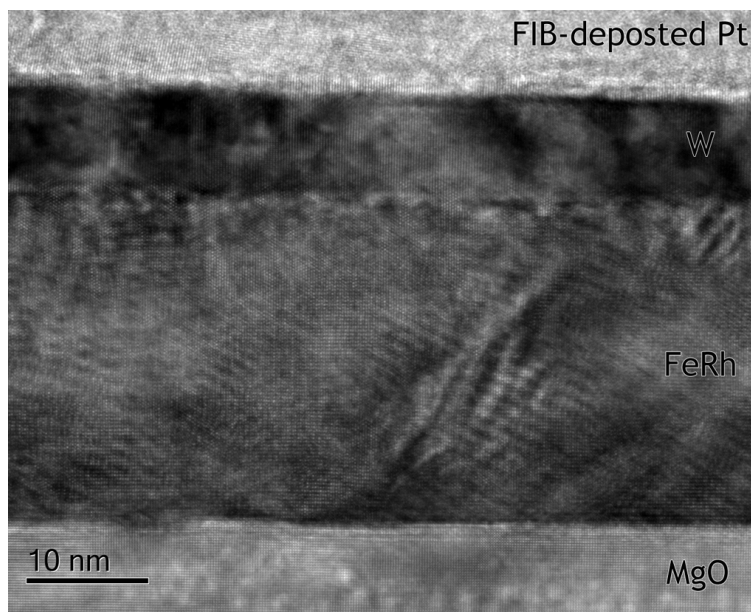


Figure 44: A TEM bright field image showing an example of a typical FeRh film grown on MgO. The large contrast between MgO and FeRh is clearly visible, and the interface between the two appears to be smooth. Epitaxy may be seen across the film-substrate interface as well as the film-cap (W) interface. In comparison, the interface of the cap appears rougher. Contrast is visible along both interfaces likely due to strain. Also, Moiré fringes are visible within the FeRh.

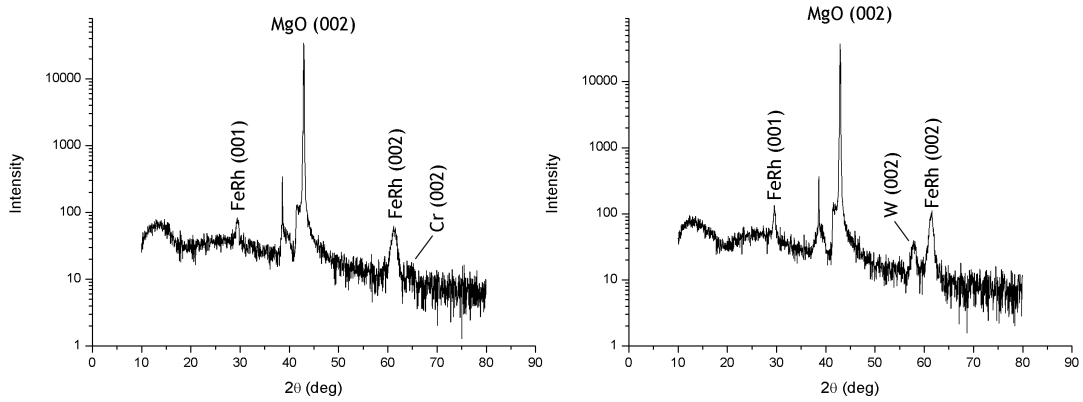


Figure 45: X-ray diffraction pattern of two FeRh films, a Cr-capped sample (a) and a W-capped sample (b). The principle peaks of MgO, FeRh, Cr and W are labelled.

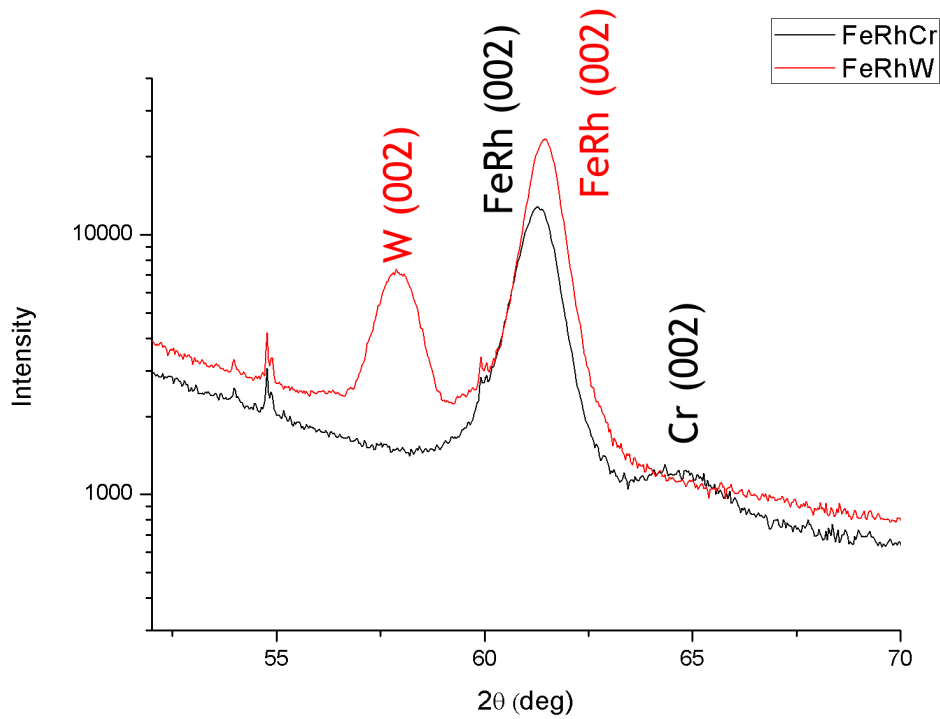


Figure 46: X-ray diffraction pattern of Cr and W-capped FeRh samples with emphasis on the (002) FeRh peaks as well as the (002) Cr and W peaks. The FeRh peak is seen to shift depending on the capping layer applied.

4.4 Electron Diffraction Pattern Analysis

Iron-rhodium is expected to grow epitaxially onto magnesium oxide with an epitaxial relationship of $\text{FeRh}[100](001)\|\text{MgO}[110](001)$. A typical selected area electron diffraction pattern of FeRh/MgO may be seen in figure 47a. The image may be split into two patterns, the brighter square pattern formed by the MgO lattice and the dimmer rectangular lattice from FeRh. Analysis of the pattern is shown in figure 47b. There is an assumed overlap of spots (circled) that fits with the epitaxial relationship of FeRh/MgO shown above. Comparison of the XRD to SAED data may be seen in table 2

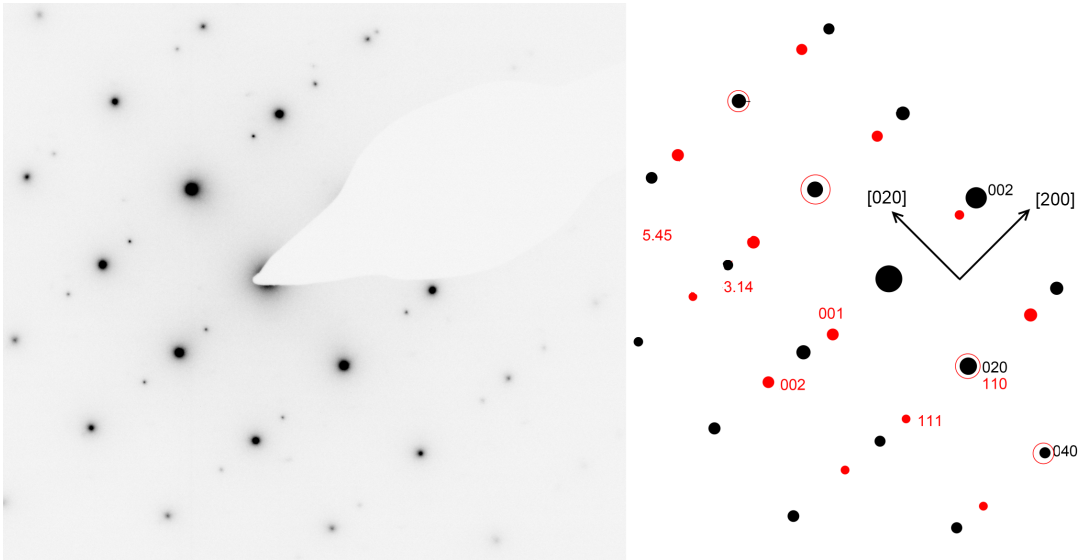


Figure 47: (a) Example of a typical selected area electron diffraction pattern of FeRh grown on an MgO substrate prepared by ion polishing. (b) Measurements and analysis of FeRh/MgO SAED pattern. The black spots correspond with the MgO lattice and the red spots FeRh. The epitaxial relationship ($\text{FeRh}[100](001)\|\text{MgO}[110](001)$) may be seen due to the overlap of the (020) MgO and (110) FeRh spots.

Material	SAED Lattice Parameter (nm)	XRD Lattice Parameter (nm)	Literature Lattice Parameter (nm)
MgO	0.4212	0.421 ± 0.001	0.4212
FeRh	0.30 ± 0.02	0.301 ± 0.001	0.2987 (AFM) / 0.2997 (FM)
W	0.31 ± 0.02	0.319 ± 0.001	0.3160
Cr	0.29 ± 0.02	0.288 ± 0.001	0.2880

Table 2: Table of lattice parameter values as determined from selected area diffraction patterns compared to both measured XRD values and literature values (also derived using XRD)¹⁻³. The values for SAED are calibrated to the lattice parameter of MgO at 4.212 Å.

4.5 Direct Structure Observations

In both the ferromagnetic and antiferromagnetic phase, it is expected that the FeRh films discussed here exhibit a CsCl structure and are epitaxially grown on MgO single crystal substrates with an epitaxial relationship $\text{FeRh}[100](001)\parallel\text{MgO}[110](001)$. This is seen in the diffraction data via both X-ray and electron diffraction. Figure 48 shows a HAADF-STEM image that provides an example of the crystal structure of FeRh directly. Here the alternating layers of Fe and Rh are clearly visible due to the difference in contrast (as a result of the atomic number difference), thereby demonstrating the CsCl structure that is seen in the diffraction data.

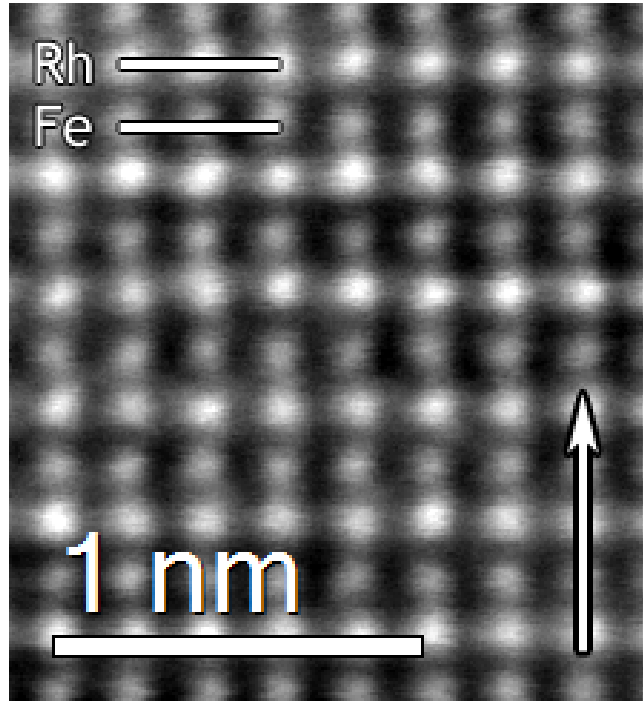


Figure 48: Typical HAADF-STEM image of an FeRh film taken along the $[110]$ FeRh zone axis. The discrete Fe and Rh layers are clearly visible due to the difference in contrast caused by the atomic number difference. This is expected for the CsCl crystal phase that has grown. Direction of epitaxial growth is marked with an arrow.

4.6 Interfacial Strain

As already mentioned, bright field TEM shows areas of dark contrast along the interfaces of FeRh. This contrast is most likely a strain effect. Contrast due to strain is not visible in HAADF imaging unless it affects channeling down the atomic columns but may be seen in MAADF, so comparison between the two, as shown in figures 49, 50 and 51 for the interfaces FeRh makes with MgO, Cr and W respectively allow for observations of strain. The MgO interface shows a ~ 0.5 nm layer of strained FeRh. There is a layer of dark contrast within the Cr layer in the MAADF but this is also seen in the HAADF. In this case, the contrast may be explained by areas of Cr being off-axis relative to the rest of the sample^{143,144}, suggesting there is heavy strain within the Cr layer. There is some bright contrast within the Cr layer at the top and bottom of the image as well as a band of contrast within the FeRh along the bottom half of the interface. This band is ~ 3 nm in thickness. Finally, the W layer shows the most strain, with a continuous band of contrast 3-5 nm in thickness as well as patches of contrast throughout the capping layer.

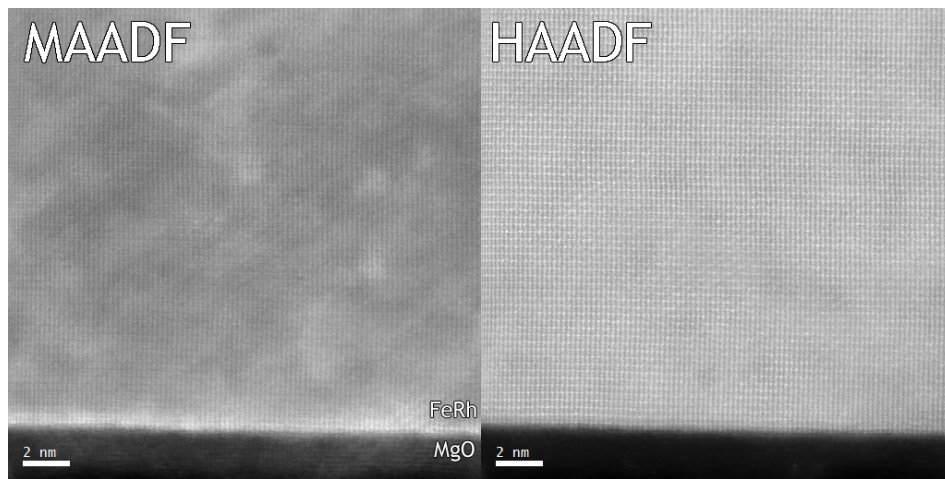


Figure 49: MAADF and HAADF images of an FeRh/MgO interface taken along the [110] zone axis of a FIB-prepared FeRh film. There is a ~ 0.5 nm layer of contrast within the FeRh that suggests interfacial strain.

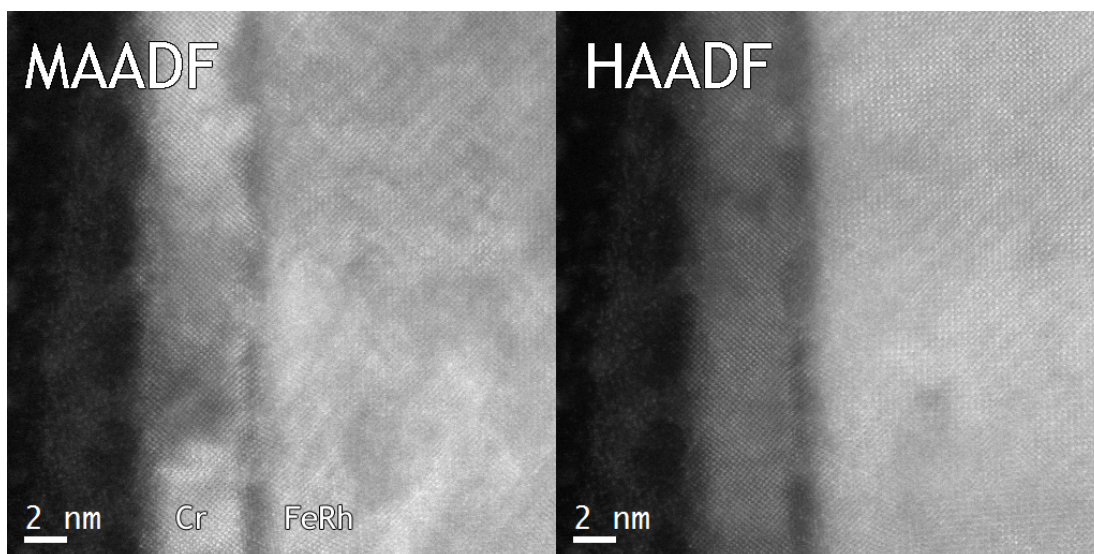


Figure 50: MAADF and HAADF images of an FeRh/Cr interface taken along the [100] zone axis of a FIB-prepared FeRh film. In both images there is dark contrast within the Cr layer which may be attributed to the strain bringing the areas off-axis and disrupting the channelling conditions. There is considerable contrast within the Cr layer as well as a band of contrast ~ 3 nm thick at the bottom of the image, extending somewhat into the FeRh.

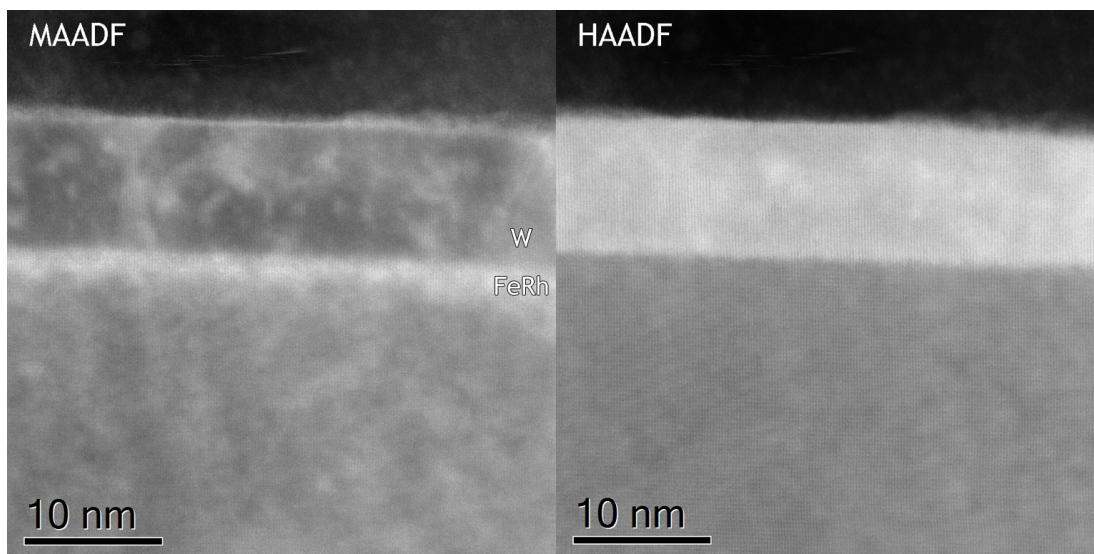


Figure 51: MAADF and HAADF images of an FeRh/W interface taken along the [110] zone axis of a FIB-prepared FeRh film. There is a 3-5 nm layer of contrast within the FeRh as well as contrast in the W layer. The larger lattice mismatch (5.5%) relative to MgO and Cr fits with the larger contrast band seen here.

4.7 FeRh Twins

An interesting contrast feature found within many FeRh films is the presence of bands that run at $\sim 45^\circ$ angles from the interfaces. Figure 52 is a lower magnification image which shows an example of the contrast effect. It can be seen to begin at the interfaces and travel across the sample, sometimes to the other interface. Figure 53 is a phase contrast HRTEM image again showing the this effect. The contrast is reminiscent of laths typically seen in martensitic metals¹⁵²⁻¹⁵⁴ and twin boundaries in crystal structures, for example in gold and silver nanoparticles^{155,156}. As well as these twins, there is also a presence of Moiré fringes throughout the samples. This would suggest an overlap of different crystals, potentially caused by twins in the structure.

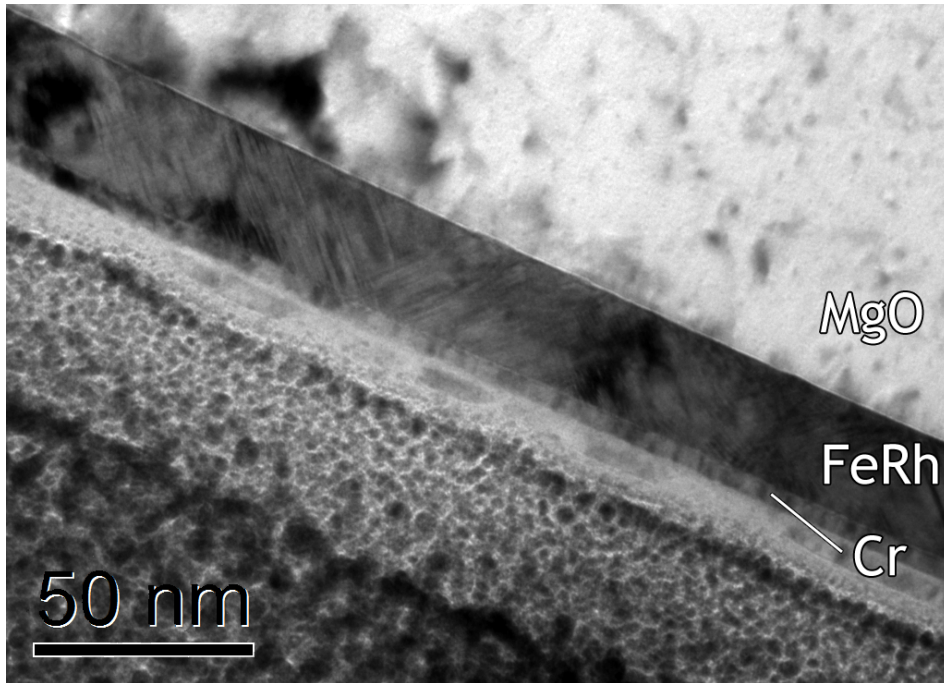


Figure 52: Bright field TEM image showing the diagonal bands of contrast in an FeRh film prepared by FIB. These lines seem to begin at the interfaces and travel through much of the FeRh film, but are not visible elsewhere within the film.

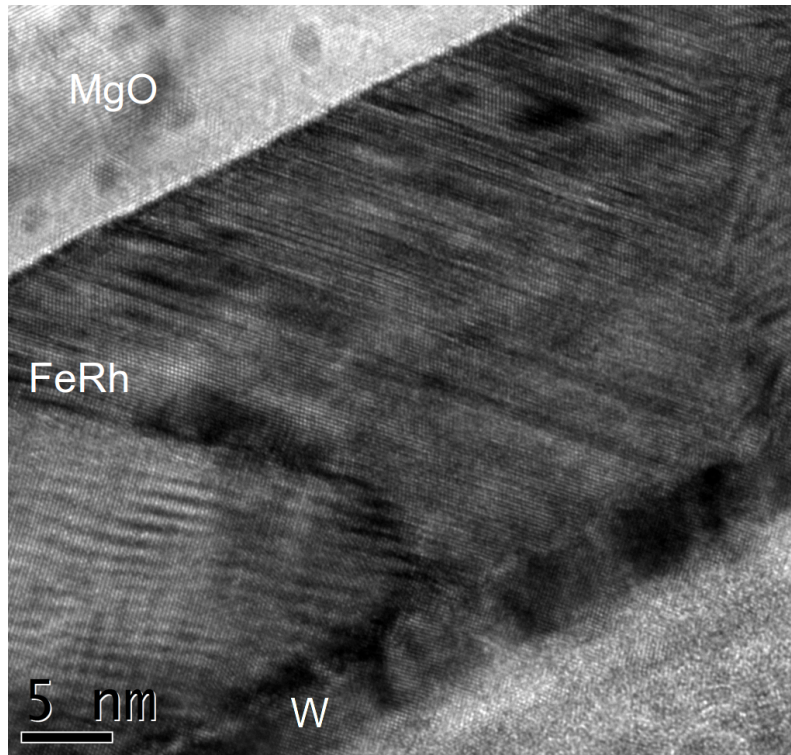


Figure 53: HRTEM image showing the twins in the FeRh thin film in greater detail on a W-capped FeRh film prepared by FIB. Other than the direction and angle, there is no pattern or periodicity in the contrast. Moiré fringes are also visible within the FeRh which is potentially an overlap of twins within the crystal.

A concern when discussing an unexpected crystal structure is whether it is caused by an external effect outside of the fabrication process. Much of the data collected has been obtained using cross-sectional samples prepared by focused ion beam milling so as a result it is a potential worry that using the FIB has caused permanent damage to the lattice to produce the effects seen under the microscope. Microdiffraction of a FIB-prepared cross-section finds the presence of extra ordering spots (figure 55) and is confirmed to be in the FM phase even at room temperature using DPC and Fresnel imaging, where large FM domains are still visible in the film. This is discussed in more detail in chapter 7 when taken into context of the phase transition. Figure 54 shows the existence

of the same twin contrast in a conventionally prepared sample. The effect in non-FIB prepared samples is less common and not as clearly pronounced but still shows that the effect may exist regardless of the sample preparation process. Twins or laths could arise as a result of mechanical deformation (e.g. during conventional sample preparation) but the appearance in both methods suggests that they are not caused by the sample preparation. While both FIB and ion polishing can cause amorphisation on the surfaces of cross-sections, it is unlikely that this is the cause of the reordering. An effect caused by sample preparation would also cause damage to the cap and substrate, both of which appear undamaged apart from some amorphisation. Instead it is more probable that this is a strain-induced reordering that is connected with the phase transition.

The crystal structure is more clearly visible using HAADF-STEM. The contrast from the twins is less visible here and instead the difference in orientation of the crystal is easily seen. Figures 56a and b provides examples of twin boundaries found in HAADF-STEM. The red lines indicate the twin boundaries. Within the lines a different crystal orientation may be seen to the outside of the lines. In figure 56a, the twin angle is measured at 65.1° . The main crystal orientation appears to be $[111]$ while the twin plane is (111) . For figure 56b, the twin angle measured on the HAADF-STEM image is found to be 46.7° . The main crystal orientation of the crystal seen here is $[001]$ while the twin plane is (111) . Comparing to other martensitic structures, a similar example is the shape memory alloy titanium-nickel (TiNi)^{33,34}. The parent phase of TiNi is B2 (i.e. the same as FeRh) and the martensitic phase is a complex superlattice defined as B19'. The phase transformation is confirmed to be first order and the twin plane is found at a 45° angle to the parent, which correlates closely to results obtained for FeRh. Another similar alloy is manganese-gold (MnAu). At high temperatures, MnAu exists in a CsCl superlattice and when cooled below 500 K, exhibits a second order transition to an AFM phase with the lattice changing to bct^{33,157}. For alloys with a composition range of less than 50% atomic Au, a second martensitic transformation occurs when cooled further. During this transition, it is seen that the direction of the Mn magnetic moment changes. Again, parallels to

FeRh are visible here with a changing of magnetic order and an associated structural change.

This effect has not been seen in either X-ray or neutron diffraction with XRD results presented in this thesis and XRD/neutron experiments in the literature showing no evidence of this martensitic transition. XRD measurements of FeRh on MgO substrates at room temperature has shown a small tetragonal distortion (with the lattice volume remaining the same)⁸² that provides evidence for a bct structure but does not explore further the changes in the crystal structure upon heating. If the martensite structure that forms in FeRh is bcc, bct or a similar structure then it is unlikely that the difference between the peaks will be visible in XRD in the high temperature phase and has therefore not been pursued further. It is difficult to confirm the exact cause behind these twins, but the most likely explanation is that FeRh makes a martensitic transformation upon heating to the FM phase. The potential martensite phase could be encouraged by epitaxial strain at the interfaces forcing a slight tetragonal distortion. This transformation could provide some explanation towards the extra ordering spots seen in microdiffraction as well as the twin planes seen in real space. The fact that these are observed at room temperature can be explained for both FIB-prepared samples and conventionally-prepared samples. For FIB sections, the damage to the structure (i.e. some disordering of the ordered B2 phase or amorphisation) lowers the transition temperature, forcing the martensitic phase at room temperature. In conventionally-prepared samples, the effect is not widespread and is instead confined to the interface where a small region of FM phase is located in the AFM phase. The fact that there are very similar parallels in other materials with magnetostructural transitions strongly suggests that a martensitic transformation in FeRh is a likely possibility. However, while there is some evidence that fits with martensitic transformations, the theory is still very incomplete. Most martensite phases appear upon cooling as opposed to heating which does not fit with the diffraction data collected here. It could certainly be argued that if FeRh changes from bcc to bct or another phase upon cooling into the AFM phase it fits the definition of a martensitic transformation. The microdiffraction pattern complicates issues as no other existing

diffraction data seems to correlate on both a localised scale (i.e. TEM) or a bulk scale as seen in XRD with no presence of extra ordering seen in other work.

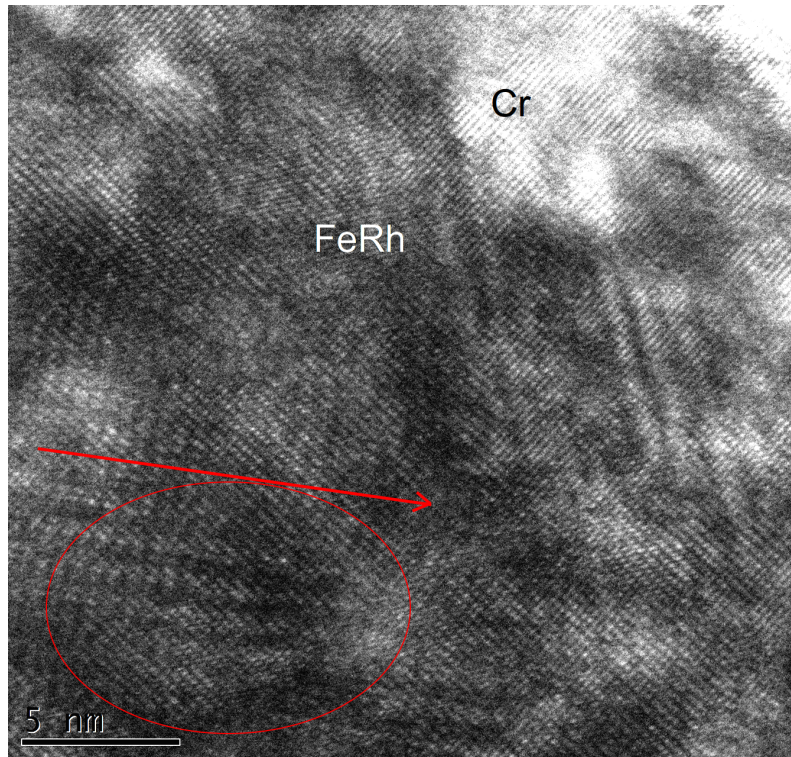


Figure 54: HRTEM image of a conventionally prepared FeRh sample along the [110] axis exhibiting the same lath contrast seen in FIB-prepared cross-sections (circled with direction highlighted). The effect is less widespread and not as obvious but clearly still exists. There is a strong presence of Moiré fringes close to the interface

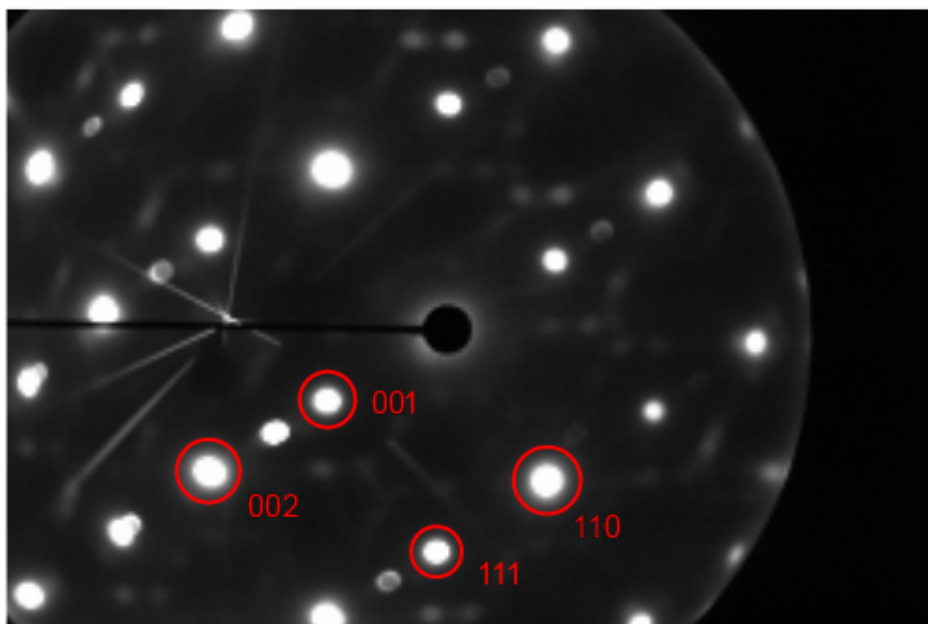


Figure 55: Microdiffraction pattern summed from only the FeRh layer in a FIB-prepared Cr-capped sample. When compared to a standard selected area diffraction pattern of an FeRh film, there are many extra diffraction spots visible. The locations of some standard CsCl FeRh spots are highlighted. It is important to note that, while at room temperature, the heating experiments performed on FIB-prepared cross-sections suggest that this is not in the AFM phase.

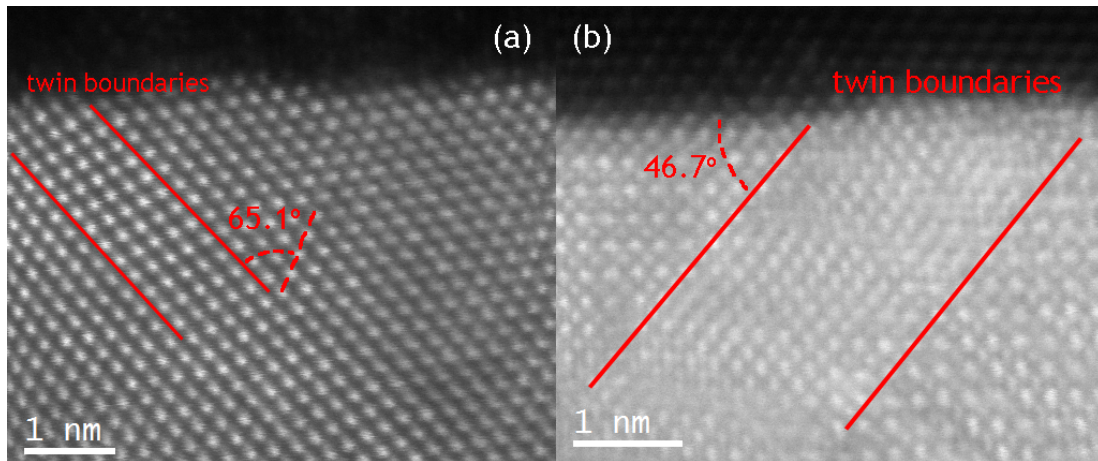


Figure 56: Observations of twins in HAADF-STEM. To the left and right of the red lines (i.e. twin boundaries) exists one crystal orientation whereas in between exists another. (a) The main crystal orientation appears to be $[111]$ showing (111) planes. At the twin boundary (which lies along the (111) plane), the planes make an angle of $\sim 65^\circ$ with the twin plane. (b) The main crystal orientation is $[001]$ and shows (100) planes. At the twin boundary the planes make an angle of 45° with the twin plane. As the twin plane is (111) it is not edge on and the crystal goes out of orientation on the other side of the twin boundary.

4.8 Chapter Summary

Initial characterisation of FeRh films gives an idea of the general structure, including confirmations of film thickness and roughness previously computed by fitting XRR curves. These values fit relatively closely and confirm that dc sputtering is indeed an effective growth method for FeRh. The interfaces are not overly rough and the thicknesses are in line with the planned thickness during growth.

XRD and SAED measurements of the lattice as well as HAADF-STEM imaging confirm the crystal structure of FeRh. The SAED and XRD are in agreement and show very similar results for lattice parameter. The SAED pattern confirms that FeRh is in a bcc structure, while the HAADF-STEM directly shows the alternating rows of Fe and Rh that are expected in a CsCl structure.

As expected, there are many strain effects occurring within the FeRh and its capping layers. The epitaxial growth of FeRh onto MgO combined with the small lattice mismatch has applied a strain within the FeRh layer that manifests into a continuous band of contrast ~ 0.5 nm thick along the interface. Thicker bands of contrast appear at the interfaces FeRh makes with Cr and W, with the capping layers also exhibiting large amounts of strain.

Finally, there is some evidence to show that the FeRh structure is not always completely single crystal. Many samples show twin boundaries within the FeRh, with HAADF-STEM images showing coexistence of different crystal orientations. There is also a presence of Moiré fringes that correlates with this. Although more dominant in FIB-prepared samples, this effect is partially seen in conventionally prepared samples as well. The effects appear very similar to martensitic phase transformations, specifically like TiNi shape memory alloys and MnAu alloys. The most probable cause for these twins is due to FeRh making a martensitic transition from a B2 structure in the AFM phase to a different (as yet undetermined - possibly bct) phase in the FM state. The epitaxial strain of FeRh at the MgO substrate interface in the AFM phase creates a slight tetragonal distortion in the AFM phase that could encourage a bct structure to form⁸². The twin planes lie at a 45° angle to the parent plane, which follows closely to the TiNi and MnAu systems. The possible martensitic

phase exists at room temperature in FIB-prepared samples due to damage caused by the sample preparation process (discussed in chapter 7) while they exist in smaller amounts in conventionally-prepared samples due to the presence of weak FM signal at the FeRh interfaces in the AFM phase. These results are incomplete and there is no explanation as to why this proposed martensitic transformation occurs through heating rather than cooling like most other martensitic transformations. As well, the diffraction data collected does not fit with data found in the literature. It is important to confirm that this effect is independent of the sample preparation and is not merely a by-product of being a thin film cross-section.

5 Local Chemistry of FeRh at the Film/Substrate Interface

5.1 Introduction

The epitaxial relationship between FeRh and its substrate can play a key role in affecting the magnetostructural transition. As seen in previous research⁸², the slight lattice mismatch across the interface is significant enough to raise or lower the transition temperature. However, the effect of interfaces with regard to composition and interdiffusion is less explored. Compositional changes in iron-rhodium are capable of having a significant effect on the temperature of the phase transition with small amounts of change away from an equiatomic composition increasing or decreasing the temperature required to enter the FM phase. As a result, it has typically been important to ensure that the FeRh composition is well-defined on growth using a target with a particular Fe:Rh ratio so the transition temperature is well-defined. It is expected that epitaxial sputter growth followed by a high temperature anneal will result in a uniform sample but in reality, the ratio of iron to rhodium may potentially vary through the samples. Although analysis of polarised neutron reflectometry data discussed by Fan et al²⁵ shows no evidence at the FeRh-MgO interface for a compositional change hypothesis, the simulations of the films may not account for changes over small length-scales. In this chapter the interface between FeRh layers and MgO substrates is investigated using EELS and EDX spectroscopy techniques alongside HAADF-STEM imaging, with SIMS used as a complementary technique.

5.2 STEM-EDX Maps and Line Profiles

Initial STEM-EDX data using a FEI Tecnai TF20 demonstrates that significant interdiffusion at the FeRh/MgO interface is not apparent. Figure 57 shows elemental maps of each major component of FeRh/MgO as well as a composite map of Fe, Rh and O and a HAADF-STEM image of the same area for comparison. According to both the HAADF and EDX maps, the interface appears to be very

sharp with no evidence of interdiffusion on length-scales above the probe size of the electron beam. The probe size may be approximately determined using the full-width half-maximum of the interface between the FeRh and MgO as the interface is sharp. The contrast change across the interface in the HAADF is clear with no gradient. Within the FeRh there is no visible variations in composition with a qualitatively even signal detected throughout. Oxygen signal is detected throughout the film but this is likely due to oxidation of the sample surface as it is evenly distributed across the FeRh. This is typically avoided in a thin film as a capping layer of Al is added, but a cross-section is not protected in the same way.

Examining the sample at a higher magnification yields similar results, as seen in figure 58. Again the interface appears to be sharp and well-defined with oxygen appearing in the FeRh layer due to surface oxidation. Line profiles created from integrated areas on figure 58 can be seen in figure 59. While the signal is noisy and no inferences may be made about qualitative changes in the FeRh, a small Mg signal is detected throughout the FeRh layer. The most likely cause of this detected Mg signal is redeposition of the MgO layer during the FIB sample preparation process.

5.3 STEM-EELS Spectrum Images and Line Profiles

Using a Nion UltraSTEM 100 with C_s corrected STEM, STEM-EELS spectral images and HAADF-STEM images were acquired on various FeRh films. The much higher spatial resolution (with a probe size of $\sim 1 \text{ \AA}$) means that the Fe and Rh atoms are clearly resolved and, as the difference in atomic weight between the two is relatively high (47), there is obvious contrast between Fe and Rh atomic columns. The CsCl structure of FeRh observed along the 110 or 100 directions means that the columns of atoms visible will be homogeneous assuming a perfect crystal. Alternating rows of iron and rhodium should be seen running parallel to any interfaces. An example of a typical HAADF-STEM image is demonstrated in figure 60. The FeRh appears homogeneous and ordered as expected in the middle of the film.

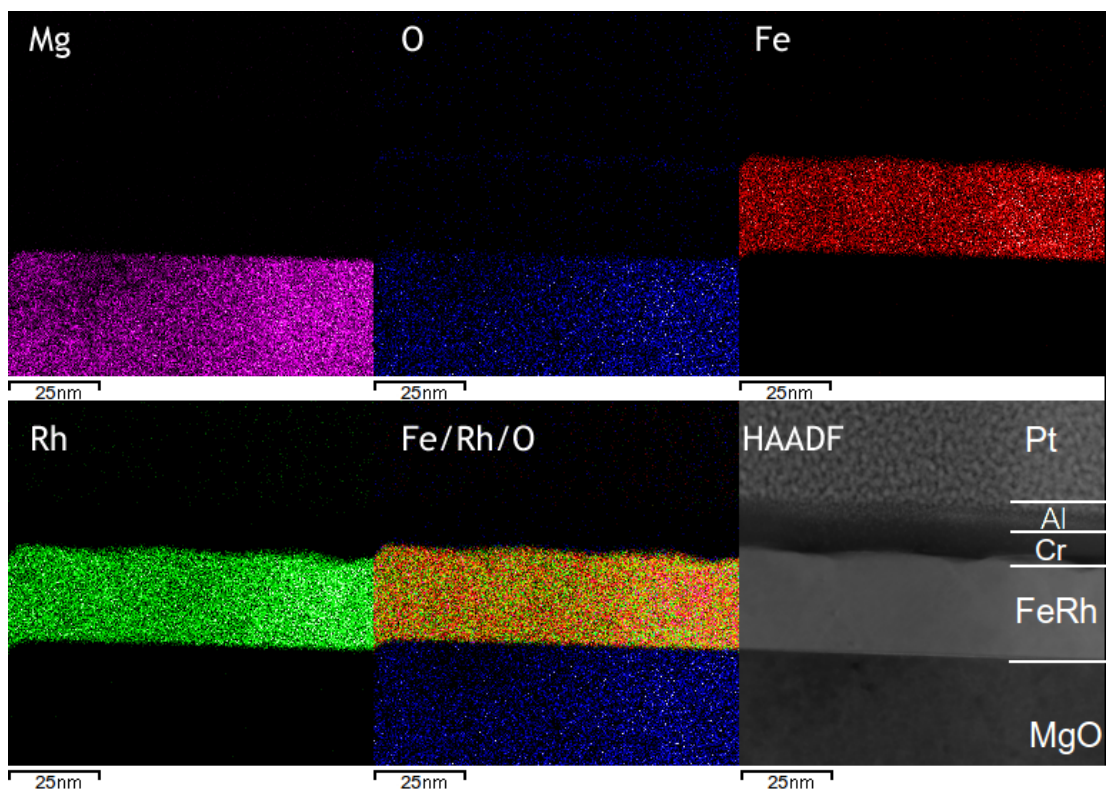


Figure 57: STEM-EDX maps of Mg, O, Fe and Rh with a composite of Fe, Rh and O and a HAADF-STEM image. The positions of the layers correlate well with the HAADF and no obvious interdiffusion around the FeRh/MgO interface is visible. Some O signal is detected outside the substrate however this is most likely due to oxidation of the surface of the sample. No variation or texturing may be seen within the FeRh film both close to and far away from the interface. In the mapped area, more signal is collected on the right hand side of the sample but this is likely due to a thickness gradient in this particular area of the sample.

At the interface (figure 61a), it is possible to see a similar structure, albeit with strain effects affecting the atomic positions. The MgO layer is difficult to see as the atoms do not scatter very strongly and the electron beam quickly sputters material away from the substrate, dropping its signal further. Very few inferences may be made about the chemical composition, although it

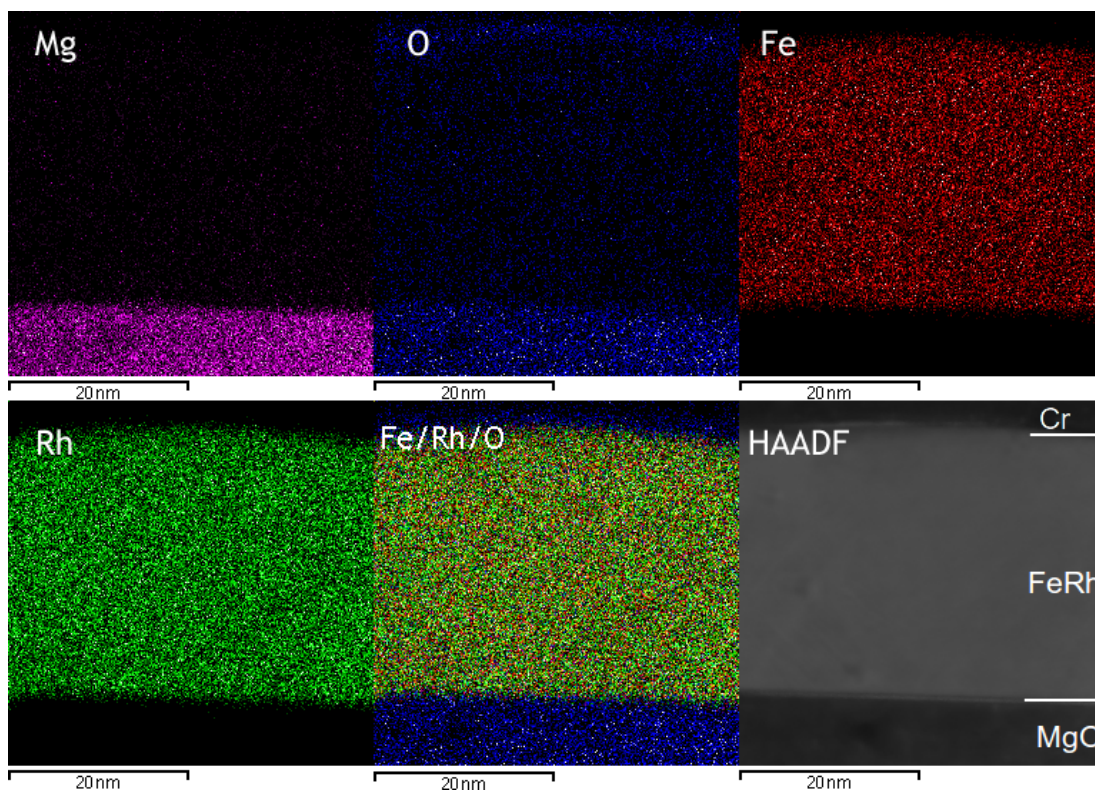


Figure 58: STEM-EDX maps of Mg, O, Fe and Rh with a composite of Fe, Rh and O and a HAADF-STEM image with emphasis on the FeRh-MgO interface. As with figure 57, the interface appears sharp with no obvious traces of interdiffusion. The Fe and Rh signal is consistent throughout the film showing no positional dependence from the interface for the Fe:Rh ratio.

appears as though the film terminates with an Fe layer. Figure 61b shows a line profile taken from the HAADF image at the MgO interface. Peaks and troughs correspond with Rh and Fe respectively with the Fe and Rh atoms alternating as expected through the layer. There are changes in intensity, particularly towards the right hand side (i.e. deeper into the FeRh layer) but this is contrast change due to the twinning effects caused by strain. There are local changes in intensity but this is not enough to confirm or deny any significant changes in composition.

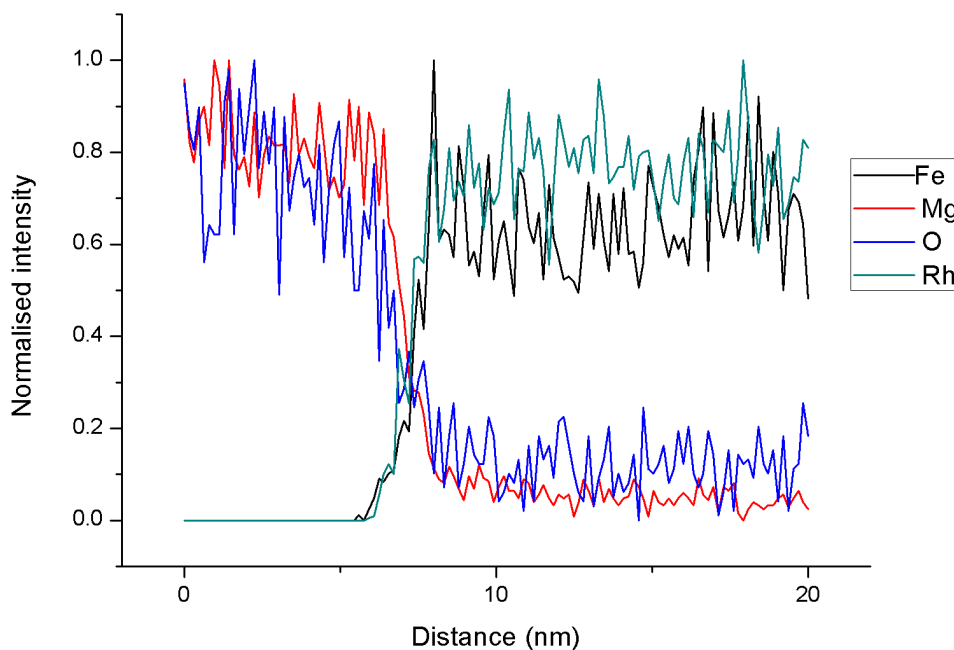


Figure 59: Line profiles showing change of intensity of Mg, O, Fe and Rh across the FeRh/MgO interface. The data is noisy but it can be seen that Fe and Rh have not diffused across the interface. A small amount of Mg signal is detected within the FeRh layer which is unlikely to be interdiffusion due to the sputtering process as this would fall off quickly further into the sample. Instead this is more likely to be a result of the FIB preparation process. While there is Mg signal in the FeRh and vice versa close to the interface, this is due to both beam broadening and the large probe formed in the microscope used. From this interface an approximation of probe size may be determined from the FWHM, showing a probe size of $\sim 2.5 \text{ \AA}$.

When acquiring the EELS data, the principle edges obtained were the iron $L_{2,3}$, rhodium $M_{4,5}$ and oxygen K edges. These all fall within an energy range of $\sim 300\text{-}700 \text{ eV}$, thus allowing for a high energy resolution when collecting data. The magnesium K edge is far from this range ($\sim 1300 \text{ eV}$)

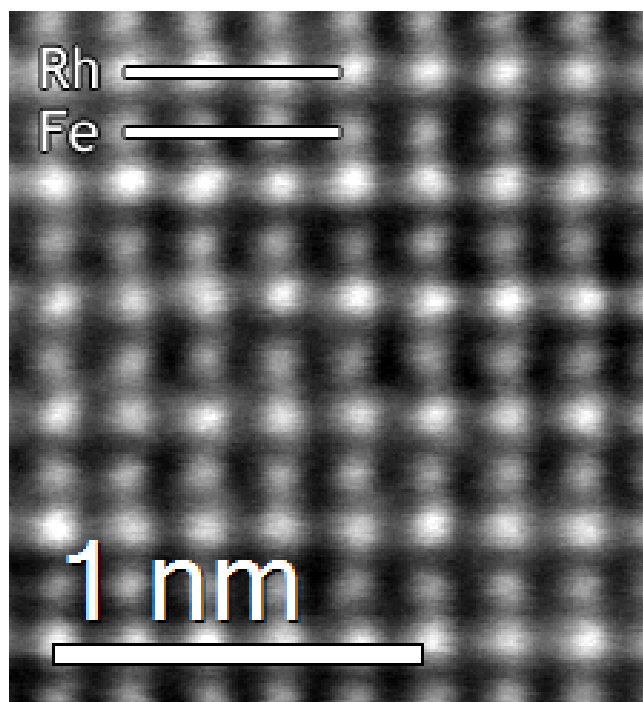


Figure 60: HAADF image demonstrating the spatial resolution obtained using aberration-corrected HAADF-STEM of [110] FeRh. The Fe and Rh columns of atoms can be clearly differentiated with Rh, the heavier atom, scattering more strongly and therefore appearing brighter. The structure appears as expected for a CsCl crystal with alternating rows of Fe and Rh.

so is not collected here. Figure 62 shows EELS spectrum images for the aforementioned elemental edges at an interface with MgO with a HAADF-STEM image of the same area. It can be seen that oxygen signal moving into the FeRh drops significantly, showing no discernible diffusion. A small amount of Fe signal is visible within the MgO substrate. Away from the interface the intensities of Fe and Rh signal alternate with each atomic layer in the same fashion as the HAADF in figure 61 however the intensities of the first three atomic layers show that the region close to the MgO interface is ordered as expected. The first and third atomic layers (Fe) are seen to have an intensity higher than all other Fe layers while the second atomic layer (Rh) has a diminished signal. The

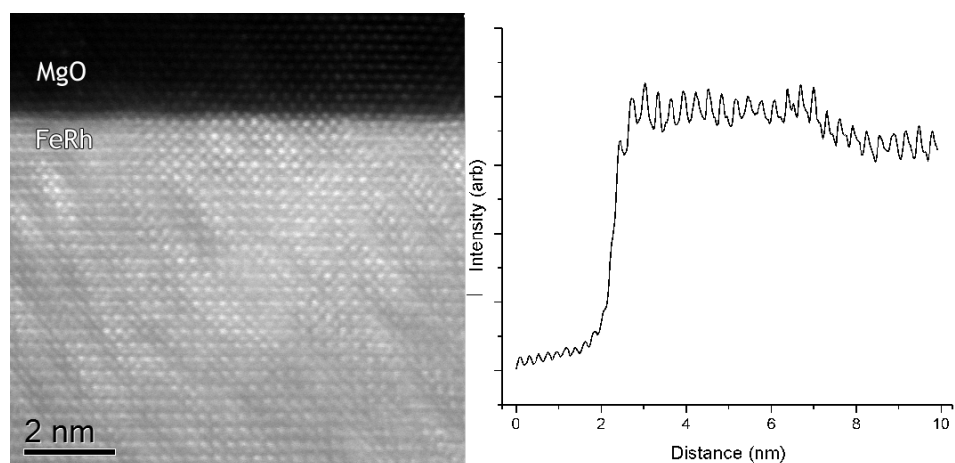


Figure 61: (a) HAADF image taken at the interface of FeRh and MgO along the [100] FeRh zone axis. The MgO appears dark as it is a lighter element that does not produce much inelastic scattering and the electron beam mills the material away as the beam scans over it. However, it may be seen that there are no obvious intensity changes and the Fe and Rh atoms appear to alternate as expected. (b) Line profile taken from the HAADF image showing change in intensities of the atomic columns. Peaks and troughs correspond with Rh and Fe respectively. It can be seen that there is intensity change through the sample although this corresponds with the contrast caused by twinning. There is variation in intensity but not enough to demonstrate a significant change in Fe or Rh composition.

HAADF image does not explicitly show the same phenomenon.

By taking a 20 pixel integrated line profile of the EELS spectrum images obtained in figure 62, the interfacial changes can be seen much more clearly. Figure 63 plots the relative intensities of the profiles with distance, with a comparison to the HAADF of the same area. The change in intensity for the first three layers of FeRh atoms is very clear, with the first two Fe layers appearing stronger and the first Rh layer showing a diminished peak. The HAADF profile shows that the first Rh peak is of lower intensity. It seems unlikely that the Fe signal is higher for the first and third layers due to a higher Fe concentration as they should be entirely consisting of iron. Therefore, the

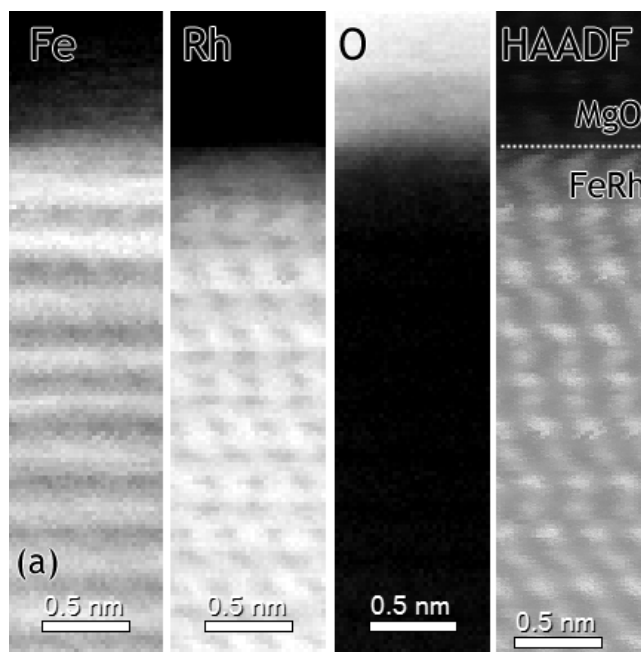


Figure 62: STEM-EELS spectrum images acquired at the FeRh-MgO interface along the [100] zone axis, with maps for iron $L_{2,3}$, rhodium $M_{4,5}$ and oxygen K edges. A HAADF image of the same region is provided for comparison, with a dotted line indicating the FeRh-MgO interface. There is a variation in intensity for the first two Fe rows, which appear brighter than the other Fe layers. Distortion in the HAADF image appears due to beam-sample interactions, particularly due to the magnetic nature of the sample.

most reasonable explanation is that there is a strong Fe signal in the first nominally Rh layer that makes the intensity of the surrounding layers more intense. This also counts for the decreased Rh signal in both the HAADF and EELS spectrum images. As a result, it can now be said that an iron-rich region three atomic layers thick exists at the FeRh-MgO interface. It has been previously shown that Fe monolayers grown onto MgO can exhibit ferromagnetic properties¹⁵⁸, so it is entirely plausible that this Fe-rich region is capable of driving the magnetic transition and explaining the existence of room temperature FM domains in the AFM phase. However, the small compositional variations expected (e.g. $Fe_{48}Rh_{52}$) were not immediately detectable with the equipment used.

Also, the thickness value for the Fe trilayer is an order of magnitude away from the thickness of the latent FM phase (~ 8 nm)²⁵. Another potential explanation for this compositional change could be a strain-induced reordering of the FeRh during sample growth and annealing. The Fe lattice parameter is smaller (2.87 Å) than FeRh (2.987 Å) and while the epitaxially matching MgO lattice ($\frac{4.212}{\sqrt{2}} = 2.987$ Å) is very similar to FeRh a small change in composition may be energetically favourable and the annealing process may allow this diffusion to occur.

5.4 EELS Edge Analysis

Transition metal oxide bonds result in a change in the EELS fine structure of the oxygen K edge¹⁵⁹ with the formation of a pre-peak. As both Fe and Rh are transition metals, this pre-peak is expected across the FeRh-MgO interface. Figure 64 shows the change in the O-K edge across the FeRh-MgO interface. The pre-peak begins to form close to the FeRh layer before promptly disappearing with the rest of the edge. As would be expected, a transition metal oxide is forming at this interface. Based on previous data showing the formation of an Fe-rich layer at the interface, it is clear that an iron oxide is forming at this interface. Comparing free energies of formation of iron¹⁶⁰ and rhodium¹⁶¹ oxides, it can be seen that iron oxides will form more readily due to their lower free energies of formation relative to the higher formation energies of rhodium oxides.

The fine structure of the iron L edge also shows evidence of change through the interface, as seen in figure 65. A small shoulder is visible on the right of the first edge at the interface which quickly disappears further into the FeRh layer. The position of an extra peak close to the L_3 edge can indicate the type of iron oxide bond with Fe^{3+} showing a shoulder before the edge whereas Fe^{2+} oxides tend to have a broader tail or a shoulder on the right hand side of the L_3 edge¹⁵⁹. Therefore, the shape of the Fe EELS edge here suggests that an Fe^{2+} oxide bond has formed at the FeRh/MgO interface.

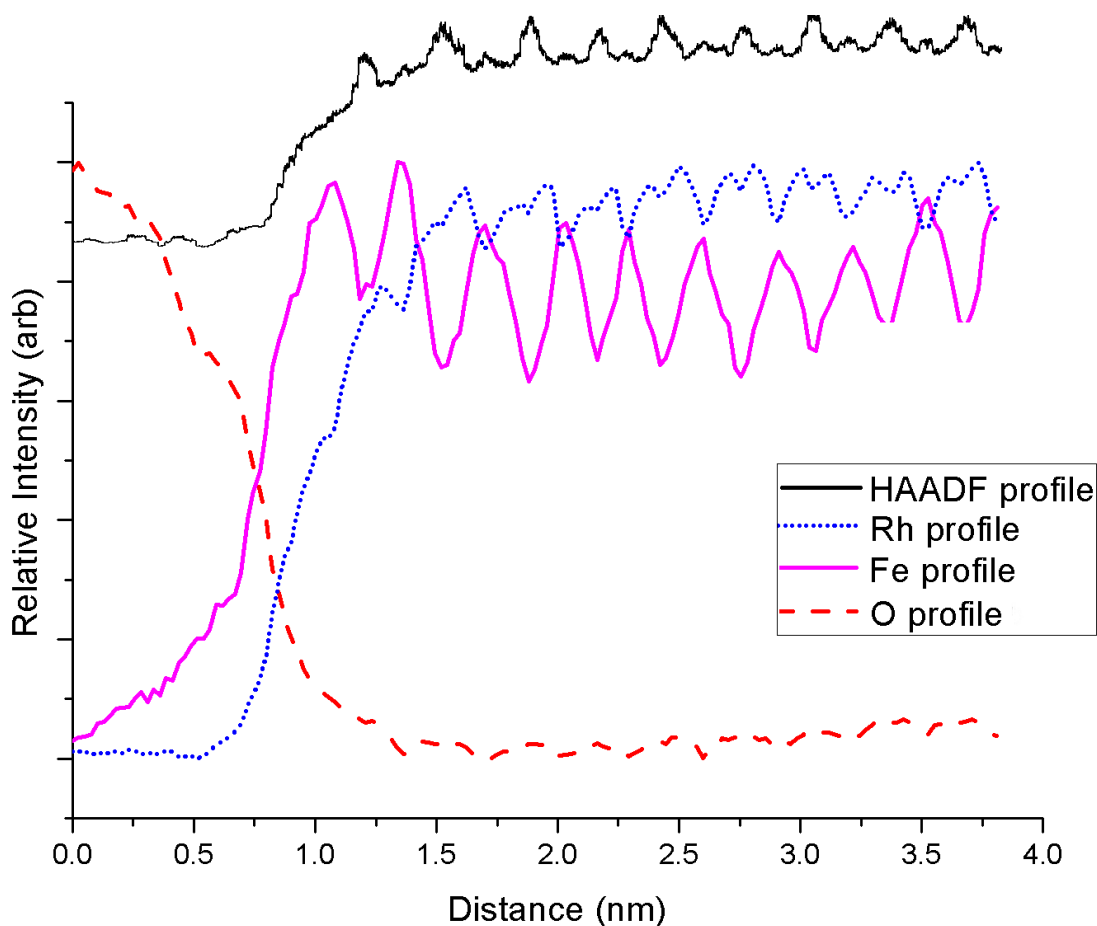


Figure 63: Line profiles taken from the above EELS spectrum images, showing the relative change of Fe, Rh and O across the FeRh-MgO interface. The first two rows of Fe atoms have a noticeably stronger signal relative to the rest of the atoms and the first Rh layer (in between the two Fe rows) is diminished in comparison to the remaining layers. The HAADF profile for the same area is offset above. The intensity change at the interface cannot be seen on the HAADF. Probe size is expected to have a diameter of ~ 1 Å.

5.5 Rhodium EELS Delocalisation

An interesting phenomenon that is visible in the rhodium line profiles is a "volcanic" effect, where the intensity of the Rh atoms decreased in the centre of the atomic column. This effect, known

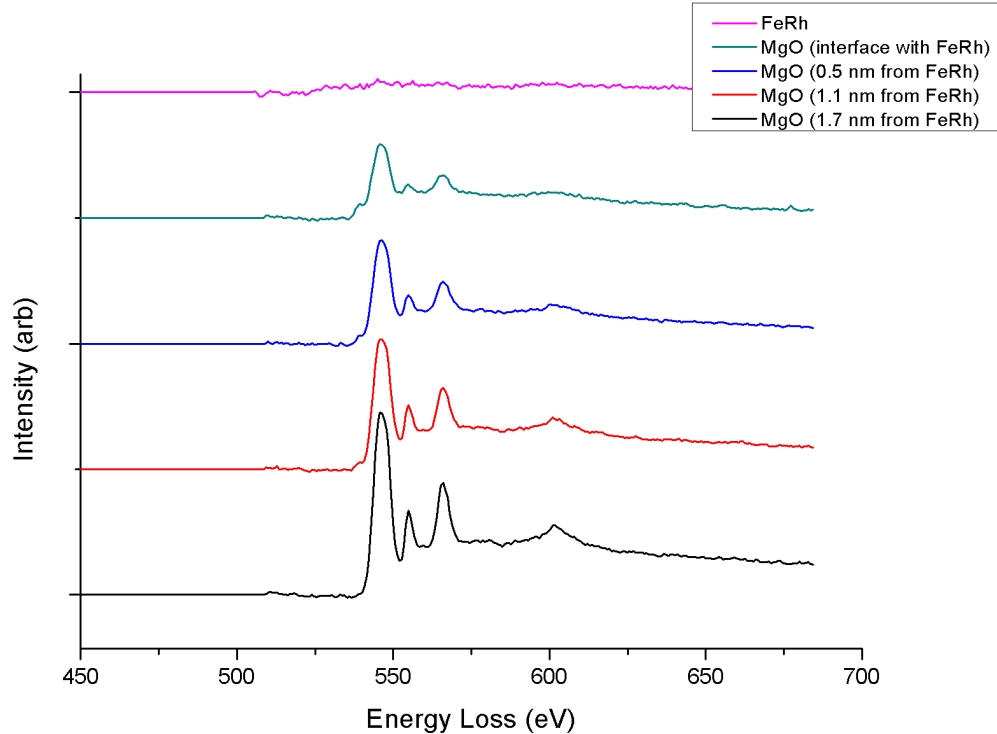


Figure 64: Background-subtracted EELS spectra showing change in the O-K edge across the FeRh-MgO interface, beginning with FeRh at the top and MgO at the bottom. As the probe location passes close to the film, a pre-peak begins to appear before promptly disappearing along with the rest of the edge within the FeRh. This pre-peak is indicative of a transition metal oxide bond¹⁵⁹ and, combined with the EELS spectrum images showing a terminating Fe layer, confirms the formation of an iron oxide at the interface.

as EELS delocalisation, has been previously documented for other materials¹⁶² and is a result of a combination of both elastic and inelastic scattering, i.e. an electron is first scattered inelastically then scattered elastically. The signal collected is then significantly affected by the EELS collection angle used particularly if the scattering column is particularly heavy. Simulations of this effect fit well with experimental data¹⁶³. The effect of delocalisation is a potential concern for high spatial resolution STEM as resolving individual columns of atoms, even with aberration correction, can be

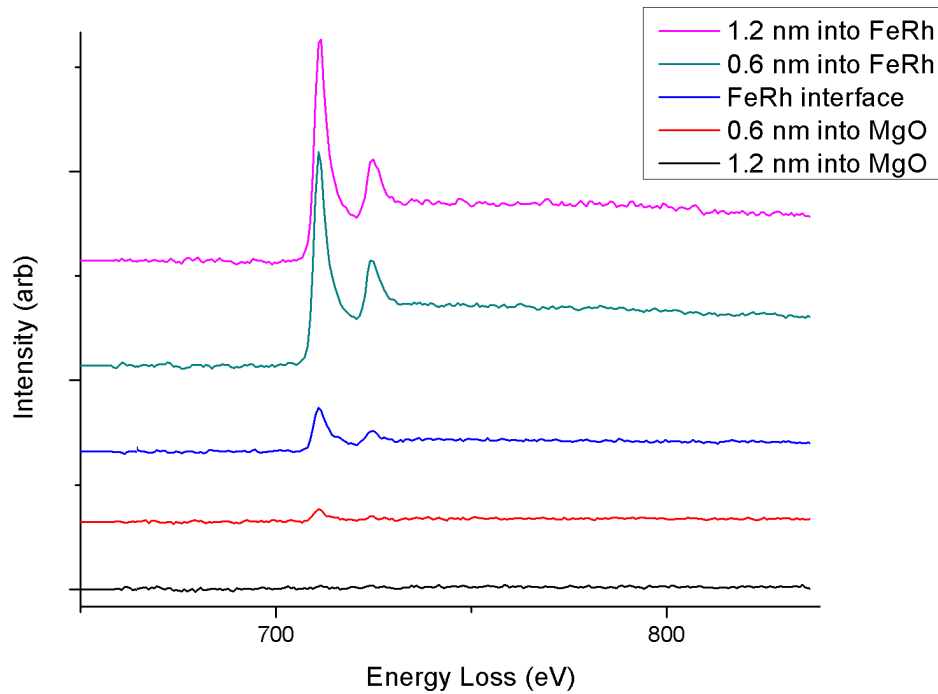


Figure 65: Background-subtracted EELS spectra showing change in the Fe- $L_{2,3}$ edges across the FeRh-MgO interface, beginning within the FeRh at the top and ending within the MgO at the bottom. A small shoulder is visible at the FeRh/MgO interface to the right hand side of the L_3 edge, which is indicative of an Fe^{2+} oxide bond¹⁵⁹. This promptly disappears in both directions away from the interface.

made more difficult¹⁶⁴. The fact this is only visible for Rh is interesting and expected as the M4,5 edges tend to be more delocalised¹⁶⁵. Typically, this may be resolved by using a larger collection angle (here a 31 mrad convergence and 35 mrad collection semiangles were used)¹⁶⁶.

5.6 Chapter Summary

It has been demonstrated that composition changes are prevalent at the FeRh/MgO interface. Looking at the film as a whole it can be seen that the FeRh is qualitatively homogeneous with no clear variations over larger length-scales or pockets of Fe or Rh rich regions. Interdiffusion across the interface may have occurred in very small amounts with some Mg signal detected within the FeRh layer and some Fe within the MgO, although this is likely to be an effect of redeposition during the FIB sample preparation process. O signal is much stronger, but this is certainly due to some surface oxidation of the FeRh in its cross-sectional state.

Most importantly, it has been found that the chemical composition at the first three layers of the FeRh is different from the bulk of the film. The film-substrate interface has a terminating Fe layer, with the second layer consisting of a very strong Fe signal as opposed alternating layers of Fe and Rh. As a result, it can be seen that an Fe-rich trilayer exists at the FeRh-MgO interface that could play an important role in the magnetic properties at the interface. A magnetised Fe layer could provide an explanation for small FM signal detected at the FeRh-MgO interface in the room temperature AFM phase and, combined with strain effects from the MgO lattice, provide a nucleation point to drive the sample into the FM phase. Research of ultrathin Fe layers grown on MgO substrates show the presence of a magnetic moment similar to bulk Fe¹⁵⁸ so this trilayer is likely to exhibit a FM signal but is unlikely to explain the FM signal alone due to the differences between the thickness value measured here (0.5 nm) and the literature values for the latent FM phase (~ 8 nm)²⁵. The reason for this chemical change could be a strain-induced composition change during sample growth and annealing. Fe has a smaller lattice parameter (2.87 Å) than FeRh (2.987 Å) and while the matching epitaxial MgO lattice along the [110] ($\frac{4.212}{\sqrt{2}} = 2.987$ Å) is very similar to FeRh a small change in composition may be energetically favourable and the annealing process may allow this diffusion to occur.

6 Local Chemistry of FeRh at the Film/Cap Interface

6.1 Introduction

The effect of interfacial epitaxy with a lattice mismatch on the phase transition of iron-rhodium is well documented using magnesium oxide substrates to apply a strain on the FeRh film²⁵. Therefore, it is reasonable to assume that an epitaxially grown capping layer could have a similar effect. Tungsten (W) and chromium (Cr) are both transition metals with a body-centred cubic structure and have lattice parameters of 3.16 Å and 2.88 Å respectively compared to the value of 2.987 Å of FeRh¹⁻³. These match relatively closely to the 2.987 Å of bcc FeRh. It can be assumed that W will place a tensile strain on the FeRh film (reducing the transition temperature) while Cr will create compressive strain (increasing the transition temperature). A suitable capping layer also needs to have minimal effect on the magnetic properties of the FeRh film. W is a paramagnetic material while Cr is antiferromagnetic at room temperature but quickly becomes paramagnetic when heated above 38 °C. Resistivity measurements confirm the change in temperature at which the lattice parameter change occurs for both Cr and W-capped samples, showing that they are indeed effective at altering the transition temperature. Cr-capped samples show a transition temperature at ~140 °C while W-capped samples begin their transition at ~100 °C.

As with the FeRh, Cr and W capping layers are deposited by dc magnetron sputtering, with these layers added after the annealing process is complete. Capping layer deposition must occur below ~100 °C else material from the capping layer will diffuse into the FeRh. This chapter investigates the possibility of interdiffusion across the FeRh/cap interface using EDX and EELS spectroscopy techniques as well as HAADF-STEM imaging.

6.2 Initial XPS

Initial FeRh growths were conducted with no additional Cr or W layer and were instead finished with an Al or MgO cap. As shown previously in polarised neutron reflectometry measurements²⁵, there is a change in scattering length density at the FeRh-MgO cap interface which suggests a ~ 10 nm Rh-rich area of the film exists. XPS depth profiling measurements were performed on FeRh with a 3 nm thick Al cap to determine if this effect could be mapped directly. Etching for the depth profile was performed using a 3 kV Ar⁺ ion beam. After each etch a spectrum was acquired to observe change in intensity of the Fe 2p, Rh 3d and Al 2p peaks. Figure 66 shows the background-subtracted changes in the Fe 2p and Rh 3d peaks with changing depth. The depth values were computed by approximating the etching time for an average of pure iron and rhodium. There are no obvious qualitative changes through the interface. By creating a normalised depth profile including the previous Fe and Rh peaks as well as the Al 2p peak the relative changes in Fe, Rh and the cap may be clearly seen. The graph shows that within the Al layer there is a small concentration of Rh while there is an Fe-rich region just within the FeRh layer. Beyond that, the Fe:Rh concentration balances although still some Al is found within the FeRh. It is important when discussing these results to note that XPS is surface-sensitive, but has an interaction volume of a few nm that affect how these results should be analysed. At the surface of the sample, some signal from within the film will be detected but its signal will be weaker relative to the material found on the surface itself. As a result, it may be interpreted that directly at the interface with the Al there is a deficiency of Fe, then moving further into the sample there is an Fe-rich region followed by equiatomic FeRh. This Fe-deficiency corresponds with the PNR measurements discussed before.

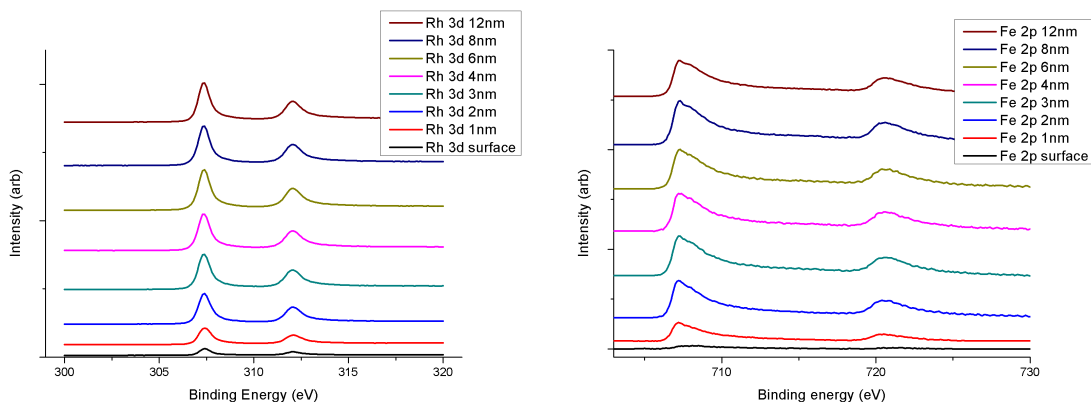


Figure 66: Background-subtracted Fe 2p and Rh 3d peaks from the surface of the sample to 12 nm into the thin film. The depth values were obtained by averaging the etching times for pure Fe and Rh.

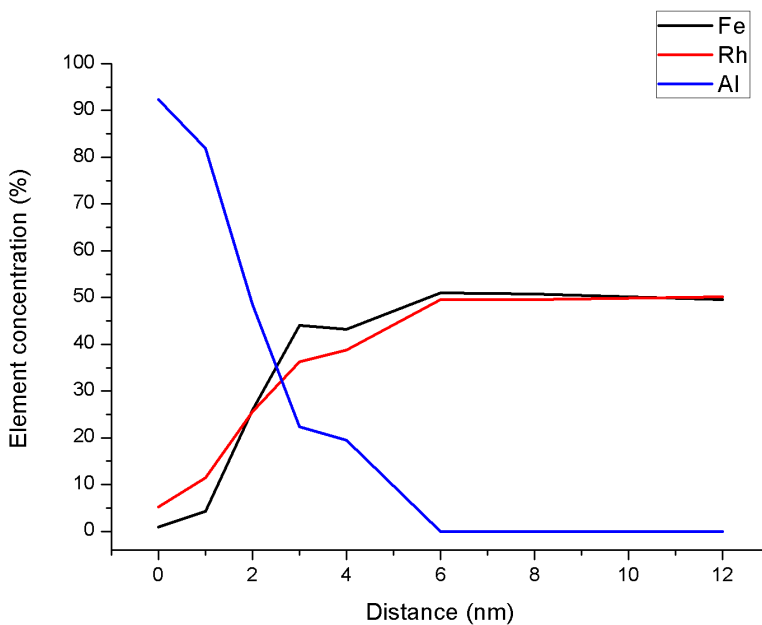


Figure 67: Depth profile created from the background-subtracted Fe 2p, Rh 3d and Al 2p peaks. Deep within the FeRh it may be seen as equiatomic but closer to the interface there are deficiencies of Rh and Fe. The interaction volume of electrons emitted means that signal nominally collected from the surface will also collect signal from a few nm within the sample. As a result, it is likely that there is a small Fe deficiency located at the FeRh-Al interface and then an Fe-rich region beyond that point. There is also a significant diffusion of Al into the top of the FeRh layer.

6.3 STEM-EDX Maps and Line Profiles

Chromium Cap

STEM-EDX maps were performed on many thin film cross-sections of Cr and W-capped FeRh films on a Tecnai TF20, with particular emphasis on Fe, Rh, O, Cr/W and Al (the top capping layer). Figure 68 shows maps for an FeRh film with a Cr cap prepared via an ion polishing method. As seen in the previous chapter and confirmed here, Fe and Rh appear to be uniform with no large Fe or Rh-rich regions. As well, an oxygen signal is detected throughout the sample and is likely due to surface oxidation in this cross-section. There is, however, a large amount of oxygen present in both the Cr and Al layers. Oxidation of aluminium is expected and indeed the layer is deposited on top of FeRh samples in order to preferentially oxidise. It also appears that the Cr layer has oxidised significantly as well. The Cr layer itself appears well-defined with no clear evidence of interdiffusion into the FeRh or vice versa. Finally, it can be seen that Al signal is detected within the FeRh. At the bottom of the maps is an area containing Al and O, which is likely a small amount of residue from the alumina suspension used during the sample dimpling process. It is also possible that some of this material has been redeposited during the ion milling process, explaining the Al signal within the FeRh. Figure 69 shows the same area in bright field view. On the far right of the image is a large amorphous area that corresponds with the Al and O signals observed in the EDX maps.

Figure 70 shows line profiles created from the maps in figure 68. The oxidation may be seen more clearly and it appears as though there is an oxidised region of FeRh close to the Cr interface. There appears to be much overlap between the Cr and Al layers, with the Al region having a shoulder within the Cr layer suggesting some interdiffusion into the chromium. No evidence of large scale interdiffusion between FeRh and Cr is detected here with this limited spatial resolution. The broadness of the curves are likely an artefact of the probe size (~ 5 nm) and not an interdiffusion effect. The Fe signal appears stronger close to the interface although it is difficult to confirm that

this is a real effect due to the significant variations in signal of both Fe and Rh through the film.

Tungsten Cap

Figure 71 shows maps for an FeRh thin film cross-section with a W cap, prepared by FIB. Fe and Rh signal is seen as uniform throughout the layer with minimal oxidation of the FeRh. Some oxidation is seen in the W cap as well as the Al. Interdiffusion between FeRh and W is not visible at this spatial resolution. There may be some redeposition of all major elements into the Pt layer on the surface of the film, but significant redeposition does not seem to have occurred.

Figure 72 shows line profiles created from figure 71. Some oxidation is visible in the Al and W layers, as well as a small amount of interdiffusion between the two. There is a possibility of interdiffusion at the FeRh-W interface, but this is likely due to the STEM probe size (~ 5 nm).

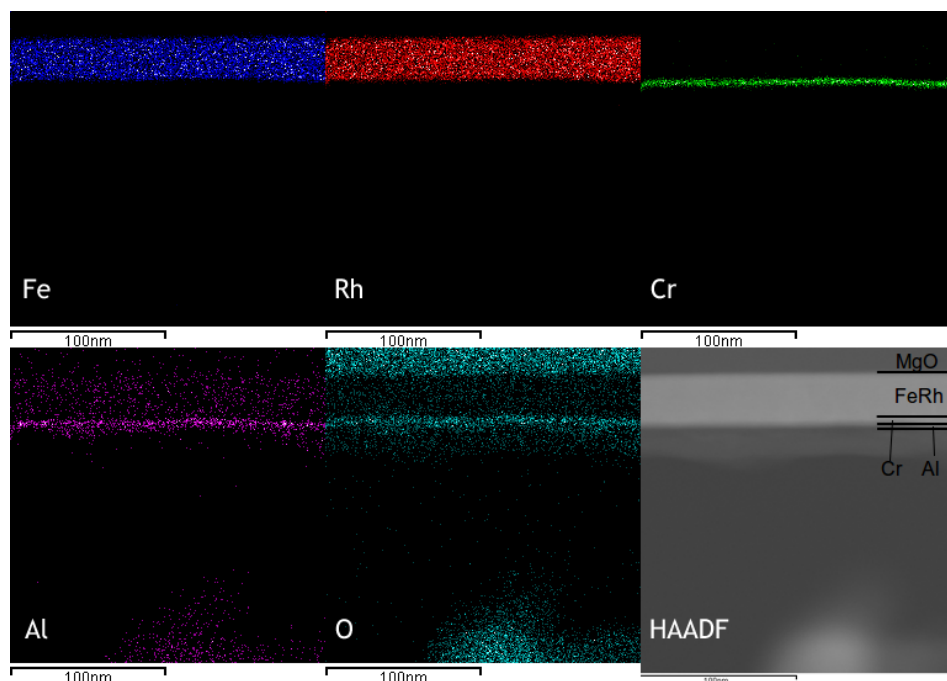


Figure 68: STEM-EDX maps taken from an FeRh film with a Cr cap prepared using ion polishing. No evidence of large compositional variation exists within the FeRh. The Cr layer is very well defined, although it appears highly oxidised along with the Al layer. The FeRh again appears to have suffered from surface oxidation. Al is detected throughout the FeRh, which is likely due to redeposition of alumina suspension used during the sample preparation process.

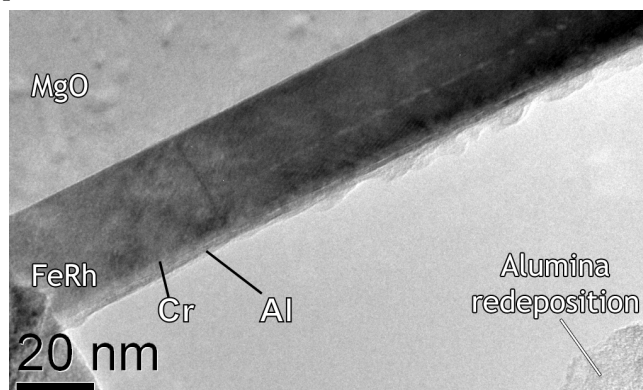


Figure 69: Bright field TEM image of the area shown in the STEM-EDX maps of figure 68. A large amorphous region is visible on the far right of the sample that corresponds with the Al and O signal found in the maps. This is likely to be residue of the alumina suspension used in the dimpling phase of the sample preparation process.

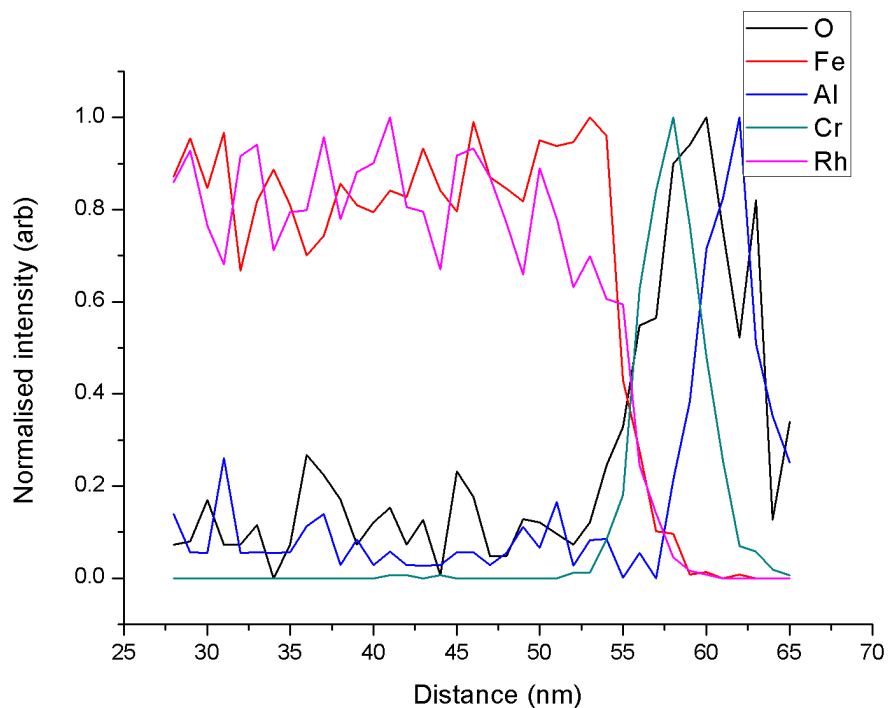


Figure 70: EDX line profile created from the maps in figure 68. There is little evidence of interdiffusion of Cr into the FeRh although the left side of the Al has a shoulder leading into the Cr, suggesting a small amount of diffusion. Both the Al and Cr layers are highly oxidised with some relatively strong signal (i.e. not an effect of surface oxidation) found within the first few nm of the FeRh. There is an increase in Fe concentration relative to Rh directly at the interface but no inferences may be made from this due to the large signal variation throughout the FeRh layer.

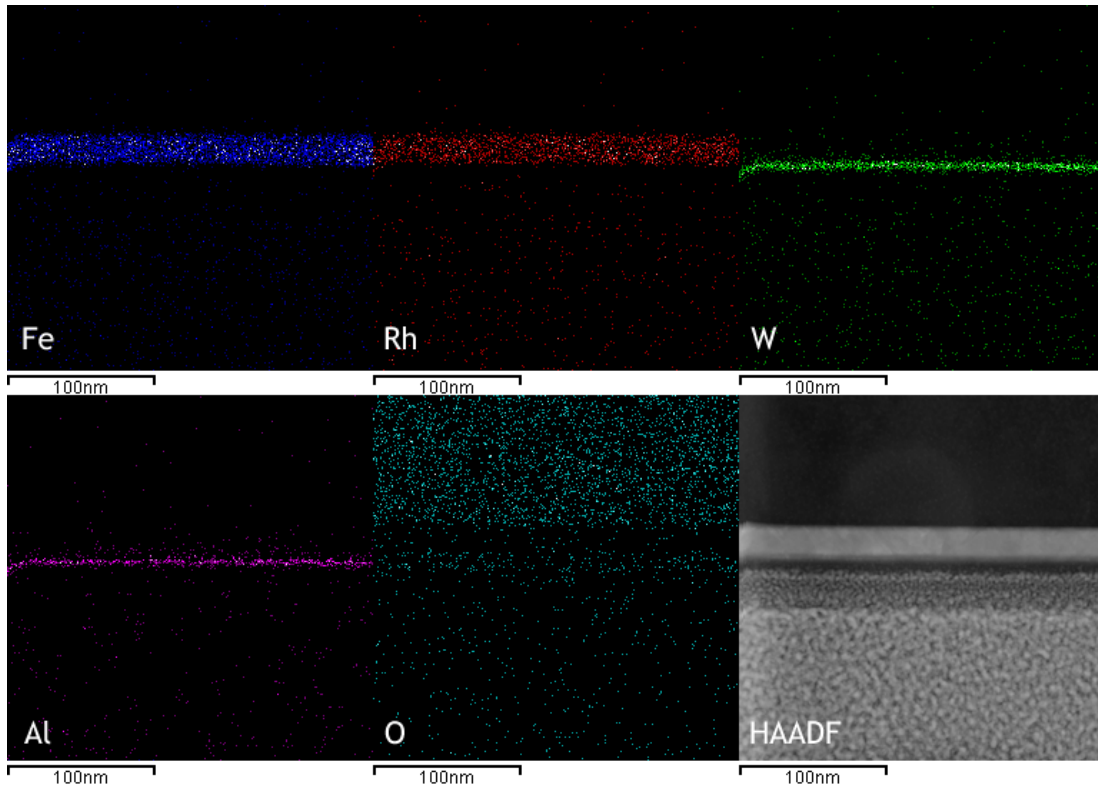


Figure 71: STEM-EDX maps taken from an FeRh film with a W cap prepared via FIB. No evidence of large compositional variation exists within the FeRh. The Cr layer is very well defined, although it appears highly oxidised along with the Al layer. The FeRh again appears to have suffered from surface oxidation. Al is detected throughout the FeRh, which is likely due to redeposition of alumina suspension used during the sample preparation process.

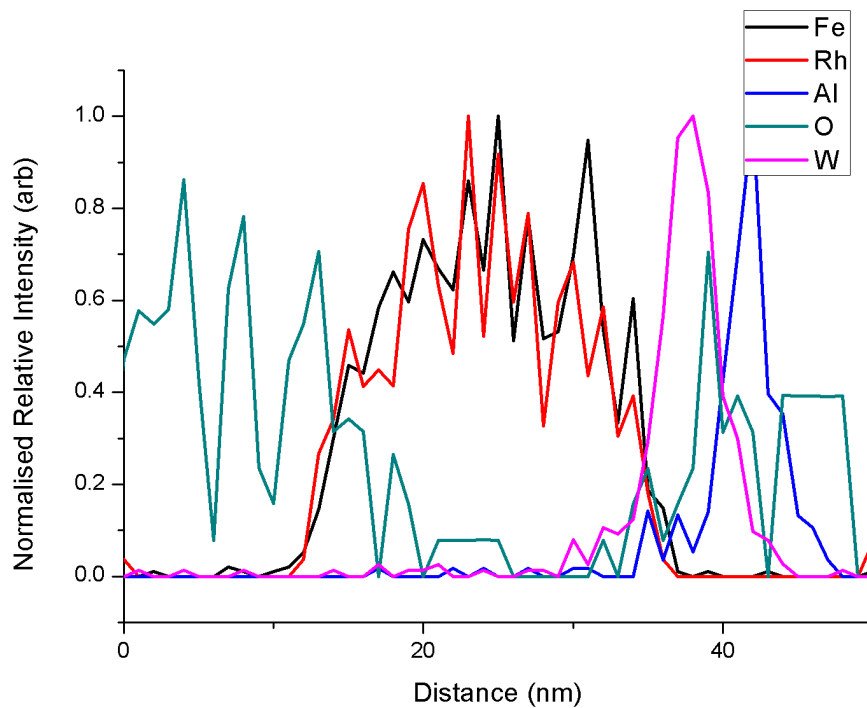


Figure 72: EDX line profile created from the maps shown in figure 71. there is little evidence of interdiffusion between FeRh and W seen here. The W and Al layers are partially oxidised with a small amount of interdiffusion between these two layers.

6.4 STEM-EELS Spectrum Images and Line Profiles

Chromium Cap

As discussed in the previous chapter, STEM-EELS spectral images and HAADF images were obtained using a Nion UltraSTEM 100 with C_s correction at 100 kV. Figure 73 shows a typical HAADF-STEM image of the FeRh/Cr interface. Relative to the FeRh/MgO interface seen in figure 61, the FeRh/Cr interface is less well-defined although the epitaxial matching can still be seen. It is expected that the interface is less well-defined as surface roughness will result in the observation of both film and cap when observing from a cross-sectional view. The strain in the Cr cap also affects channelling of the beam and gives rise to contrast in the HAADF. The Cr is also shown to be single crystal in nature. There is a large amount of strain around the interface particularly within the FeRh which makes it difficult to determine the terminating layer in the FeRh, although within the highlighted area it appears as though the film terminates with Fe. The surface roughness also means that it is unlikely for there to be a uniform terminating layer.

Initial EELS data sets of the FeRh/Cr interface mapping the Fe $L_{2,3}$, Rh $M_{4,5}$, O K and Cr $L_{2,3}$ edges show little evidence of interdiffusion. Some Fe signal was detected within the Cr layer but may easily be caused by background noise. To further investigate, a spectrum image across the entire FeRh film including the MgO interface was acquired, providing a reference for zero (or at least minimal) Fe and Rh signal as the MgO layer has been found to contain no significant amounts of FeRh. Figure 74 shows maps for Fe, Rh, O and Cr throughout the layers. Here it can be seen that there is a significant Fe signal detected within the Cr layer. However, no evidence of Cr or Rh diffusion is visible. A small amount of oxidation is seen within the FeRh layer although little oxygen is found within the Cr cap. This is certainly Fe diffusion into Cr as the HAADF clearly shows the contrast difference between the FeRh and Cr, with Fe and Cr detected within the nominally Cr layer.

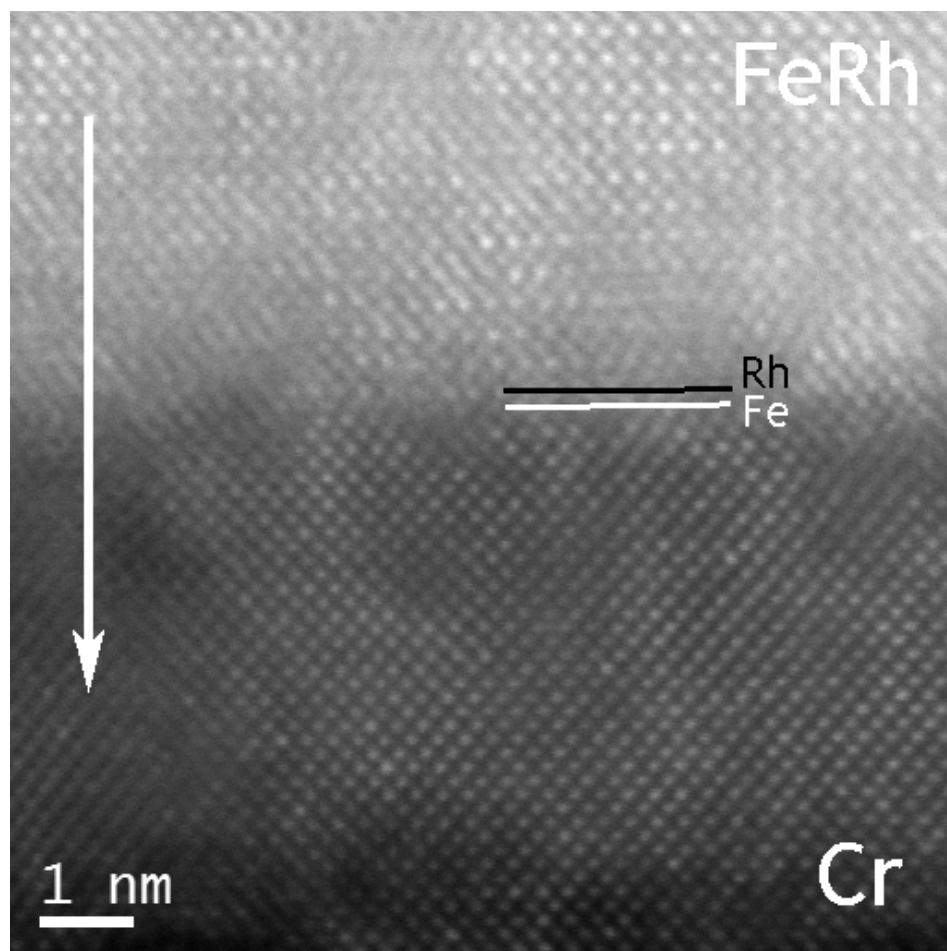


Figure 73: HAADF-STEM image of the FeRh/Cr interface along the [100] FeRh (and Cr) zone axis. While not as well-defined as the FeRh/MgO interface seen in other HAADF-STEM images (e.g. figure 61) the epitaxy between the layers is barely visible as well as the single crystal nature of the chromium. The terminating layer is ambiguous due to the large amounts of strain affecting the contrast combined with the roughness of the interface, however the Fe and Rh are labelled. Growth direction of both FeRh and Cr is shown with an arrow.

By creating line profiles from the data in figure 74 the interdiffusion may be seen more clearly. The source of the interdiffusion seems to be the top few nm of the FeRh layer, which is expected

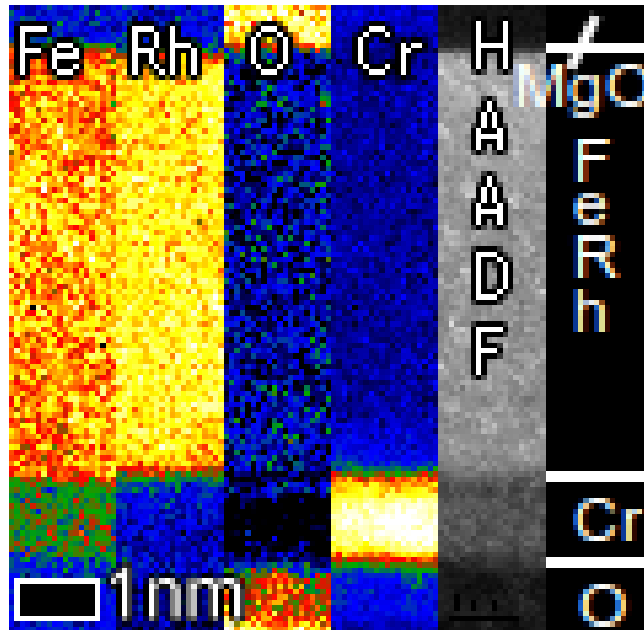


Figure 74: STEM-EELS spectral images showing elemental maps of Fe, Rh, O and Cr with a HAADF image for comparison. The colours indicate a temperature scale ("hotter" colours show higher signal). There is no evidence of Rh or Cr diffusion around the FeRh/Cr interface however it can be seen that a large amount of Fe is visible within the nominally Cr layer. There is also little oxygen signal found within the Cr layer while it is found elsewhere within the FeRh.

as the diffused material would have to move from an adjacent area. Very small quantities of Cr are detected within the FeRh. There is oxidation of the Al layer (the first shoulder to the right of the Cr) as well as a small amount of O signal found in the last few Angstroms of the Cr cap.

Fe diffusion out of FeRh is enough to have an effect on the phase transition. As previously seen in the FeRh phase diagram, a deficiency of Fe (to $\sim\text{Fe}_{45}$) causes an increase in the transition temperature. Beyond this point, the transition temperature drops sharply until no AFM-FM transition is seen. As a result, the interdiffusion at the interface may pair with the strain from the Cr cap to further increase the FeRh transition temperature. However, as both effects are seen together it is

not possible to separate them and therefore fine control of the transition with a Cr cap is difficult.

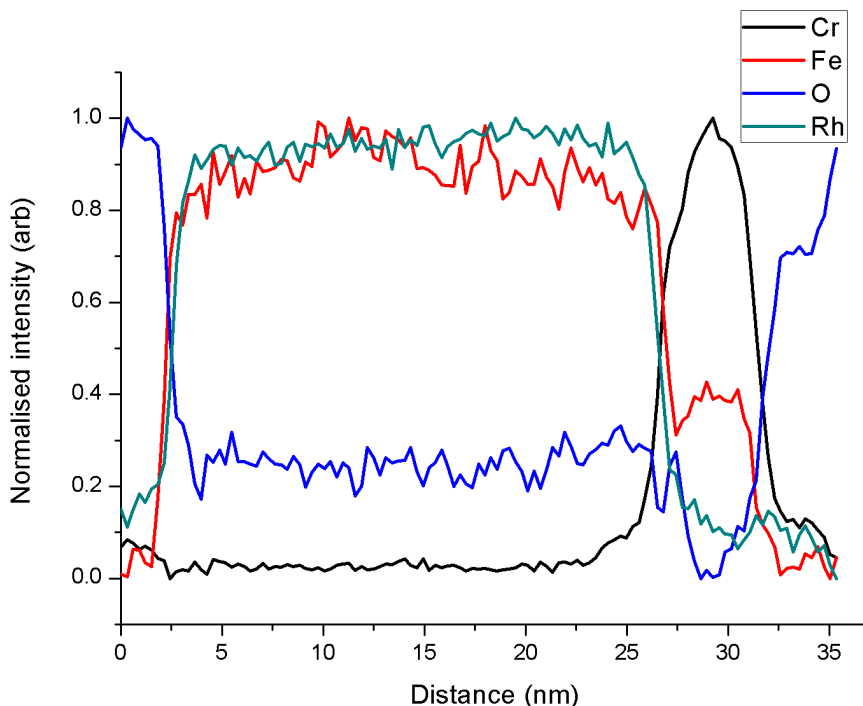


Figure 75: Line profile plot created from the elemental maps in figure 74. By including the FeRh/MgO interface to observe relative drop in Fe and Rh concentration at the cap interface, it can be seen that iron is detected throughout the chromium cap, with the signal eventually disappearing when the chromium layer ends. Also, it appears as though the ratio of Fe:Rh varies slightly through the film. There is an Fe-deficient area close to the FeRh-Cr interface which, if Fe is detected within the Cr cap, makes sense as the Fe would have diffused from the neighbouring region.

Quantifying the EELS map for Fe and Cr gives an idea of the percentage of Fe content within the Cr layer. Figure 76 gives a line profile showing the change in Fe and Cr concentration across the interface. Within the Cr there is a relatively consistent 10% Fe content.

These data may be compared to metal phase diagrams (figure 77 to give an idea of the solubility

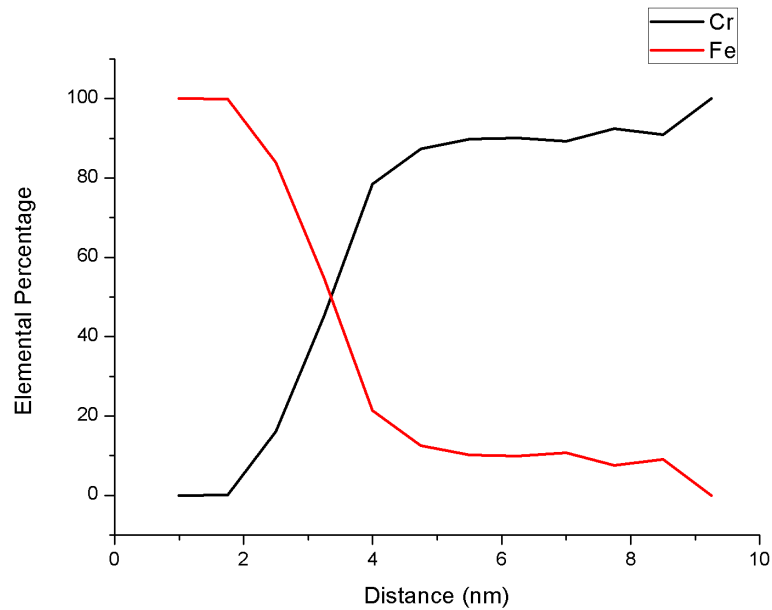


Figure 76: Quantified EELS line profile for Fe and Cr only. Within the Cr layer there is a stable Fe concentration of $\sim 10\%$.

of various elements for the bcc/CsCl phases of the possible alloys. The phase diagram for FeCr shows that intermixing between the two is possible with no change in crystal structure, remaining bcc regardless of the atomic ratio¹⁶⁷. RhCr multiphase alloys exist with bcc and a Cr_3Rh until 22% atomic ratio, at which point Cr_3Rh exists alone¹⁶⁸. The solubility of Fe into Cr without disrupting the crystal phase fits with the STEM-EELS data collected.

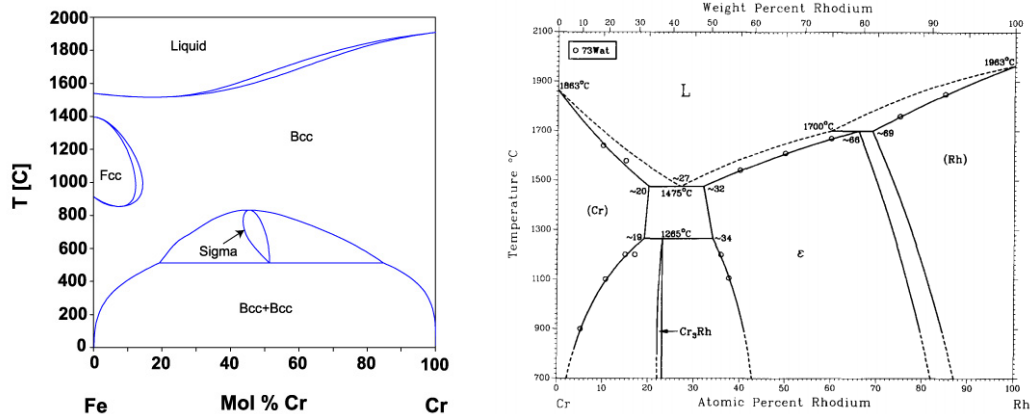


Figure 77: Phase diagrams for Cr-Fe and Cr-Rh alloys. CrFe alloys remain in a bcc phase regardless of ratio. Adding Rh to Cr creates a multiphase CrRh which remains bcc until 22% atomic Rh, where a Cr₃Rh alloy is formed^{167,168}.

Tungsten Cap

For W-capped samples, the EELS spectral images were divided into two separate runs to retain a good energy resolution due to the high energy loss (1800 eV) of the W_{4,5} edge relative to other elements, in particular the Rh M_{4,5} edge (450 eV). The Fe L_{2,3} edge (700 eV) was acquired in both data sets. STEM-EELS spectral images of the W-capped FeRh films show compositional data very different to the Cr-capped samples. As with the Cr-capped film, the HAADF-STEM (figure 78) shows a relatively well-defined interface between the W and FeRh. Again, this interface is rougher than seen at the FeRh-Mg interface. The W cap is seen to be single crystal although in some areas the lattice appears slightly distorted and there are some grain boundaries. Presence of strain will affect channelling of electrons and therefore HAADF contrast at the interface. It is not possible to determine the terminating layer in the FeRh at this interface.

The EELS maps themselves show that interdiffusion across the interface has not occurred in

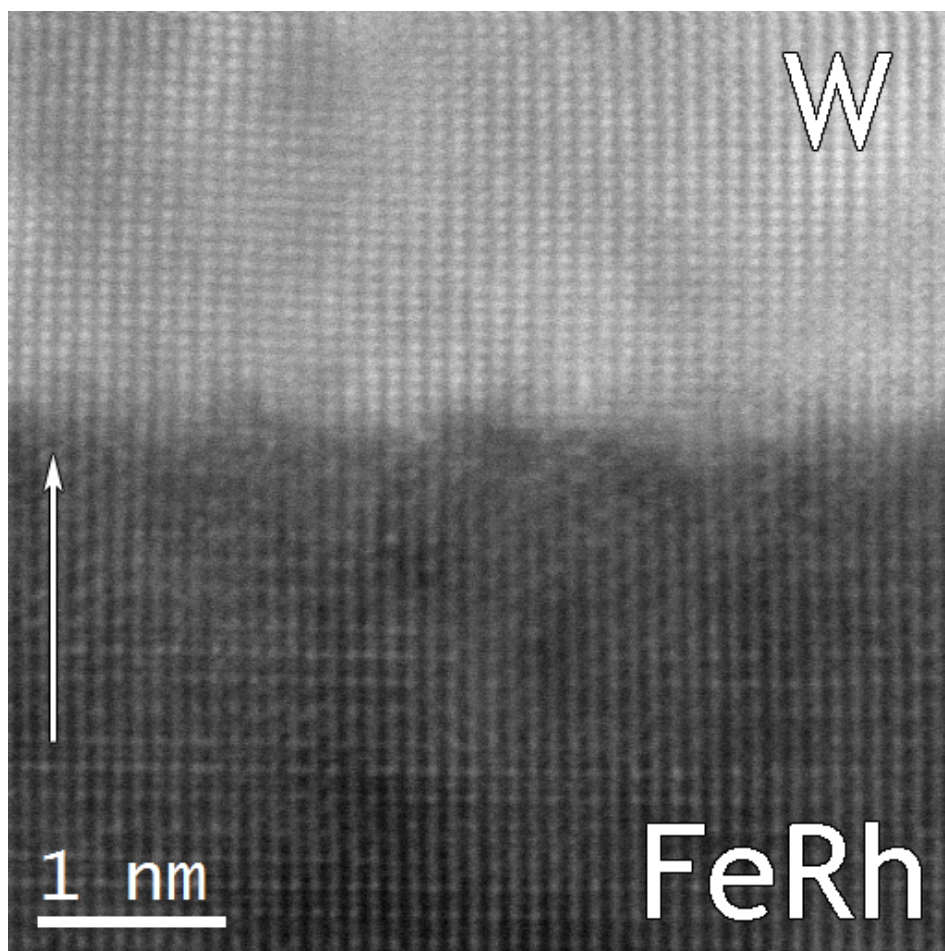


Figure 78: HAADF-STEM image of the FeRh/W interface along the [110] FeRh (and W) zone axis. In a similar manner to the Cr layer previously described in figure 73 the layer is seen as less strongly defined than the FeRh/MgO interface (figure 61) due to the roughness of the FeRh layer and how this roughness is displayed in a 2D projection. Visibility of a terminating layer is difficult due to the high strain affecting the contrast and the distortion of the lattice. However, the W lattice is seen here to be a single crystal. Growth direction of the FeRh and W crystal is indicated by an arrow.

this sample despite the same growth conditions (aside from the alternate capping layer) and sample preparation method (FIB) used. Figure 79 shows the maps obtained for W, Fe, Rh and O throughout

the FeRh layer with the HAADF image of the same area for comparison. In Fe there is no signal detected within the W layer as seen in the Cr-capped sample and Rh and W see no evidence of interdiffusion as well. The O map shows a small amount of oxidation of the W layer but very little O signal is found within the FeRh.

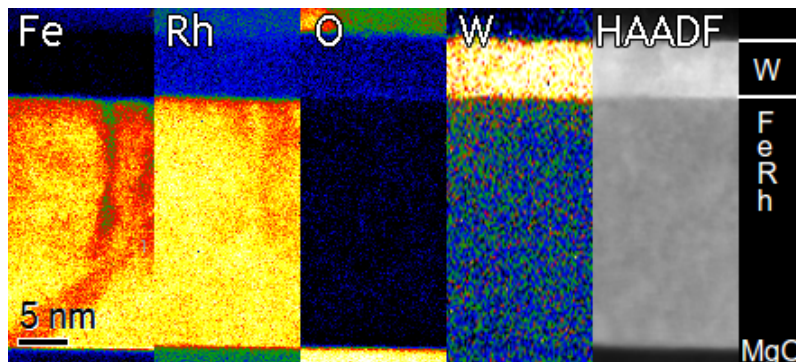


Figure 79: STEM-EELS spectral images showing elemental maps of Fe, Rh, O and W as well as a HAADF image of the area. The colours indicate a temperature scale ("hotter" colours show higher signal). Unlike the Cr-capped sample, the interface is very well defined and shows no evidence of diffusion between the layers. There is also a small degree of oxidation within the W layer. In the image a large variation in Fe content can be seen, when comparing to other samples this appears to be an anomaly with no similar compositional variations seen elsewhere.

By creating a line profile from figure 79, the lack of interdiffusion is more clearly visible. The interface between the W and FeRh is clearly defined with no strong interdiffusion in either direction. There is a large amount of noise from the W signal located within the FeRh simply due to the low signal:noise ratio from using edges with high energy loss. The oxidation within the W layer is again clearly visible and promptly falls off within the FeRh layer, although a very thin 1-2 nm oxide layer exists within the FeRh itself.

Again comparing to binary metal phase diagrams (figure 81) it can be seen that both Fe and Rh will form an alloy with W but the bcc W is only kept for atomic percentages of 3% for Rh and

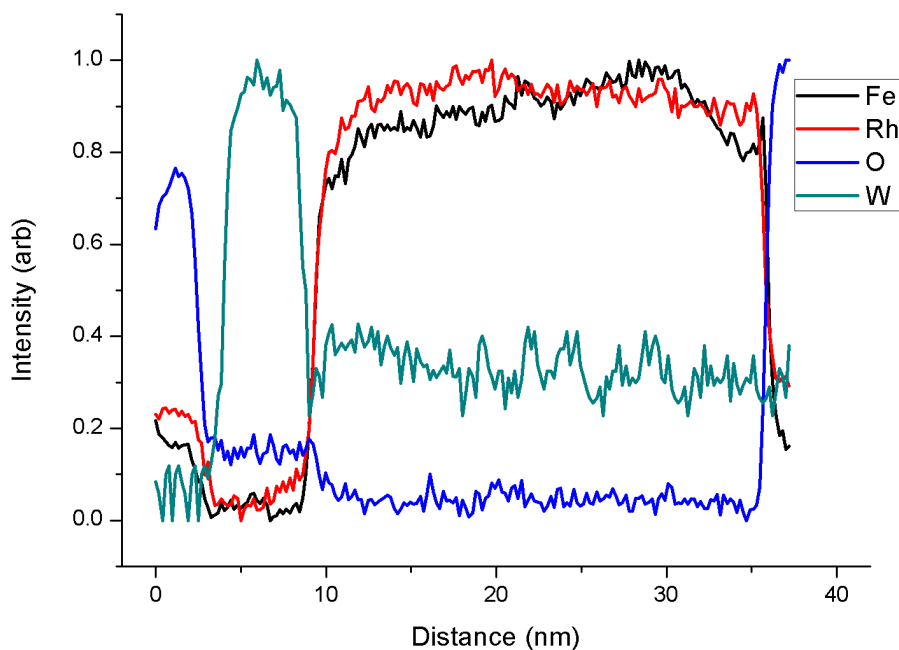


Figure 80: Line profile created from figure 79. The lack of interdiffusion across the FeRh-W interface is obvious with no significant composition changes occurring. There is a large amount of noise in the W curve within the FeRh due to a high signal:noise ratio using an edge with such a high energy loss. Finally, the oxidation of the W is seen with a small 1-2 nm region of FeRh also suffering from a small amount of oxidation.

2% for Fe¹⁶⁹. In both cases, adding excess Fe and Rh destroys the bcc crystal of the W, explaining why interdiffusion is not visible across this interface in the same way as for Cr-capped samples.

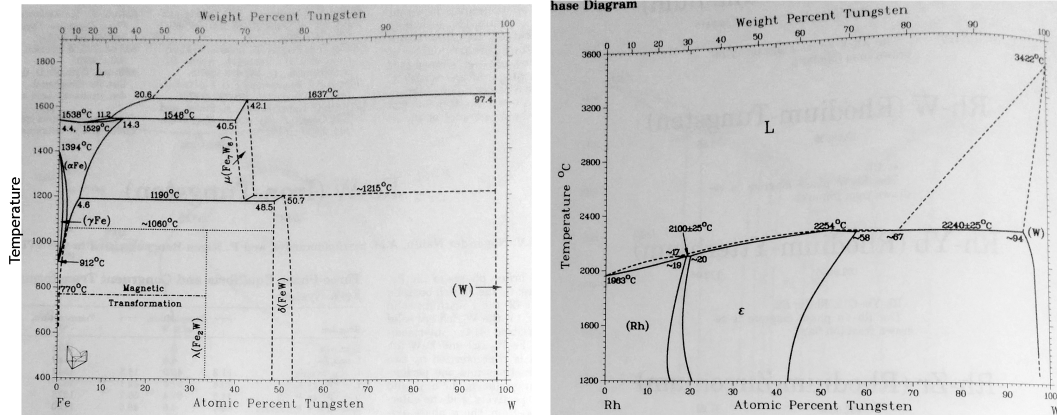


Figure 81: Phase diagrams for W-Fe and W-Rh alloys. In both cases W allows a small percentage of alloying (3% for Rh and 2% for Fe) after which a multiphase alloy exists for both¹⁶⁹.

6.5 EELS Edge Analysis

It is not expected that there will be changes in EELS near edge fine structure across the interface with the capping layers but for completeness the data are shown here. Figures 82 and 83 show the change in the Cr L_{2,3} and Fe L_{2,3} edges respectively for the FeRh Cr-capped sample. In both the Fe and the Cr edges there is no evidence to suggest that fine structure changes due to bonding occur.

As with the Cr-capped sample, it is extremely unlikely that a change in fine structure will be observed in W-capped samples. Figures 84 and 85 show background-subtracted spectra of the W M_{4,5} edge and Fe L_{2,3} edges respectively across the interface. Again, there are no changes visible in either spectrum other than drops in intensity across the interface. Measurements of the L₃/L₂ ratios - which may be affected by alloying¹⁴⁶ - yield no significant change, with the value remaining ~1.1 for Cr and ~1.8 for Fe.

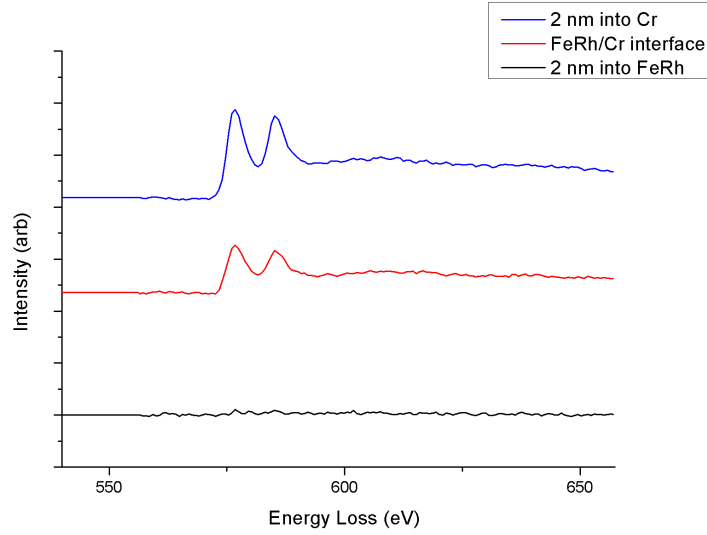


Figure 82: Background-subtracted EELS spectra of the Cr $L_{2,3}$ edges at the FeRh/Cr interface. There are no obvious changes across the interface other than an increase in intensity.

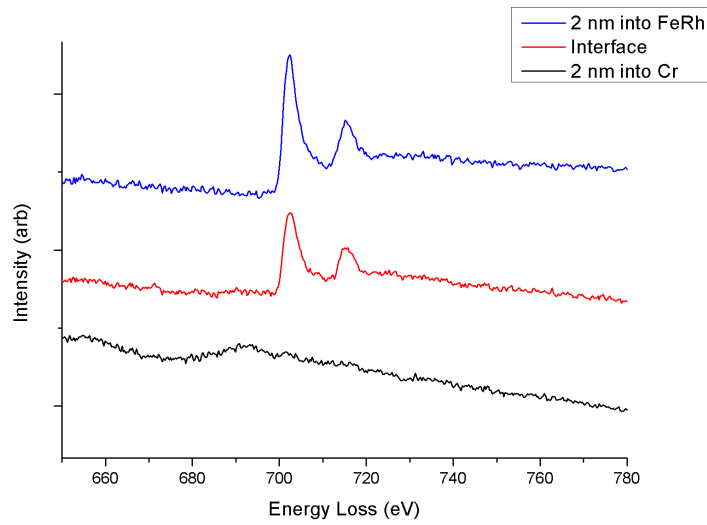


Figure 83: Background-subtracted EELS spectra of the Fe $L_{2,3}$ edges at the FeRh/Cr interface. There are no obvious changes across the interface other than an increase in intensity.

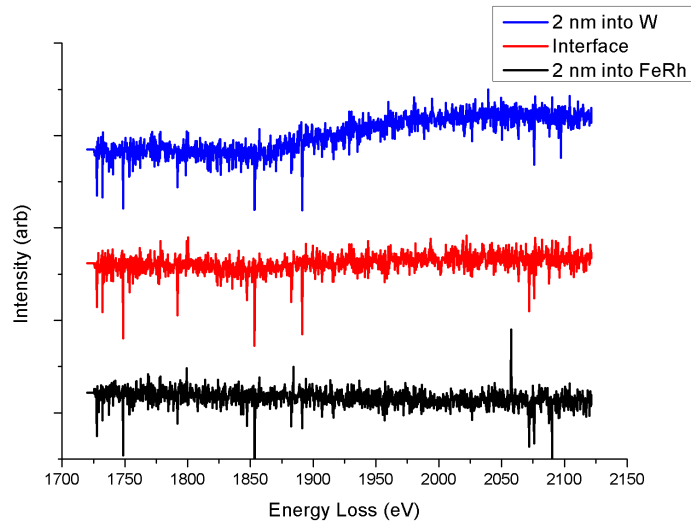


Figure 84: Background-subtracted EELS spectra of the W $M_{4,5}$ edge at the FeRh/Cr interface. The W edge is extremely broad and is noisy here due to the high energy loss. The edge intensity drops quickly at and beyond the interface into the FeRh.

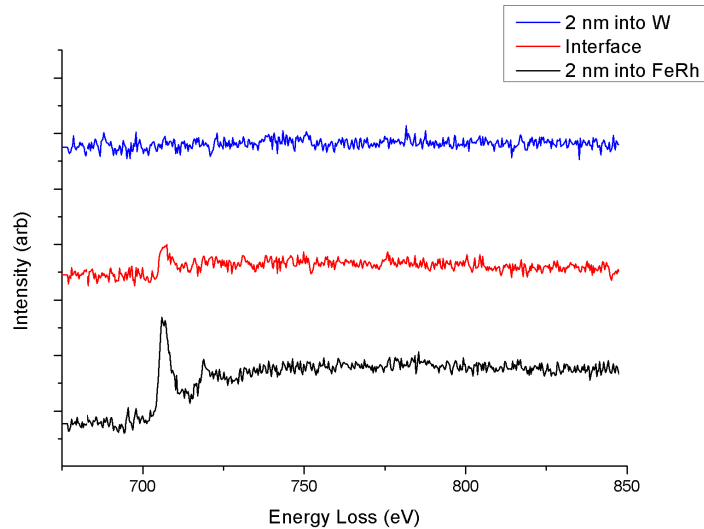


Figure 85: Background-subtracted EELS spectra of the Fe $L_{2,3}$ edges at the FeRh/W interface. The intensity of the FeRh edge decreases further into the W layer but there are no changes that cannot be attributed to noise. The bottom curve shows two small, broad peaks both before the Fe edge that are likely attributable to extended energy loss fine structure (EXELFS) oscillations from the $Cr_{2,3}$ edge.

6.6 Chapter Summary

While strain is clearly a factor involved in capping layers affecting the transition temperature, composition change and interdiffusion cannot be ruled out. Conventional STEM-EDX on Cr-capped samples did not show any interdiffusion of FeRh or Cr across their interface, but it did find that a small amount of oxidation occurs in the first few nanometres of the FeRh. More importantly, high resolution aberration-corrected STEM-EELS imaging found a significant amount of interdiffusion across the FeRh-Cr interface, with the movement of Fe into the Cr layer. As a result, there is an apparent decrease in Fe concentration in the FeRh layer close to the Cr cap. Observation of the oxygen edge shows no signal within the Cr layer. Analysis of the fine structure for both Cr and Fe show no changes due to chemical bonding, which is expected at a metal-metal interfacial region. The Fe interdiffusion is significant as a small excess of Rh will increase the transition temperature slightly. As a result, the measured increase seen in the transition temperature for Cr-capped samples may not be solely caused by the epitaxial strain, with composition playing a role.

In comparison, the elemental analysis tells a different story for W-capped samples. Whereas STEM-EELS shows significant interdiffusion of Fe into the Cr, nothing similar occurs between the FeRh and W, which instead is shown to have a well-defined interface and no large-scale interdiffusion across it. Interestingly, the concentration of oxygen is different, with the detection of O within the capping layer, which is different to the case of the Cr cap. Again, fine structure analysis does not provide any interesting information about bonding between the layers.

Tungsten is clearly shown to be a suitable capping layer for FeRh as it epitaxially strains the FeRh without any alteration to the chemical composition of the film. Chromium, on the other hand, is less suitable for affecting the transition temperature purely via epitaxial strain due to the iron diffusion that has taken place. As a result, it is harder to control the transition temperature effectively.

7 Changes in Strain and Magnetism by Heating Through the FeRh Transition

7.1 Introduction

Although the dynamics of the magnetostructural transition are fairly well documented for thin films^{102,170}, little work has discussed the actual nucleation and growth of the ferromagnetic phase within FeRh films from a cross-sectional standpoint. Synchrotron X-ray experiments show a coexistence of lattice parameters (and therefore a phase coexistence) through the transition in strained thin films, suggesting that the epitaxial strain across the interface serves as a point of nucleation for the ferromagnetic phase. From a magnetic point of view, XMCD, PEEM and MFM experiments have observed the nucleation and growth of ferromagnetic domains and their coexistence with antiferromagnetic domains and provide evidence to suggest that the domains nucleate from interfaces and grain boundaries^{52,100,171}.

Bright field imaging by isolating the central spot only provides evidence of strain fields to observe what is essentially a change in lattice parameter. This, paired with magnetic imaging in the TEM using Lorentz techniques via both Fresnel and differential phase contrast imaging, can provide data regarding the phase transition as the magnetic and structural changes are linked. Here, various experiments involving heating stages have been performed to observe the dynamics of the transition on both plan view and cross-sectioned samples.

7.2 Strain Field Heating Experiments

Differences (and therefore changes) in lattice parameter can be qualitatively observed using both bright and dark field TEM. Using a heating stage the temperature may be increased through the transition to observe how the structure of FeRh changes. Many different cross-sectional samples were used, differing in terms of sample preparation method and capping layer. The first sample

shown here is FeRh with a Cr capping layer prepared by the conventional ion polishing method. Starting at room temperature, the temperature was increased at 3 °C increments up to 200 °C (i.e. far past the expected transition temperature). Figure 86 gives an example of the contrast change with temperature. At room temperature there are small pockets of contrast along both sides of the interface. At 85 °C it can be seen that these regions are beginning to expand into the rest of the FeRh. At 97 °C there is now a large dark band running along the MgO interface as well as some dark areas on the FeRh side of the cap interface connecting together. It may also be seen that some contrast is now appearing within the capping layer itself. Finally at 166 °C much of the FeRh is dark as well as most of the capping layer. The contrast change in the Cr cap with temperature makes sense as the cap is seen to be granular in nature in previous HRTEM and HAADF images. Although the capping layer is exerting a compressive strain on the FeRh, as the FeRh makes its transition to the FM phase the jump in lattice parameter will exert more strain on the capping layer. The contrast changes in the FeRh are best explained by assuming nucleation of strained regions begin at discrete points along both interfaces before growing and coalescing into larger areas. These observations are in line with the expected phase coexistence of FM and AFM in the middle of the transition.

Again using the aforementioned sample, a region with a suspected grain boundary was used as a reference point in observing contrast change (figure 87). Starting again at room temperature but instead increasing by 10 °C through the expected transition point, it can be seen that some small areas of contrast exist along both interfaces as well as a very large dark region adjacent to the defect along the cap interface. At 130 °C, this dark region begins to expand and a second dark region forms at the interface with MgO on the other side of the defect. At 150 °C these regions have expanded further and dark contrast begins to fill the film albeit with fewer nucleation points than in figure 86. Finally at 190 °C the sample is far within the expected FM region and darker contrast dominates.

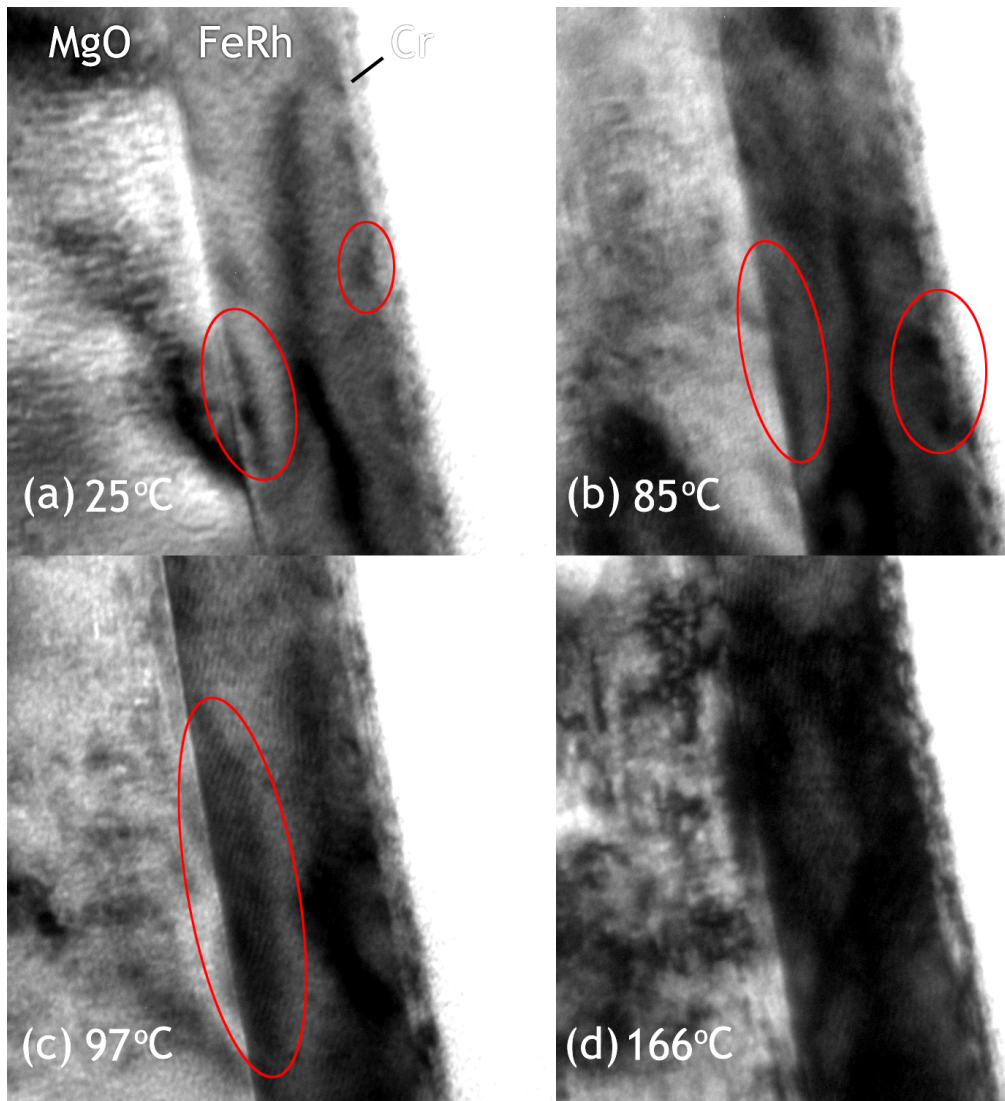


Figure 86: Bright field heating experiments of FeRh with a Cr cap prepared using ion polishing at (a) room temperature (b) 85 °C (c) 97 °C (d) 166 °C. (a) At room temperature, some pockets of contrast are visible. (b) As the temperature is increased these regions become larger until (c) the regions can be seen to coalesce. (d) Finally, within the expected FM phase most of the sample now appears dark. This suggests strain nucleates at the interfaces and propagates through the sample.

Despite the fact that the data in figures 86 and 88 are acquired from the same sample, the temperatures at which the principal changes occur are apparently different. There are two potential factors that could cause this. Firstly, the positions along the film where the results are taken may have an effect. The defect is located in an extremely thin area of the sample close to the edge, affecting the thermal conductance and therefore meaning the recorded temperature (i.e. the temperature at the thermocouple in the TEM specimen holder) is different to the real temperature in the observed area. Secondly, the temperature increase when observing the defect was much sharper than the other area. It could potentially be that there is a lag between the recorded temperature and the temperature of the sample that requires a longer period of stabilisation than was given. It is also important to note that this is not direct imaging of the phase transition and the phase transition may only be inferred from the contrast changes when heating. Changes in contrast may also arise due to changes in sample orientation caused by drift upon heating. It could be argued, using figure 88 as an example, that orientation change is minimal as the large jump between (a) and (b) results in a minimal change in contrast for the Cr cap and MgO layer but the effect cannot be completely ignored.

Further experiments performed on a FIB section (FeRh with an Al cap) did not produce similar results. Figure 89 shows the sample at room temperature and 150 °C. Unlike the previous sample, contrast changes through heating are not visible and it can be seen that there is no obvious pattern to the contrast within the film. Indeed, unlike the aforementioned samples rather than a slow creep of dark contrast from the interface it is found throughout the film. A second FIB section (FeRh with a Cr cap) yielded similar results, with no obvious change in contrast with increasing temperature. From these experiments it seems likely that samples prepared using this method are somehow altered, disrupting the phase transition. It is well known (and discussed previously) that the focused ion beam may create ion-implanted amorphous layers on the top and bottom of the sample with a thickness of ~5-10 nm. However, as this is also a phenomenon that exists occurs with

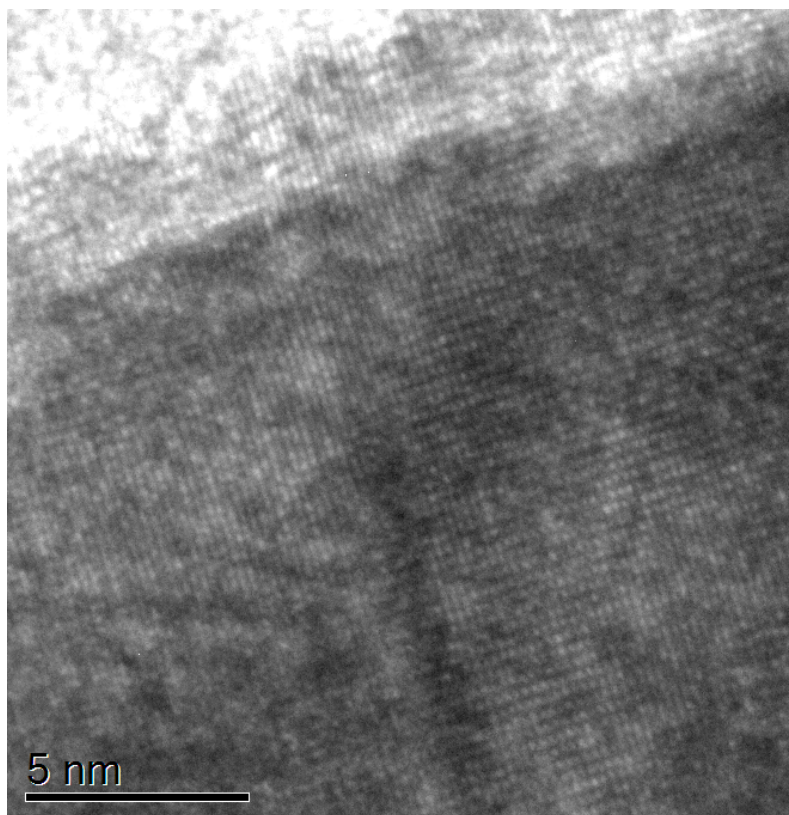


Figure 87: HRTEM image of a grain boundary located within an FeRh film along the [110] zone axis. The line of dark contrast indicates the boundary. The FeRh on the right of the boundary is observed along the zone axis while the FeRh on the left is slightly off-axis.

ion-polished samples it is unlikely that this is the sole cause for the destruction of the transition.

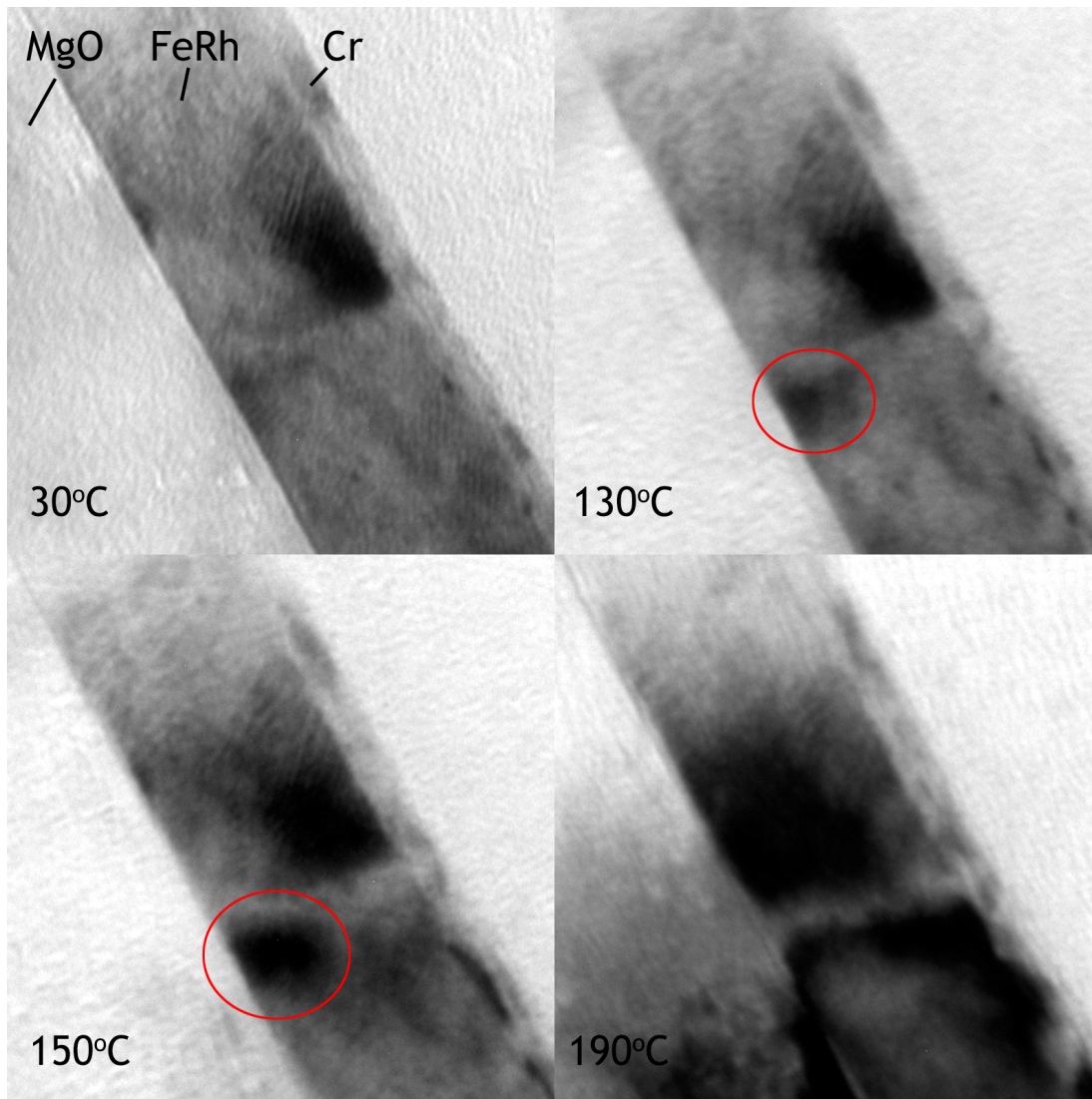


Figure 88: Bright field heating experiments of FeRh with a Cr cap prepared conventionally observing a grain boundary in the FeRh structure at (a) 30 °C (b) 130 °C (c) 150 °C (d) 190 °C. (a) At low temperatures, there is a large area of contrast close to the grain boundary. (b) As the temperature is increased area of contrast appear although are constrained to opposite corners adjacent to the substrate and cap interface. (c) Heating further the areas of contrast increase in size and contrast begins to form at the interfaces. (d) At high temperatures far into the expected FM phase much of the film appears dark.

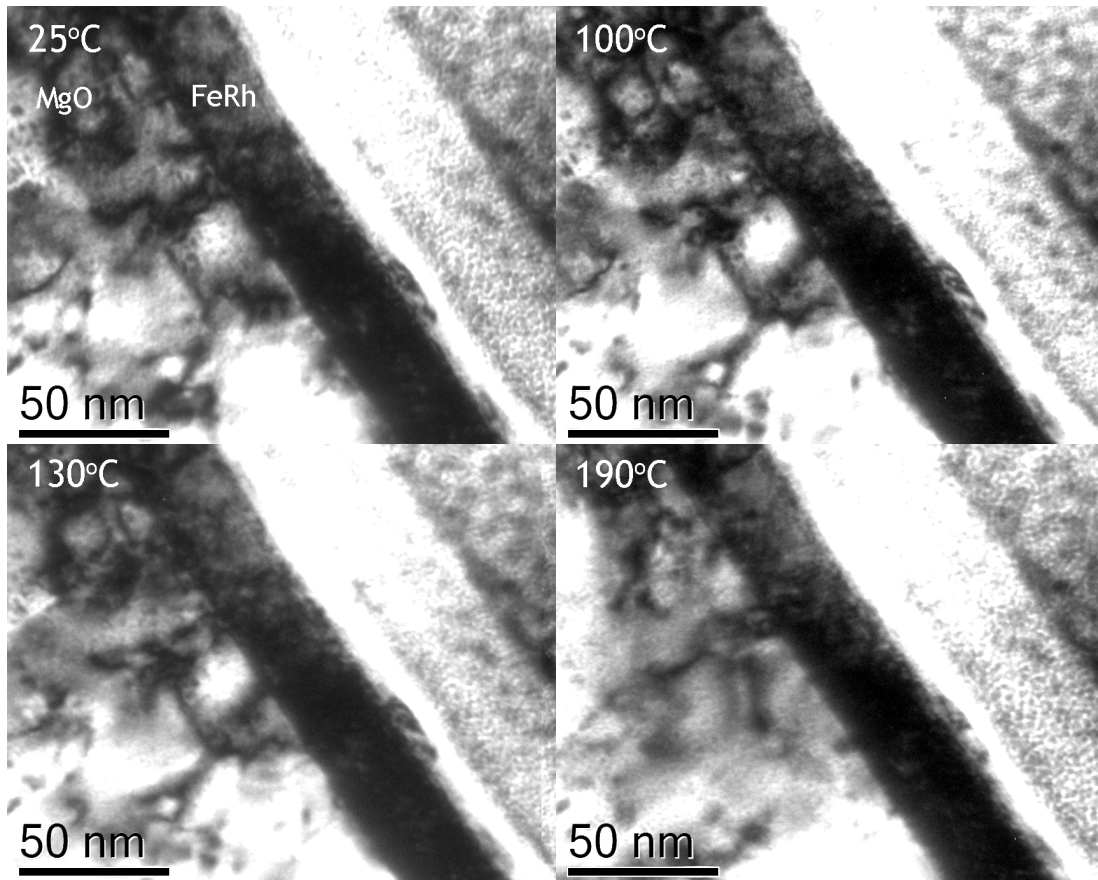


Figure 89: Bright field heating experiments of FeRh with an Al cap prepared using a focused ion beam at (a) room temperature (b) 100 °C (c)130 °C (d) 190 °C. Unlike previous experiments on different samples, there is no obvious change in contrast when heating through the transition and instead there is dark contrast even at room temperature.

7.3 Diffraction Pattern Changes Across Transition

The change in lattice parameter across the transition should result in a change in the diffraction pattern through the transition. Initial experiments on an FeRh Cr-capped FIB section were performed in the AFM and FM phases to observe any potential difference. The diffraction patterns recorded were unexpected and contained many extra ordering spots not previously seen in either X-ray or electron diffraction. Figure 90 shows these diffraction patterns obtained using scanning diffraction integrated over the FeRh area. A typical pattern (e.g. as seen in figure 47) shows a typical CsCl structure with a rectangular pattern. The scanning diffraction patterns have the same basic ordering but also visible are many extra spots indicating further ordering. The pattern remained unchanged through the transition and when considering the lack of contrast change in the strain heating experiments again it can be seen that FIB-prepared cross-sections do not exhibit the magnetostructural phase transition. These spots could be a cause of bending of the lamella due to strain, damage from the FIB preparation process or extra ordering of FeRh in the FM phase. It is unlikely that these spots are due to bending of the lamella or FIB damage as extra ordering spots would be visible for all layers and FIB damage would instead cause amorphisation.

To further understand the diffraction pattern seen in the previous FIB-prepared cross section, selected area diffraction experiments were performed a plan view sample. Figure 91 shows the change in diffraction pattern for a plan view sample. The principle FeRh 001 and 011 diffraction spots show no obvious change in position, aside from a slight rotation that is probably due to sample drift as opposed to any real change in structure. There is heavy distortion in the diffraction pattern towards the edges due to the set-up of the microscope so the changes may only be seen as relative. A lattice parameter change of 0.3% is unlikely to be visible but figure 90 provides some evidence to suggest that there is a change in the crystal structure when making a transition to the FM phase which is not visible here. This means that the extra ordering spots are either created by the FIB preparation process or are only visible along a certain zone axis.

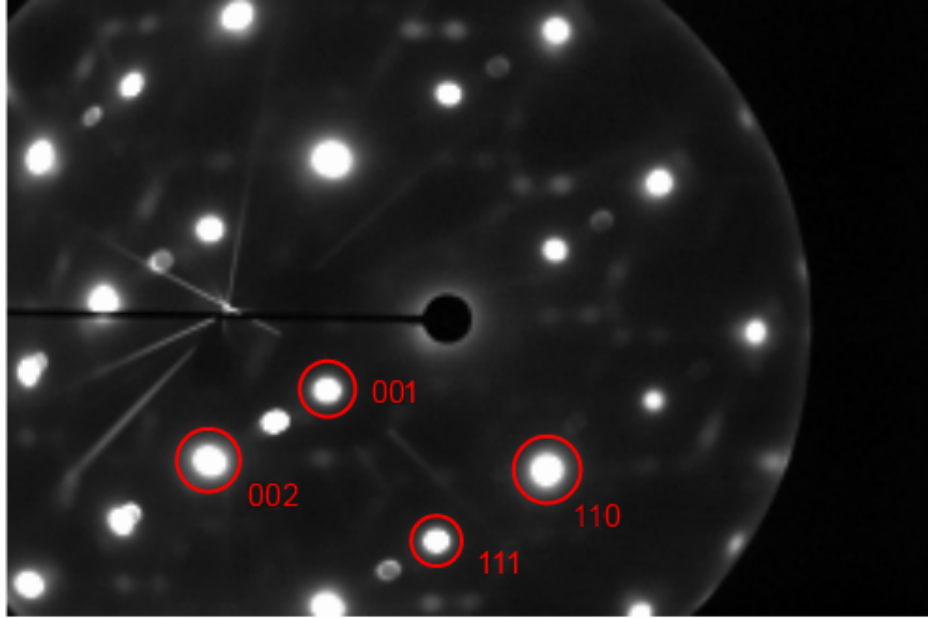


Figure 90: Microdiffraction pattern summed from only the FeRh layer in a FIB-prepared Cr-capped sample. When compared to a standard selected area diffraction pattern of an FeRh film, there are many extra diffraction spots visible. The locations of some standard CsCl FeRh spots are highlighted. It is important to note that, while at room temperature, the heating experiments performed on FIB-prepared cross-sections suggest that this is not in the AFM phase.

7.4 Plan View Magnetic Imaging

Lorentz microscopy experiments on a plan view sample (FeRh with a Cr cap) were performed using a JEOL ARM 200F. Initially, the sample was heated to 200 °C (i.e. far into the FM phase) then fully magnetised by tilting the sample into the objective lens and increasing the lens current. The sample was then tilted in the opposite direction and partially magnetised to create multiple FM domains with different orientations. At this point various magnetic domains could be seen in both standard Fresnel images (with white lines signifying the location of domain walls) and DPC images

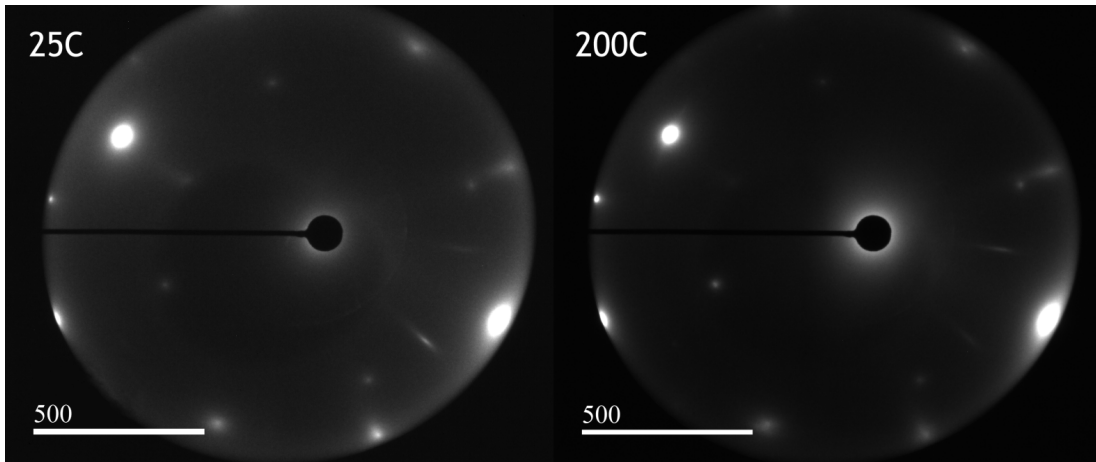


Figure 91: Selected area diffraction patterns of a plan-view FeRh film with a W cap below the transition temperature at 25 °C (AFM phase) and above the transition temperature at 200 °C (FM phase). There is no obvious visible change between the two aside from a slight rotation that is probably due to sample drift rather than any change in crystal structure.

(with different colours showing the direction of domain magnetisation), as seen in figures 92a and b. Figure 92c and d also provides a comparison showing the film brought to saturation magnetisation and a typical diffraction pattern obtained from this area. The existence of domain walls is no longer visible although there is contrast throughout the sample that does not change with magnetisation. This is potentially due to defects or grains in the FeRh crystal structure or more likely because of various crystallite grains within the Cr layer with slightly different orientations, which are also visible in cross-section. The diffraction pattern shows an ordered crystal structure and the large changes in contrast, if a result of disorder in the FeRh, would make the diffraction pattern appear more amorphous in nature. The Cr capping layer is only 5 nm thick so diffraction spots would not be very strong here. The size of the FM domains may also be measured here and compared to literature data. The domain size varies significantly within this area, with values between 0.4 μm to 1.2 μm . PEEM measurements find the domain size to be around 1.2 μm ⁵². The discrepancy

between these values may be due to the small region sampled in the TEM relative to a larger sample.

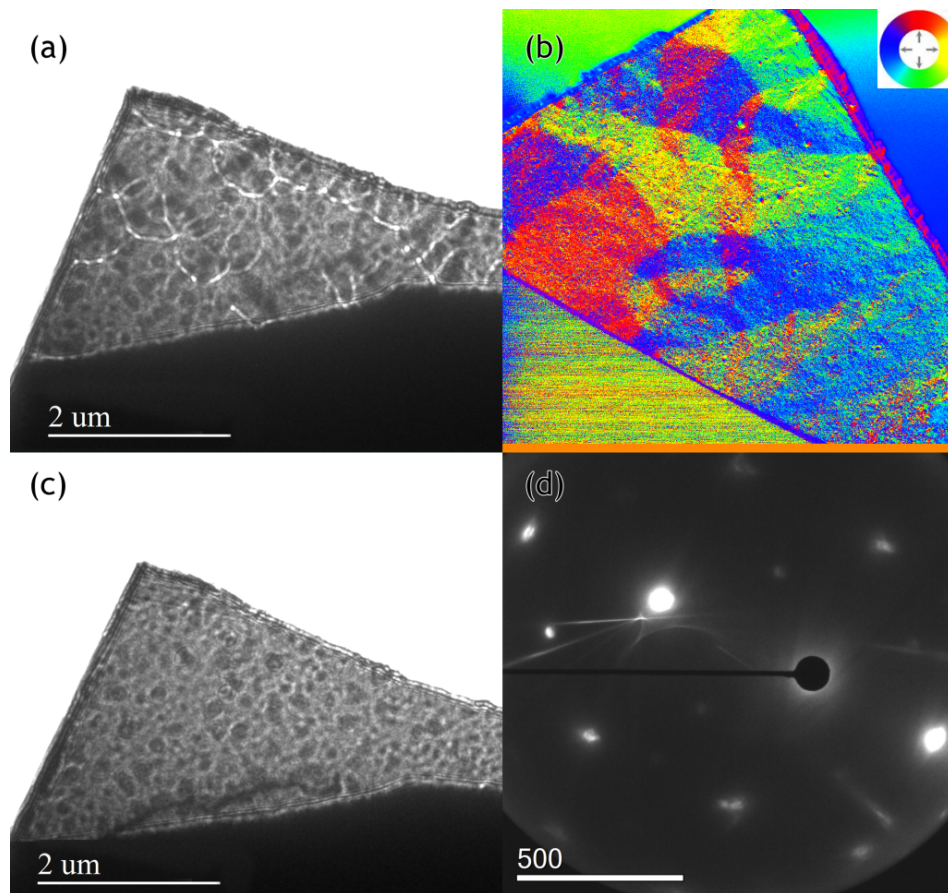


Figure 92: Various TEM images of a) a Fresnel image showing the existence of magnetic domains. The lines of bright and dark contrast corresponds with ferromagnetic domain walls. b) a DPC image again showing magnetic domains, instead imaging them directly with colour showing the direction of magnetisation. c) a Fresnel image with the sample brought to saturation magnetisation. Magnetic contrast from the domain walls is no longer visible but there is still a lot of contrast that appears in both this image and in 92a, potentially due to defects or granularity of the crystal. d) a diffraction pattern of the same area. The lack of evidence of polycrystalline or amorphous signal here suggests that the contrast is due to grains in the Cr capping layer.

By cooling down from 200 °C the sample was taken into the AFM phase to observe the disappearance of the FM domains. Initially this was performed using Fresnel imaging. Figure 93 shows the change seen in the Fresnel imaging mode as the sample is cooled. As the sample enters the phase transition, more domain wall contrast with a decreased intensity begin to appear throughout the film. Eventually the contrast initially visible at 200 °C begins to disappear with the extra contrast remaining.. Once the sample passes through the transition this contrast disappears and the film is left in what is expected to be the AFM state. The size of the domains in the middle of the transition are measured to be between $\sim 0.1-0.3 \mu\text{m}$.

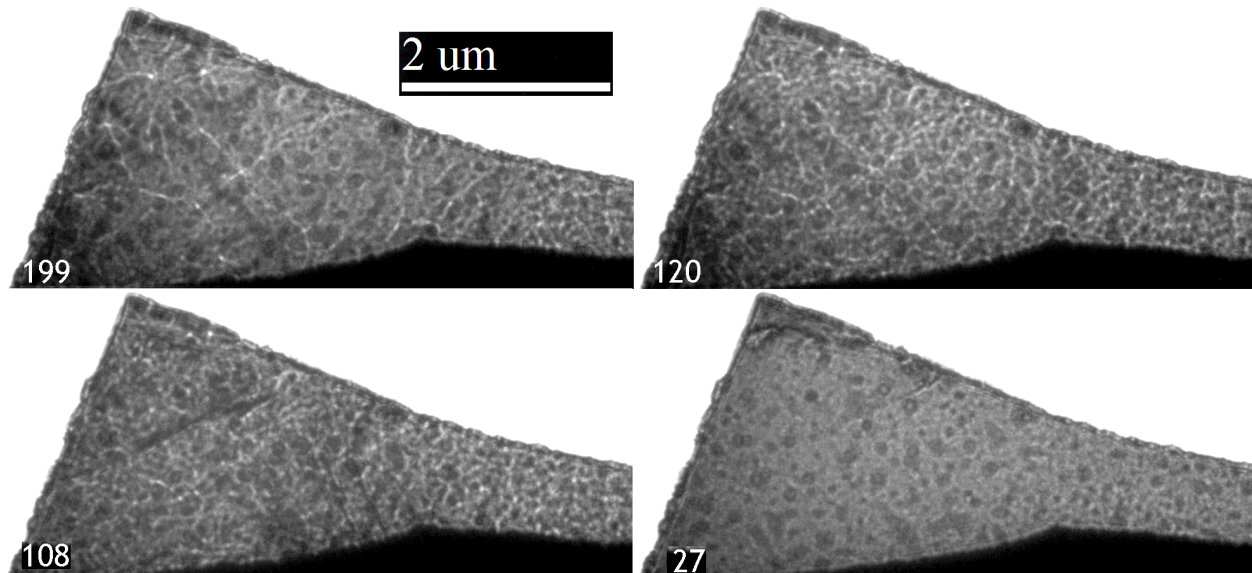


Figure 93: A series of Fresnel images observing the change in domain wall signal during cooling at (a) 199 °C (b) 120 °C (c) 108 °C (d) 27 °C. At 199 °C the sample is in the FM phase and domain walls are visible throughout the sample. In the middle of the phase transition at 120 °C more contrast is visible, suggesting a higher density of domains. Cooling further to 108 °C the domain walls are still visible but have a lower intensity. Finally at 27 °C the sample is in the AFM phase and no domain wall contrast is visible.

The experiment was repeated instead using the DPC detector to observe the change in FM signal.

Figure 94 shows data in a similar fashion to the Fresnel images. In the high temperature FM phase at 200 °C the domains appear as expected with strong FM signal throughout. Upon cooling, the domains still exist in their original locations but appear less well-defined and are speckled. As the sample is cooled further towards the FM phase the speckling is much more prominent with some evidence of the original domain locations showing, but without a reference of FM domains in figure 94 it is hard to recognise them. Finally in the expected AFM phase there are no FM domains and only noise.

As the FeRh phase transition is first order in nature, a phase coexistence through the transition is expected. This has been seen before in XPEEM experiments with the presence of FM and non-FM signal alongside each other. The DPC and Fresnel images strongly suggest that a domain coexistence is visible in the middle of the FM-AFM transition. The changes in both data sets is best explained by the loss of FM domains (and could be explained by the presence of the AFM phase) in the middle of the film with the areas closer to the interfaces remaining FM. As the sample is cooled these FM domains will slowly disappear until the sample is left completely in the AFM phase. As XPEEM is surface-sensitive, changes in the transition occurring beyond the top of the film, such as the potential effect seen here, cannot be seen.

7.5 Cross-Sectional Magnetic Imaging

Magnetic DPC measurements on a FIB-prepared sample (FeRh with a Cr cap) were performed using a JEOL ARM 200F. Initially, the sample was heated to 200°C (i.e. far into the FM phase) then magnetised by tilting the sample into the objective lens and increasing the lens current. Once magnetised a domain wall could be clearly seen using both conventional Lorentz microscopy and magnetic DPC, as seen in figure 95. This initially showed that the FM phase could be induced and imaged. However, upon cooling back to room temperature the FM phase still persisted and could not be removed. When combined with results found from strain heating experiments in FIB

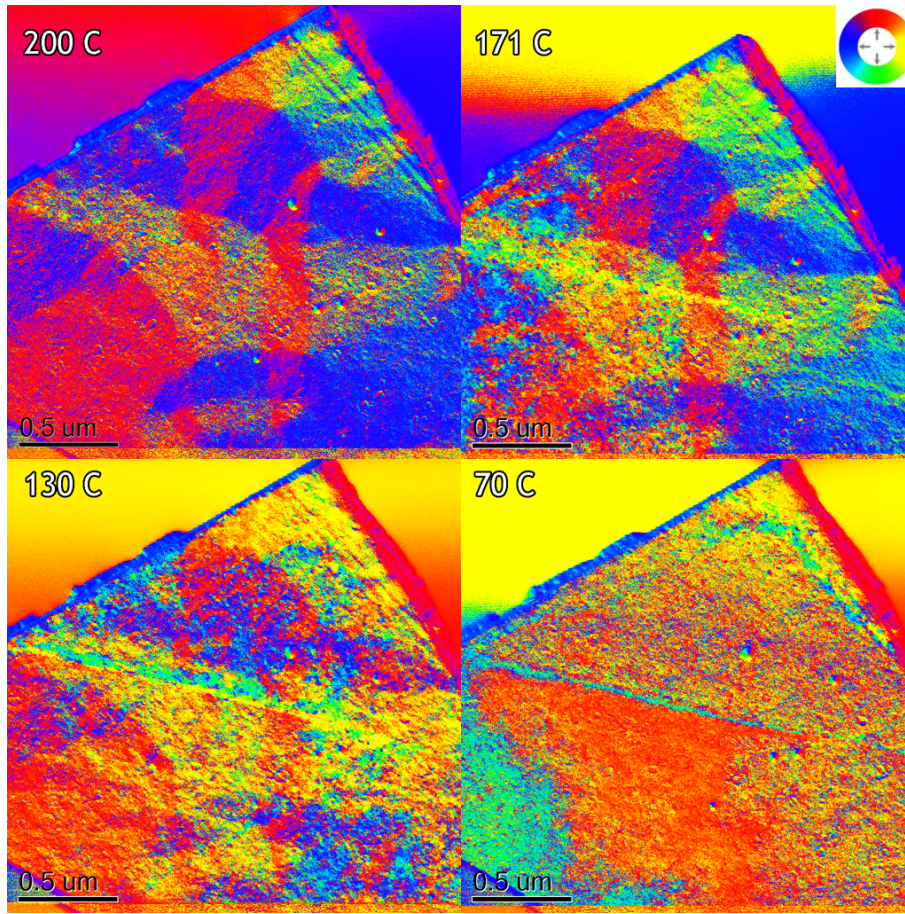


Figure 94: A series of DPC images observing the change in magnetic signal as the sample cools at (a) 200 °C (b) 171 °C (c) 130 °C (d) 70 °C. (a) Within the FM phase, the FM domains are clearly visible with many large, single-coloured areas. (b) As the sample is cooled, the domains are less well-defined and appear speckled in nature. (c) Within a reference in a or b, the location of the domains is much harder to ascertain. The original domains still exist but the speckle pattern is much more prominent. (d) In the AFM phase there are no longer any clearly defined ferromagnetic domains as expected.

sections, it seems likely that the sample transition is significantly affected by the preparation method used.

The results obtained suggest that the focused ion beam preparation method is causing damage

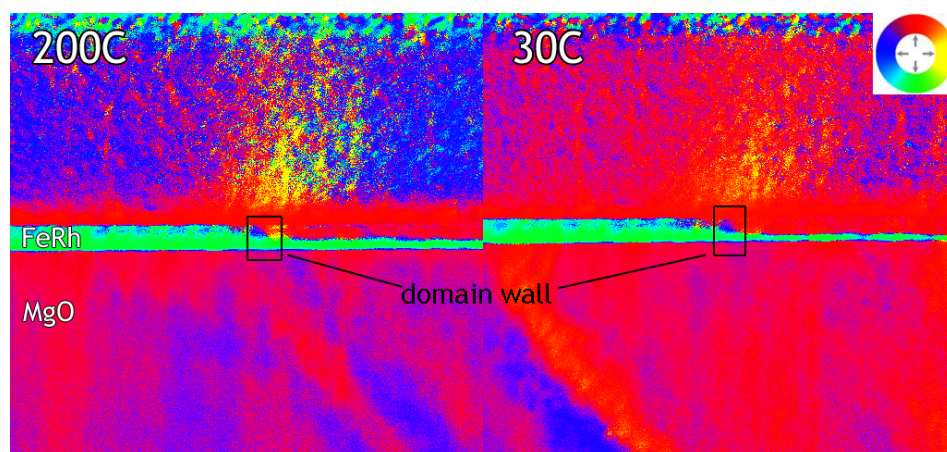


Figure 95: DPC images taken in the nominal FM (200 °C) and AFM (30 °C) phases for a FIB-prepared FeRh cross-section. It can be seen even deep within the AFM phase (~ 90 °C below the transition temperature) the domains still exist unchanged from the image taken above the transition.

to the sample and, as a result, affecting the phase transition by either destroying it completely or broadening the hysteresis. A FIB has been used as a means to intentionally damage the crystal structure and lower the transition temperature⁷⁷ and it is known that the ion beam causes amorphisation on both surfaces of the lamella^{135,136}. The creation of an amorphous layer could be enough to destroy the transition or at least lower the transition temperature below -169°C (the lowest achievable temperature available in the TEM with the sample holder used). As well, bending of lamella could cause unexpected changes in the transition due to changes in strain.

7.6 Chapter Summary

It has been found that the magnetostructural transition is very easily affected by changes in the sample form. Conventionally prepared samples show contrast changes in the bright field that correspond with strain fields (and therefore a lattice parameter change) while similar samples prepared by FIB show these results either once or never at all. Large shifts in the zone axis when moving

across the sample within both the FeRh film and MgO substrate suggest FIB sections bend significantly in the plane of the electron beam and could be related to the lack of consistent structural changes expected in these films. Lorentz microscopy experiments on similar FIB sections also found a lack of a phase transition, with the sample remaining ferromagnetic down deep into the AFM phase. FIB damage to the FeRh structure has been shown to reduce the transition temperature⁷⁷ but this has never been observed directly. Microdiffraction experiments also reveal extra ordering spots, but it is difficult to ascertain if these are caused by FIB damage or are a by-product of a martensitic transformation in the FM phase. It is important to note that changes in sample orientation may also affect the contrast observed in the sample as what appears to be changes due to strain may simply be drift in the microscope. The lack of change seen in FIB-prepared samples gives some evidence to suggest that orientation may not be a major issue. As well, large changes in temperature that are expected to be below the transition temperature do not see significant changes in contrast. However, the effect should not be ruled out completely.

Despite these issues, the strain field heating experiments in conventionally prepared cross sections successfully demonstrate the nucleation and growth of strain changes at the substrate and cap interfaces, with the lattice parameter change propagating through the structure. A large grain boundary within the FeRh also provided an interesting result regarding the transition, acting as a nucleation site similar to the interfaces. Experiments performed on the same sample in different area seem to find that there is a difference in the temperatures at which the contrast changes occur. The most likely explanations are either that there is a lag between the temperature recorded and the temperature of the observed area or that the thickness and location of the area affects the thermal conductance.

Plan view Lorentz microscopy allows for observation of the coexistence between AFM and FM domains. In the FM phase the domain size varies significantly but are typically found between ~ 0.4 - $1.2 \mu\text{m}$, which compares fairly closely to values of $1 \mu\text{m}$ ⁵³ and $1.2 \mu\text{m}$ ⁵² values in the literature.

Through the transition extra domain walls appear in Fresnel imaging and a speckling of the domains appears in DPC imaging which would suggest intermixing of phases out of plane of the sample when cooling into the AFM phase which has been suspected due to the effects of strain at the interfaces on FeRh but never directly observed. These extra domains are measured to be between $\sim 0.1-0.3 \mu\text{m}$ in diameter.

Observations of diffraction pattern change in plan view samples have found no obvious differences through the transition. The extra spots visible in FM-phase FIB cross-sections are not seen here in either phase which suggests that, if the ordering spots are a by-product of the FM phase, the spots are only visible observing in cross-section form. Otherwise, damage caused by the FIB is the only other explanation for these spots.

8 Conclusions and Future Work

The work detailed here demonstrates the power of transmission electron microscopy as a characterisation tool for the iron-rhodium system. Some TEM work on FeRh has studied nanoparticles or bulk materials but characterisation has never gone beyond basic structural observations and diffraction²⁶⁻²⁸. The ultimate goal has been to understand the AFM-FM transition further and to understand how epitaxial strained layers interact with FeRh and while it has made progress it has opened new questions about the system. This thesis has successfully characterised the changes in composition and interdiffusion at the FeRh interfaces, particularly investigating how applying an epitaxial capping layer affects local composition and confirmed that sputter-deposited growth is an effective method for creating FeRh films. Dynamic heating experiments across the transition gives evidence to suggest that there is a phase coexistence of FM domains with another phase (expected to be the AFM phase) within the FeRh phase transition where the regions at the interfaces potentially exist in a FM state whereas the middle of the film is AFM. Finally, there appears to be some evidence suggesting a martensitic phase transformation involved across the phase transition may be occurring that has not been previously documented but this is as yet not conclusive.

The main findings from this work are as follows:

- The roughness and thickness data acquired by TEM corresponds fairly well with bulk characterisation methods such as XRD and XRR. The imperfections in the values may be attributable to local variations in thickness and the effect of diffraction contrast making the interface harder to see clearly. The FeRh/MgO interface is extremely smooth while the FeRh/cap interface is slightly rougher with epitaxial growth for all layers. Strain contrast is visible at both interfaces although is more prominent at the W and Cr capping layers due to their larger lattice mismatches. These results show that sputter deposition and annealing is an effective method for growing FeRh layers.

- Focused ion beam is not a suitable method of cross-sectional sample preparation for FeRh if preserving the transition is important. Heating experiments find that the transition is destroyed in these cross-sections (whereas the transition still exists in conventionally-prepared cross-sections as well as plan view samples). If characterising chemical composition, the FIB is still a suitable method of achieving high resolution maps. The use of FIB systems to intentionally affect the transition fits with this results obtained here⁷⁷, although previous work has instead involved direct irradiation of regions of FeRh whereas the FIB prepared process uses glancing angles instead for thinning. The work by Aikoh also states that while lattice defects are introduced into the structure the XRD data shows that the the B2 ordering is retained. Bending of the lamella could also affect the transition as it will induce strain that could affect the phase transition.
- Analysis of the FeRh/MgO substrate interface using HAADF-STEM and STEM-EELS find the presence of a ~ 0.5 nm thick Fe-rich region (corresponding with 3 atomic layers). Previous work has shown that FeRh still exhibits a small ferromagnetic signal at the FeRh-MgO interface although this region is found to be ~ 10 nm thick²⁵. Ultrathin Fe layers on MgO are shown to still have a magnetic moment similar to bulk Fe¹⁵⁸ so this trilayer is likely to exhibit a FM signal but is unlikely to explain the FM signal alone. The reason for this could be a strain-induced composition change during sample growth and annealing. Fe has a smaller lattice parameter (2.87 Å) than FeRh (2.987 Å) and while the MgO atomic spacing along the [110] direction ($\frac{4.212}{\sqrt{2}} = 2.987$ Å) is very similar to FeRh a small change in composition may be energetically favourable.
- While growing FeRh epitaxially onto a substrate is widely documented as a means to growing FeRh thin films and affecting the transition, the concept of growing an epitaxial capping layer is new, so it is important to document the effect these layers have on the FeRh structurally and chemically. Using Cr and W layers due to their relatively similar lattice parameter,

HAADF-STEM and STEM-EELS of the interfaces between FeRh and these caps find significant interdiffusion of Fe into the Cr as well as a small Cr diffusion into the FeRh. No interdiffusion of any kind is seen at the FeRh/W interface. The interdiffusion across the FeRh/Cr interface makes it harder to control the transition effectively, making Cr a less suitable choice as a capping layer for increasing the transition temperature unless the interdiffusion can be controlled.

- The presence of laths or twins in the FeRh structure is an unexpected phenomenon which has not been previously documented either through TEM or through changes to the diffraction pattern. The twins are predominantly visible in FIB-prepared cross-sections but are also seen (albeit more rarely) in conventionally-prepared cross-sections as well. As previously discussed, ion beam irradiation has been shown to retain the CsCl structure of FeRh⁷⁷ so the effect likely cannot be explained purely by the FIB or the sample preparation process in general. Microdiffraction patterns of an FeRh cross-section prepared by FIB finds extra ordering spots. As FIB sections do not exhibit AFM order even at low temperatures, this diffraction pattern is expected to be associated with the FM phase. Room temperature SAED patterns do not see any extra ordering spots. Laths are generally associated with martensitic phase transitions, and the lattice volume increase of FeRh may also have a martensitic transformation associated. Similar magnetostructural phase transitions documented in manganese-gold and nickel-titanium alloys show a bcc to body centred tetragonal (bct) martensitic transition when cooling into an AFM phase at 500 K³³ for MnAu and a B2 to B19' change in TiNi³⁴. The MnAu instead exhibits a second order phase transformation and the martensitic transformation appears inverse to the FeRh transition, i.e. the martensitic phase (bct) appears on cooling instead of heating. The transformation for TiNi is first order like FeRh. The twin angle is measured at 45° when looking down the [110] plane, which would suggest a twin direction of (111). This again matches with the twin planes seen in MnAu and TiNi suggesting

a similar type of phase transition. Before this can be confirmed a comparison of diffraction pattern change across the transition in a conventionally-prepared cross-section must be performed. Combined with HRTEM or HAADF-STEM imaging above and below the transition the presence of twins can be confirmed. However, it is important to note that martensitic transformations are typically seen upon cooling rather than heating, which appears contradictory to the effects seen here.

- Strain heating experiments on conventionally prepared FeRh cross-sections clearly show the effect of epitaxial strain on the FeRh transition, providing points of nucleation. Grain boundaries also provide similar nucleation points to start the phase transition. The appearance of FM order in the AFM phase at interfaces²⁵ combined with the phase coexistence in the middle of the phase transition^{52,102} leads to the conclusion that the transition change will begin at the interfaces.
- Plan view observations of diffraction pattern change upon heating find no qualitative change of the pattern through the transition. This fits with X-ray measurements taken on bulk FeRh films¹⁰².
- Lorentz microscopy of a plan-view film allows for measurements of ferromagnetic domain size. The size varies significantly between ~ 0.4 - $1.2 \mu\text{m}$. Previous domain size measurements find the value to be $\sim 1 \mu\text{m}$ ^{52,53}. The discrepancy could be due to the small area observed as well as restriction due to imaging close to the edge of the sample but the larger values for domain size correlate with the literature values.
- Observation of the domain structure dynamics through the phase transition find contrast that may be attributed to extra domain walls with a lower intensity than the original walls in the FM phase (with a domain size measured at ~ 0.1 - $0.3 \mu\text{m}$) in the Fresnel imaging. In the DPC imaging there is a "speckling" of the domains that becomes stronger upon cooling until

the sample no longer appears ferromagnetic. This suggests that the FM phase could coexist with another phase, with multiple domains visible in the plane of the beam, i.e. one magnetic phase is located at the interface while another is located in the middle of the film. Considering the material, the potential second phase is expected to be the AFM phase nucleating during the cooling process. In comparison, PEEM measurements do not see the same effect, instead just the slow growth or decay of domains through the transition^{52,99}. However, PEEM is extremely surface sensitive so would not be able to observe a coexistence in the plane of the beam.

Future Work

- Most importantly the understanding of the possible martensitic transformation needs to be fully understood. Further experiments on conventionally-prepared cross-sections to characterise the diffraction pattern change across the transition as well as HRTEM and HAADF-STEM to see if there is a change in the presence of laths could confirm or deny the potential martensitic transition.
- While there is evidence to suggest that the phase transition has been observed here in cross-sectional FeRh, the lack of appropriate samples (due to breaking or because the samples were prepared by FIB) means that no Fresnel or DPC imaging experiments were successfully performed on cross-sections. It would be interesting to see how the phase change propagates through the sample and if it confirms the conclusions drawn from the cross-sectional strain heating experiments and plan view magnetic measurements.
- A combination of convergent beam electron diffraction and DPC imaging (non-magnetic, using the same principles but on a diffracted beam) could provide quantitative analysis of the strain in FeRh and its capping layers in both the AFM and FM phases and may also be used to

quantify strain changes through the transition.

- One of the later experiments performed using STEM-EELS found an apparent change in composition of the FeRh (figure 79 on page 125). While this effect was only seen in one sample, it would be interesting to find if this is an anomaly or if it exists elsewhere and determine if there is any effect on the local phase transition/strain.
- The existence of latent FM signal at the FeRh interfaces has been determined from bulk magnetic measurements such as polarised neutron reflectometry but has not been observed directly, although the existence of a small Fe-rich region has been found along the same interface. The magnetisation of these regions is extremely low relative to the full FM signal but it could be interesting to see this effect in the AFM phase.
- Much of the work documented here has involved TEM characterisation. Apart from one XPS data set, no other experiments were run (primarily due to the breaking of samples and the availability of equipment). Further XPS experiments and secondary ion mass spectrometry (SIMS) would provide complementary information to confirm the chemical changes seen here. SIMS would be an especially useful technique as it is a continuous measurement as opposed to the measurement of discrete layers via etching seen in XPS.

References

- [1] K Hermann. *Crystallography and Surface Structure: An Introduction for Surface Scientists and Nanoscientists*. 2011.
- [2] Rossler O. Madelung, O. and M. Schul' *II-VI and I-VII Compounds; Semimagnetic Compounds*. Springer Berlin Heidelberg, 1999.
- [3] L. J. Swartzendruber. The FeRh (Iron-Rhodium) system. *Bulletin of Alloy Phase Diagrams*, 5(5):456–462, October 1984.
- [4] Jordi Marcos, Lluís Mañosa, Antoni Planes, Fèlix Casanova, Xavier Batlle, and Amílcar Labarta. Multiscale origin of the magnetocaloric effect in Ni-Mn-Ga shape-memory alloys. *Physical Review B*, 68(9):094401, September 2003.
- [5] V. V. Khovailo, V. Novosad, T. Takagi, D. a. Filippov, R. Z. Levitin, and a. N. Vasilev. Magnetic properties and magnetostructural phase transitions in Ni_{2+x}Mn_{1-x}Ga shape memory alloys. 19:7, May 2004.
- [6] Roundy s. Wright K. and Evans J. W. Steingart, D. Micropower materials development for wireless sensor networks,. *Materials Research Society Bulletin*, 33:408–409, 2008.
- [7] VK Pecharsky and KA Gschneidner Jr. Magnetocaloric effect and magnetic refrigeration. *Journal of Magnetism and Magnetic . . .*, 200(January):44–56, 1999.
- [8] JS Kouvel. Unusual nature of the abrupt magnetic transition in FeRh and its pseudobinary variants. *Journal of Applied Physics*, 37(3):1257–1258, 1966.
- [9] Kadomtseva A. M. Levitin Ponyatovskii R. Z. E. G. Zakharov, A. I. Magnetic and magnetoelastic properties of a metamagnetic fe-rh alloy. *Journal of Experimental and Theoretical Physics*, 46:1348–1353, 1964.

- [10] M. Chattopadhyay, S. Roy, A. Nigam, K. Sokhey, and P. Chaddah. Metastability and giant relaxation across the ferromagnetic to antiferromagnetic transition in $\text{Ce}(\text{Fe}_{0.96}\text{Ru}_{0.04})_2$. *Physical Review B*, 68(17):1–8, November 2003.
- [11] S. Roy, G. Perkins, M. Chattopadhyay, A. Nigam, K. Sokhey, P. Chaddah, A. Caplin, and L. Cohen. First Order Magnetic Transition in Doped CeFe_2 Alloys: Phase Coexistence and Metastability. *Physical Review Letters*, 92(14):14–17, April 2004.
- [12] M. Chattopadhyay, S. Roy, and P. Chaddah. Kinetic arrest of the first-order ferromagnetic-to-antiferromagnetic transition in $\text{Ce}(\text{Fe}_{0.96}\text{Ru}_{0.04})_2$: Formation of a magnetic glass. *Physical Review B*, 72(18):15–18, November 2005.
- [13] Jan-Ulrich Thiele, Thomas Hauet, and Olav Hellwig. Design of CoPd multilayer system with antiferromagnetic-to-ferromagnetic phase transition. *Applied Physics Letters*, 92(24):242502, 2008.
- [14] A. J. Heeger. Pressure dependence of the ferri first-order phase transition. *Journal of Applied Physics*, 41(11):4751–4752, 1970.
- [15] JB McKinnon, D Melville, and EW Lee. The antiferromagnetic-ferromagnetic transition in iron-rhodium alloys. *Journal of Physics C: Solid*, 46, 1970.
- [16] N Baranov. Electrical resistivity and magnetic phase transitions in modified FeRh compounds. *Journal of Alloys and Compounds*, 219(1-2):139–148, March 1995.
- [17] Paul H. L. Walter. Exchange Inversion in Ternary Modifications of Iron Rhodium. *Journal of Applied Physics*, 35(3):938, 1964.
- [18] D. Weller and a. Moser. Thermal effect limits in ultrahigh-density magnetic recording. *IEEE Transactions on Magnetics*, 35(6):4423–4439, 1999.

- [19] Jan-Ulrich Thiele, Stefan Maat, and Eric E. Fullerton. FeRh/FePt exchange spring films for thermally assisted magnetic recording media. *Applied Physics Letters*, 82(17):2859, 2003.
- [20] LO Chua. Memristor-the missing circuit element. *Circuit Theory, IEEE Transactions on, C*, 1971.
- [21] Dmitri B Strukov, Gregory S Snider, Duncan R Stewart, and R Stanley Williams. The missing memristor found. *Nature*, 453(7191):80–3, May 2008.
- [22] X Marti, I Fina, C Frontera, Jian Liu, P Wadley, Q He, R J Paull, J D Clarkson, J Kudrnovský, I Turek, J Kuneš, D Yi, J-H Chu, C T Nelson, L You, E Arenholz, S Salahuddin, J Fontcuberta, T Jungwirth, and R Ramesh. Room-temperature antiferromagnetic memory resistor. *Nature materials*, 13(4):367–74, April 2014.
- [23] Jan-Ulrich Thiele, Matthias Buess, and Christian H. Back. Spin dynamics of the antiferromagnetic-to-ferromagnetic phase transition in FeRh on a sub-picosecond time scale. *Applied Physics Letters*, 85(14):2857, 2004.
- [24] Ganping Ju, Julius Hohlfeld, Bastiaan Bergman, René van de Veerdonk, Oleg Mryasov, Jai-Young Kim, Xiaowei Wu, Dieter Weller, and Bert Koopmans. Ultrafast Generation of Ferromagnetic Order via a Laser-Induced Phase Transformation in FeRh Thin Films. *Physical Review Letters*, 93(19):1–4, November 2004.
- [25] R. Fan, C. Kinane, T. Charlton, R. Dorner, M. Ali, M. de Vries, R. Brydson, C. Marrows, B. Hickey, D. Arena, B. Tanner, G. Nisbet, and S. Langridge. Ferromagnetism at the interfaces of antiferromagnetic FeRh epilayers. *Physical Review B*, 82(18):2–6, November 2010.
- [26] a. R. Yavari, E. Navarro, H. Mori, H. Yasuda, a. Hernando, and W. J. Botta F. On the B2 fcc transformation of FeRh during deformation. *Philosophical Magazine A*, 80(8):1779–1793, August 2000.

- [27] Shishou Kang. Synthesis and phase transition of self-assembled FePd and FePdPt nanoparticles. *Journal of Applied Physics*, 95(11):6744, 2004.
- [28] Hnin Yu Yu Ko, Takao Suzuki, Nguyen T. Nam, Nguyen N. Phuoc, Jiangwei Cao, and Yoshihiko Hirotsu. Magnetic and structural characterizations on nanoparticles of FePt, FeRh and their composites. *Journal of Magnetism and Magnetic Materials*, 320(22):3120–3123, November 2008.
- [29] D. C. Mattis. *The Theory of Magnetism Made Simple*. World Scientific, 2006.
- [30] A. Aharoni. *Introduction to the Theory of Ferromagnetism*. Oxford University Press, 2000.
- [31] D. A. Porter and K. E. Easterling. *Phase Transformation in Metals and Alloys*. Van Nostrand Reinhold Berkshire, 1983.
- [32] Kurt Binder. Theory of first-order phase transitions. *Reports on progress in physics*, 50:783, 1987.
- [33] Z. Nishiyama. *Martensitic Transformation*. Martensitic Transformation. Elsevier Science, 2012.
- [34] K. Otsuka and X. Ren. Physical metallurgy of TiNi-based shape memory alloys. *Progress in Materials Science*, 50(5):511–678, July 2005.
- [35] C. Liu, H. Qin, and P. T. Mather. Review of progress in shape-memory polymers. *Journal of Materials Chemistry*, 17:1543, 2007.
- [36] N. B. Morgan. Medical shape memory alloy applications - The market and its products. *Materials Science and Engineering A*, 378:16–23, 2004.
- [37] Marchon Eyewear Inc. Flexon eyewear: <http://www.marchon.com/html/flexon.asp>.

- [38] Paulo Rangel Rios and José Roberto Costa Guimarães. Formal analysis of isothermal martensite spread. *Materials Research*, 11(1):103–108, 2008.
- [39] CP Bean and DS Rodbell. Magnetic disorder as a first-order phase transformation. *Physical Review*, 126(1):104–115, 1962.
- [40] S. J. Murray, M. a. Marioni, a. M. Kukla, J. Robinson, R. C. OHandley, and S. M. Allen. Large field induced strain in single crystalline NiMnGa ferromagnetic shape memory alloy. *Journal of Applied Physics*, 87(9):5774, 2000.
- [41] Ajaya K. Nayak, K. G. Suresh, and a. K. Nigam. Metastability of magneto-structural transition revealed by sweep rate dependence of magnetization in Ni₄₅Co₅Mn₃₈Sb₁₂ Heusler alloy. *Journal of Applied Physics*, 109(7):07A906, 2011.
- [42] V K Sharma, J D Moore, M K Chattopadhyay, Kelly Morrison, L F Cohen, and S B Roy. A scanning Hall probe imaging study of the field induced martensite-austenite phase transition in Ni₅₀Mn₃₄In₁₆ alloy. *Journal of physics. Condensed matter : an Institute of Physics journal*, 22(1):016008, January 2010.
- [43] Fallot M. Les alliages du fer avec les metaux de la famille du platine. *Annales de Physique*, 10:291–332, 1938.
- [44] VL Moruzzi and PM Marcus. Antiferromagnetic-ferromagnetic transition in FeRh. *Physical Review B*, 46(5):2864, 1992.
- [45] J. S. Kouvel and C. C. Hartelius. Anomalous Magnetic Moments and Transformations in the Ordered Alloy FeRh. *Journal of Applied Physics*, 33(3):1343, 1962.
- [46] L Muldower. Antiferromagnetic-ferromagnetic transformation in FeRh. *The Journal of Chemical Physics*, 1961.

- [47] MA Khan. Band theory of nonmagnetic and magnetic iron-rhodium alloy. *Journal of Physics F: Metal Physics*, 9:457, 1979.
- [48] L. Zsoldos. Lattice parameter change of ferh alloys due to antiferromagnetic-ferromagnetic transformation. *physica status solidi (b)*, 20(1):K25–K28, 1967.
- [49] G. Shirane, CW Chen, PA Flinn, and R. Nathans. Mössbauer Study of Hyperfine Fields and Isomer Shifts in the Fe-Rh Alloys. *Physical Review*, 131(1):183, 1963.
- [50] G. Shirane, R. Nathans, and CW Chen. Magnetic moments and unpaired spin densities in the Fe-Rh alloys. *Phys. Rev*, 134:A1547, 1964.
- [51] VL Moruzzi and PM Marcus. Antiferromagnetic-ferromagnetic transition in FeRh. *Physical Review B*, 46(5), 1992.
- [52] CJ Kinane, M Loving, and MA de Vries. Observation of a temperature dependent asymmetry in the domain structure of a Pd doped FeRh epilayer. *arXiv preprint arXiv: . . .*, pages 1–10, 2014.
- [53] S. O. Mariager, L. Le Guyader, M. Buzzi, G. Ingold, and C. Quitmann. Imaging the antiferromagnetic to ferromagnetic first order phase transition of FeRh. page 19, January 2013.
- [54] J. W. Kim, P. J. Ryan, Y. Ding, L. H. Lewis, M. Ali, C. J. Kinane, B. J. Hickey, C. H. Marrows, and D. a. Arena. Surface influenced magnetostructural transition in FeRh films. *Applied Physics Letters*, 95(22):222515, 2009.
- [55] Chantal Le Graët, Mark a de Vries, Mathew McLaren, Richard M D Brydson, Melissa Loving, Don Heiman, Laura H Lewis, and Christopher H Marrows. Sputter growth and characterization of metamagnetic B2-ordered FeRh epilayers. *Journal of visualized experiments : JoVE*, (80):1–8, January 2013.

- [56] Wei Lu, Ping Huang, Zhe Chen, Chenchong He, Yuxin Wang, and Biao Yan. Magnetization studies of first-order magnetostructural phase transition in polycrystalline FeRh thin films. *Journal of Physics D: Applied Physics*, 45(43):435001, October 2012.
- [57] J.-S. Lee, E. Vescovo, L. Plucinski, C. M. Schneider, and C.-C. Kao. Electronic structure and magnetic properties of epitaxial FeRh(001) ultrathin films on W(100). *Physical Review B*, 82(22):224410, December 2010.
- [58] G. C. Han, J. J. Qiu, Q. J. Yap, P. Luo, D. E. Laughlin, J. G. Zhu, T. Kanbe, and T. Shige. Magnetic stability of ultrathin FeRh films. *Journal of Applied Physics*, 113(17):17C107, 2013.
- [59] Y Ohtani. Features of broad magnetic transition in FeRh thin film. *Journal of Magnetism and Magnetic Materials*, 131(3):339–344, March 1994.
- [60] S. Hashi, S. Yanase, Y. Okazaki, and M. Inoue. A Large Thermal Elasticity of the Ordered FeRh Alloy Film With Sharp Magnetic Transition. *IEEE Transactions on Magnetics*, 40(4):2784–2786, July 2004.
- [61] S. Lounis, M. Benakki, and C. Demangeat. Ferromagnetic stabilization of ordered B2 FeRh thin films. *Physical Review B*, 67(9):1–5, March 2003.
- [62] T. J. Swoboda, W. H. Cloud, T. A. Bither, M. S. Sadler, and H. S. Jarrett. Evidence for an antiferromagnetic-ferrimagnetic transition in cr-modified mn_2sb . *Phys. Rev. Lett.*, 4:509–511, May 1960.
- [63] RW De Blois and DS Rodbell. Magnetic First-Order Phase Transition in Single-Crystal MnAs. *Physical Review*, 130(4):1347–1360, 1963.
- [64] L. Morellon, J. Blasco, P. Algarabel, and M. Ibarra. Nature of the first-order antiferromagnetic-ferromagnetic transition in the Ge-rich magnetocaloric compounds $\text{Gd}_5(\text{SixGe}_{1-x})_4$. *Physical Review B*, 62(2):1022–1026, July 2000.

- [65] Kyongha Kang, a. R. Moodenbaugh, and L. H. Lewis. MnBi nanostructures: Size dependence of magnetostructural transition and matrix templating. *Applied Physics Letters*, 90(15):153112, 2007.
- [66] Pallavi Kushwaha, Archana Lakhani, R. Rawat, and P. Chaddah. Low-temperature study of field-induced antiferromagnetic-ferromagnetic transition in Pd-doped Fe-Rh. *Physical Review B*, 80(17):1–7, November 2009.
- [67] J Van Driel, R Coehoorn, G J Strijkers, F R De Boer, E Bru, and I Introduction. Compositional dependence of the giant magnetoresistance in Fe x Rh 1 x thin films. *Journal of Applied Physics*, 85(2):1026–1036, 1999.
- [68] Dhishan Kande, David Laughlin, and Jian-Gang Zhu. Origin of room temperature ferromagnetic moment in Rh-rich [Rh/Fe] multilayer thin films. *Journal of Applied Physics*, 107(9):09E318, 2010.
- [69] N.T. Nam and T. Suzuki. Effect of Pt Doping on the Structure, Magnetic, and Magneto-Optical Properties of Ordered FeRh-Pt Thin Films. *IEEE Transactions on Magnetics*, 45(6):2716–2719, June 2009.
- [70] CJ Schinkel, R. Hartog, and F. Hochstenbach. On the magnetic and electrical properties of nearly equiatomic ordered FeRh alloys. *Journal of Physics F: Metal Physics*, 4:1412, 1974.
- [71] P Tu, AJ Heeger, JS Kouvel, and JB Comly. Mechanism for the First-Order Magnetic Transition in the FeRh System. *Journal of Applied Physics*, 40(3):1368, 1969.
- [72] Wei Lu, Biao Yan, and Takao Suzuki. Magnetic phase transition and magneto-optical properties in epitaxial FeRh_{0.95}Pt_{0.05} (001) single-crystal thin film. *Scripta Materialia*, 61(9):851–854, November 2009.

- [73] M Fukuzumi, Y Chimi, N Ishikawa, F Ono, S Komatsu, and A Iwase. Swift heavy ion induced magnetic phase transition of FeRh alloy. *Nuclear Instruments and Methods in Physics Research Section B: Beam Interactions with Materials and Atoms*, 230(1-4):269–273, April 2005.
- [74] M Fukuzumi, Y Chimi, N Ishikawa, M Suzuki, M Takagaki, J Mizuki, F Ono, R Neumann, and A Iwase. Effects of swift heavy ion irradiation on magnetic properties of FeRh alloy. *Nuclear Instruments and Methods in Physics Research Section B: Beam Interactions with Materials and Atoms*, 245(1):161–165, April 2006.
- [75] S. Kosugi, Nao Fujita, T. Matsui, F. Hori, Y. Saitoh, N. Ishikawa, Y. Okamoto, and A. Iwase. Effect of high temperature annealing on ferromagnetism induced by energetic ion irradiation in FeRh alloy. *Nuclear Instruments and Methods in Physics Research Section B: Beam Interactions with Materials and Atoms*, 269(9):869–872, May 2011.
- [76] Nao. Fujita, S. Kosugi, Y. Saitoh, Y. Kaneta, K. Kume, T. Batchuluun, N. Ishikawa, T. Matsui, and A. Iwase. Magnetic states controlled by energetic ion irradiation in FeRh thin films. *Journal of Applied Physics*, 107(9):09E302, 2010.
- [77] K. Aikoh, S. Kosugi, T. Matsui, and A. Iwase. Quantitative control of magnetic ordering in FeRh thin films using 30 keV Ga ion irradiation from a focused ion beam system. *Journal of Applied Physics*, 109(7):07E311, 2011.
- [78] Atsushi Tohki, Kazuma Aikoh, Ryoichi Shinoda, Takuo Ohkochi, Masato Kotsugi, Tetsuya Nakamura, Toyohiko Kinoshita, Akihiro Iwase, and Toshiyuki Matsui. X-ray magnetic circular dichroism photoemission electron microscopy of focused ion beam-induced magnetic patterns on ironrhodium surfaces. *Nuclear Instruments and Methods in Physics Research Section B: Beam Interactions with Materials and Atoms*, 302:51–54, May 2013.

- [79] LI Vinokurova. Pressure effects on magnetic phase transitions in FeRh and FeRhIr alloys. *physica status solidi . . .*, 363, 1976.
- [80] K. Kameneva, Z. Arnolda, J. Kamaráda, and N.V. Baranovb. Pressure induced antiferromagnetism in (Fe_{1-x}Ni_x)₄₉Rh₅₁ alloys. *Journal of Alloys and Compounds*, 252:1–5, 1997.
- [81] L.I. Vinokurova, A.V. Vlasov, N.I. Kulikov, and M. Pardavi-Horváth. Pressure-induced antiferromagnetism in ferromagnetic Fe_{51.5}Rh_{48.5} alloy. *Journal of Magnetism and Magnetic Materials*, 25(2):201–206, December 1981.
- [82] S Maat, J.U. Thiele, and E.E. Fullerton. Temperature and field hysteresis of the antiferromagnetic-to-ferromagnetic phase transition in epitaxial FeRh films. *Physical Review B*, 72(21):214432, 2005.
- [83] C. Bordel, J. Juraszek, David W. Cooke, C. Baldasseroni, S. Mankovsky, J. Minár, H. Ebert, S. Moyerman, E. E. Fullerton, and F. Hellman. Fe Spin Reorientation across the Metamagnetic Transition in Strained FeRh Thin Films. *Physical Review Letters*, 109(11):117201, September 2012.
- [84] J. M. Lommel. Magnetic and Electrical Properties of FeRh Thin Films. *Journal of Applied Physics*, 37(3):1483, 1966.
- [85] J. M. Lommel. Role of Oxygen in Obtaining Complete Magnetic First-Order Transitions in FeRh Films. *Journal of Applied Physics*, 40(3):1466, 1969.
- [86] Jiangwei Cao, Nguyen T. Nam, Sho Inoue, Hnin Yu Yu Ko, Nguyen N. Phuoc, and Takao Suzuki. Magnetization behaviors for FeRh single crystal thin films. *Journal of Applied Physics*, 103(7):07F501, 2008.
- [87] Y. Ohtani and I. Hatakeyama. Antiferro-ferromagnetic transition and microstructural prop-

- erties in a sputter deposited FeRh thin film system. *Journal of Applied Physics*, 74(5):3328, 1993.
- [88] Ippei Suzuki, Takayoshi Koike, Mitsuru Itoh, Tomoyasu Taniyama, and Tetsuya Sato. Stability of ferromagnetic state of epitaxially grown ordered FeRh thin films. *Journal of Applied Physics*, 105(7):07E501, 2009.
- [89] G. C. Han, J. J. Qiu, Q. J. Yap, P. Luo, T. Kanbe, T. Shige, D. E. Laughlin, and J.-G. Zhu. Suppression of low-temperature ferromagnetic phase in ultrathin FeRh films. *Journal of Applied Physics*, 113(12):123909, 2013.
- [90] M Loving, F Jimenez-Villacorta, B Kaeswurm, D a Arena, C H Marrows, and L H Lewis. Structural evidence for stabilized ferromagnetism in epitaxial FeRh nanoislands. *Journal of Physics D: Applied Physics*, 46(16):162002, April 2013.
- [91] J.P. Ayoub, C. Gatel, C. Roucau, and M.J. Casanove. Structure and chemical order in FeRh nanolayers epitaxially grown on MgO(001). *Journal of Crystal Growth*, 314(1):336–340, January 2011.
- [92] B. Kaeswurm, F. Jimenez-Villacorta, S.P. Bennett, D. Heiman, and L.H. Lewis. Nanostructured FeRh in metallic and insulating films. *Journal of Magnetism and Magnetic Materials*, 354:284–289, March 2014.
- [93] S. Inoue, N.T. Nam, T. Suzuki, and Y. Hirotsu. Magnetic Properties of Nanocomposite Particles of FePt/FeRh. *IEEE Transactions on Magnetics*, 44(11):2780–2783, November 2008.
- [94] Hnin Yu Yu Ko, Takao Suzuki, Nguyen N. Phuoc, and Jiangwei Cao. Fabrication and characterization of FeRh nanoparticles. *Journal of Applied Physics*, 103(7):07D508, 2008.
- [95] Z. Jia, J. W. Harrell, and R. D. K. Misra. Synthesis and magnetic properties of self-assembled FeRh nanoparticles. *Applied Physics Letters*, 93(2):022504, 2008.

- [96] Hnin Yu Yu Ko and Takao Suzuki. Synthesis and magnetic properties of self-organized FeRh nanoparticles. *Journal of Applied Physics*, 101(9):09J103, 2007.
- [97] a. Hillion, a. Cavallin, S. Vlaic, a. Tamion, F. Tournus, G. Khadra, J. Dreiser, C. Piamonteze, F. Nolting, S. Rusponi, K. Sato, T. Konno, O. Proux, V. Dupuis, and H. Brune. Low Temperature Ferromagnetism in Chemically Ordered FeRh Nanocrystals. *Physical Review Letters*, 110(8):087207, February 2013.
- [98] C. Stamm, J.-U. Thiele, T. Kachel, I. Radu, P. Ramm, M. Kosuth, J. Minár, H. Ebert, H. Dürr, W. Eberhardt, and C. Back. Antiferromagnetic-ferromagnetic phase transition in FeRh probed by x-ray magnetic circular dichroism. *Physical Review B*, 77(18):3–7, May 2008.
- [99] C Baldasseroni, C Bordel, A X Gray, A M Kaiser, F Kronast, C M Schneider, C S Fadley, and F Hellman. Temperature-driven nucleation of ferromagnetic domains in FeRh thin films. 262401:1–5, 2012.
- [100] M. Manekar, C. Mukherjee, and S. B. Roy. Imaging of time evolution of the first-order magneto-structural transition in Fe-Rh alloy using magnetic force microscopy. *Europhysics Letters (EPL)*, 80(1):17004, October 2007.
- [101] Y. Yokoyama, M. Usukura, S. Yuasa, Y. Suzuki, H. Miyajima, and T. Katayama. MFM observation of magnetic phase transitions in ordered FeRh systems. *Journal of Magnetism and Magnetic Materials*, 177-181:181–182, January 1998.
- [102] M. a. de Vries, M. Loving, M. McLaren, R. M. D. Brydson, X. Liu, S. Langridge, L. H. Lewis, and C. H. Marrows. Asymmetric melting and freezing kinetics of the magnetostructural phase transition in B2-ordered FeRh epilayers. *Applied Physics Letters*, 104(23):232407, June 2014.
- [103] T Fukuda and T Kakeshita. Martensitic transformation in Pd doped FeRh exhibiting a metamagnetic transition. *Journal of Alloys and Compounds*, 2013.

- [104] Y. Feng, T. Fukuda, and T. Kakeshita. Temperature memory effect associated with a first order magnetic transition in FeRh. *Intermetallics*, 36:57–60, May 2013.
- [105] Yan Feng, Yong-hee Lee, Takashi Fukuda, and Tomoyuki Kakeshita. Time dependent nature of first order magnetostructural transition in FeRh. *Journal of Alloys and Compounds*, 538:5–7, October 2012.
- [106] E Beaurepaire, J Merle, A Daunois, and J Bigot. Ultrafast spin dynamics in ferromagnetic nickel. *Physical review letters*, 76(22):4250–4253, May 1996.
- [107] J Hohlfeld, E Matthias, R. Knorren, and KH Bennemann. Nonequilibrium magnetization dynamics of nickel. *Physical review letters*, 78(25):4861–4864, 1997.
- [108] F. Dalla Longa, J. T. Kohlhepp, W. J. M. de Jonge, and B. Koopmans. Resolving the genuine laser-induced ultrafast dynamics of exchange interaction in ferromagnet/antiferromagnet bilayers. *Physical Review B*, 81(9):1–5, March 2010.
- [109] C. Stanciu, F. Hansteen, a. Kimel, a. Kirilyuk, a. Tsukamoto, a. Itoh, and Th. Rasing. All-Optical Magnetic Recording with Circularly Polarized Light. *Physical Review Letters*, 99(4):047601, July 2007.
- [110] Bastiaan Bergman, Ganping Ju, Julius Hohlfeld, René van de Veerdonk, Jai-Young Kim, Xiaowei Wu, Dieter Weller, and Bert Koopmans. Identifying growth mechanisms for laser-induced magnetization in FeRh. *Physical Review B*, 73(6):1–4, February 2006.
- [111] I. Radu, C. Stamm, N. Pontius, T. Kachel, P. Ramm, J.-U. Thiele, H. a. Dürr, and C. H. Back. Laser-induced generation and quenching of magnetization on FeRh studied with time-resolved x-ray magnetic circular dichroism. *Physical Review B*, 81(10):1–5, March 2010.
- [112] C. Baldasseroni, G. K. Pálsson, C. Bordel, S. Valencia, a. a. Unal, F. Kronast, S. Nemsak, C. S. Fadley, J. a. Borchers, B. B. Maranville, and F. Hellman. Effect of capping material

- on interfacial ferromagnetism in FeRh thin films. *Journal of Applied Physics*, 115(4):043919, January 2014.
- [113] C. Kittel. Model of Exchange-Inversion Magnetization. *Physical Review*, 120(2):335–342, October 1960.
- [114] J. A. Ricodeau and D. Melville. Model of the antiferromagnetic-ferromagnetic transition in ferh alloys. *Journal of Physics F: Metal Physics*, 2:337, 1972.
- [115] D. Melville Richardson, M. J. and J. A. Ricodeau. Specific heat measurements on an ferh alloy. *Physics Letters A*, 46:153–154, 1973.
- [116] M. P. Annaorazov, S. a. Nikitin, a. L. Tyurin, K. a. Asatryan, and a. Kh. Dovletov. Anomalous high entropy change in FeRh alloy. *Journal of Applied Physics*, 79(3):1689, 1996.
- [117] J. Ivarsson, GR Pickett, and J. Tóth. The electronic heat capacity of nearly stoichiometric ordered FeRh alloys. *Physics Letters A*, 35(3):167–168, 1971.
- [118] M. Gruner, E. Hoffmann, and P. Entel. Instability of the rhodium magnetic moment as the origin of the metamagnetic phase transition in α -FeRh. *Physical Review B*, 67(6):1–10, February 2003.
- [119] R. Gu and V. Antropov. Dominance of the spin-wave contribution to the magnetic phase transition in FeRh. *Physical Review B*, 72(1):012403, July 2005.
- [120] J. B. Staunton, R. Banerjee, M. Dos Santos Dias, a. Deak, and L. Szunyogh. Fluctuating local moments, itinerant electrons, and the magnetocaloric effect: Compositional hypersensitivity of FeRh. *Physical Review B*, 89(5):054427, February 2014.
- [121] Leonid Sandratskii and Phivos Mavropoulos. Magnetic excitations and femtomagnetism of FeRh: A first-principles study. *Physical Review B*, 83(17):1–13, May 2011.

- [122] Joseph Barker and Roy W. Chantrell. Higher order exchange interactions leading to metamagnetism in FeRh. May 2014.
- [123] D. A. Thompson and J. S. Best. The future of magnetic data storage technology. *IBM Journal of Research and Development*, 44(3):311–322, may 2000.
- [124] Nguyen T. Nam, W. Lu, and T. Suzuki. Exchange bias of ferromagnetic/antiferromagnetic in FePt/FeRh bilayers. *Journal of Applied Physics*, 105(7):07D708, 2009.
- [125] T Goto. Growth of FeRh thin films and magnetic properties of FePt/FeRh bilayers. *Journal of Magnetism and Magnetic Materials*, 272-276:E791–E792, May 2004.
- [126] EE Fullerton, JS Jiang, and M Grimsditch. Exchange-spring behavior in epitaxial hard/soft magnetic bilayers. *Physical Review B*, 58(18):193–200, 1998.
- [127] A. R. Barron. Molecular beam epitaxy. <http://cnx.org/contents/0b2614e4-aa98-49c1-bf50-1db3ee3c5ecd@2>, cited in 2014.
- [128] Aachen University Physics Department. The reactive dc-magnetron sputtering process. <http://ia.physik.rwthachen.de/research/sputtering/www-sputter-eng.pdf>, cited in 2014.
- [129] S. Inoue and T. Suzuki. Magnetic Properties of Single-Crystalline FeRh Alloy Thin Films. *IEEE Transactions on Magnetics*, 44(11):2875–2878, November 2008.
- [130] B. E. Warren. *X-ray diffraction*. Reading, Mass: Addison-Wesley Pub. Co., 1969.
- [131] Takafumi Miyanaga, Tatsunori Itoga, Teiko Okazaki, and Kiyofumi Nitta. Local structural change under antiferro- and ferromagnetic transition in FeRh alloy. *Journal of Physics: Conference Series*, 190:012097, November 2009.
- [132] Chantal Le Graët, Mark a de Vries, Mathew McLaren, Richard M D Brydson, Melissa Loving, Don Heiman, Laura H Lewis, and Christopher H Marrows. Sputter growth and characteriza-

- tion of metamagnetic B2-ordered FeRh epilayers. *Journal of visualized experiments : JoVE*, (80):1–8, January 2013.
- [133] P. Spellward. *Cross-Sectional Kit Content and Use*. Gatan, 2003.
- [134] LA Giannuzzi and FA Stevie. A review of focused ion beam milling techniques for TEM specimen preparation. *Micron*, 30(3):197–204, 1999.
- [135] J P McCaffrey, M W Phaneuf, and L D Madsen. Surface damage formation during ion-beam thinning of samples for transmission electron microscopy. *Ultramicroscopy*, 87(3):97–104, April 2001.
- [136] N. I. Kato, Y. Kohno, and H. Saka. Side-wall damage in a transmission electron microscopy specimen of crystalline Si prepared by focused ion beam etching. *Journal of Vacuum Science & Technology A: Vacuum, Surfaces, and Films*, 17(4):1201, 1999.
- [137] L. Clement, R. Pantel, L. F. Tz. Kwakman, and J. L. Rouviere. Strain measurements by convergent-beam electron diffraction: The importance of stress relaxation in lamella preparations. *Applied Physics Letters*, 85(4):651, 2004.
- [138] JEOL. *JEOL 2000FX Handbook, Image acquired from:*
<http://www2.warwick.ac.uk/fac/sci/physics/current/postgraduate/regs/mpags/ex5/techniques/structural/ter>
- [139] D.B. William and C.B. Carter. *Transmission Electron Microscopy, 2nd ed. A Textbook for Materials Science*. New York: Springer Science+Business media, 2009.
- [140] Jingyue Liu. Scanning transmission electron microscopy and its application to the study of nanoparticles and nanoparticle systems. *Journal of electron microscopy*, 54(3):251–78, June 2005.
- [141] Peter D Nellist. Scanning Transmission Electron Microscopy. (i):91–116, 2011.

- [142] L Fitting, S Thiel, A Schmehl, J Mannhart, and D A Muller. Subtleties in ADF imaging and spatially resolved EELS : A case study of low-angle twist boundaries in SrTiO₃. 106:1053–1061, 2006.
- [143] R. F. Loane, E. J. Kirkland, and J. Silcox. Visibility of single heavy atoms on thin crystalline silicon in simulated annular dark-field STEM images. *Acta Crystallographica Section A Foundations of Crystallography*, 44(6):912–927, November 1988.
- [144] Zhiheng Yu. Study of strain fields at a-Si/c-Si interface. *Journal of Applied Physics*, 95(7):3362, 2004.
- [145] University of Cape Town. *EDX: Peaks and Background, image acquired from:* <http://emu.uct.ac.za/training/sem-school/edx-peaks-and-background/>.
- [146] RD Leapman and LA Grunes. Anomalous L₃ L₂ White-Line Ratios in the 3d Transition Metals. *Physical Review Letters*, 45(5):397–401, 1980.
- [147] C Colliex, T Manoubi, and C Ortiz. Electron-energy-loss-spectroscopy near-edge fine structures in the iron-oxygen system. *Physical Review B*, 44(20), 1991.
- [148] Krivanek O. L. Ahn, C. C. *EELS Atlas: A reference collection of electron energy loss spectra covering all stable elements*. Gatan, 1983.
- [149] Peter D. Nellist. Electron microscopy: Atomic resolution comes into phase. *Nature Physics*, 8(8):586–587, June 2012.
- [150] D.W. Ackland C.J. Kiely M. Watanabe, M. Kanno and D.B. Williams. The antiferromagnetic-ferromagnetic transition in iron-rhodium alloys. *Microscience and Microanalysis*, 13:1264 – MSA plugin is available from www.hremresearch.com, 2007.
- [151] C Le Graet. private communication. 2013.

- [152] T. Furuhashi, T. Ogawa, and T. Maki. Atomic structure of interphase boundary of an a precipitate plate in a β Ti[β]Cr alloy. *Philosophical Magazine Letters*, 72(3):175–183, September 1995.
- [153] S Morito, X Huang, T Furuhashi, T Maki, and N Hansen. The morphology and crystallography of lath martensite in alloy steels. *Acta Materialia*, 2006.
- [154] S. Morito, H. Tanaka, R. Konishi, T. Furuhashi, and T. Maki. The morphology and crystallography of lath martensite in Fe-C alloys. *Acta Materialia*, 51(6):1789–1799, April 2003.
- [155] Yugang Sun, Yang Ren, Yuze Liu, Jianguo Wen, John S Okasinski, and Dean J Miller. Ambient-stable tetragonal phase in silver nanostructures. *Nature communications*, 3:971, January 2012.
- [156] Marek Wojnicki, M Luty-Bocho, and Iwona Dobosz. Electro-oxidation of glucose in alkaline media on graphene sheets decorated with gold nanoparticles. *Materials Sciences and ...*, 2013(February):162–169, 2013.
- [157] JH Smith and P Gaunt. The martensitic transformations in gold-manganese alloys near the equiatomic composition. *Acta Metallurgica*, 1961.
- [158] Chun Li and a. Freeman. Giant monolayer magnetization of Fe on MgO: A nearly ideal two-dimensional magnetic system. *Physical Review B*, 43(1):780–787, January 1991.
- [159] Clair C. Calvert, Andy Brown, and Rik Brydson. Determination of the local chemistry of iron in inorganic and organic materials. *Journal of Electron Spectroscopy and Related Phenomena*, 143(2-3):173–187, May 2005.
- [160] D. Ragone. *Thermodynamics of Materials*. Wiley, 1994.

- [161] K.T. Jacob and Debadutta Prusty. Thermodynamic properties of RhO₂. *Journal of Alloys and Compounds*, 507(1):L17–L20, September 2010.
- [162] M. Oxley, M. Varela, T. Pennycook, K. van Benthem, S. Findlay, a. DAlfonso, L. Allen, and S. Pennycook. Interpreting atomic-resolution spectroscopic images. *Physical Review B*, 76(6):064303, August 2007.
- [163] M P Oxley and S J Pennycook. Image simulation for electron energy loss spectroscopy. *Micron (Oxford, England : 1993)*, 39(6):676–84, August 2008.
- [164] E C Cosgriff, M P Oxley, L J Allen, and S J Pennycook. The spatial resolution of imaging using core-loss spectroscopy in the scanning transmission electron microscope. *Ultramicroscopy*, 102(4):317–26, March 2005.
- [165] a B Shah, Q M Ramasse, J G Wen, a Bhattacharya, and J M Zuo. Practical spatial resolution of electron energy loss spectroscopy in aberration corrected scanning transmission electron microscopy. *Micron (Oxford, England : 1993)*, 42(6):539–46, August 2011.
- [166] P. Wang, a. DAlfonso, S. Findlay, L. Allen, and a. Bleloch. Contrast Reversal in Atomic-Resolution Chemical Mapping. *Physical Review Letters*, 101(23):236102, December 2008.
- [167] JO Andersson and Bo Sundman. Thermodynamic properties of the Cr Fe system. *Calphad*, 11(1):83–92, 1987.
- [168] Neumann J. P. Venkatraman, M. The cr-rh (chromium-rhodium) system. *Journal of Phase Equilibria*, 8(2):107–109, 1987.
- [169] Thaddeus B Massalski, Hiroaki Okamoto, PR Subramanian, and Linda Kacprzak. Binary alloy phase diagrams. vol. 2. 1990.

- [170] S Inoue, N Nam, N Phuoc, J Cao, H Yuko, and T Suzuki. Magnetic and magneto-optical properties of FeRh thin films. *Journal of Magnetism and Magnetic Materials*, 320(22):3113–3116, November 2008.
- [171] Y. Ding, D. a. Arena, J. Dvorak, M. Ali, C. J. Kinane, C. H. Marrows, B. J. Hickey, and L. H. Lewis. Bulk and near-surface magnetic properties of FeRh thin films. *Journal of Applied Physics*, 103(7):07B515, 2008.